= SBIR - 02.01-2008
rel date 5/19/92
JAF

THE USE OF VARIATIONAL PRINCIPLES IN IMPROVING COMPUTATIONAL FLUID DYNAMICS METHODOLOGY

Final Report, Contract NAS8-37408

IN-34-CR
207515

P. 159

Prepared for:

National Aeronautics & Space Administration
George C. Marshall Space Flight Center
Marshall Space Flight Center, AL 35812

By

Yen-Sen Chen
Richard C. Farmer
Jon A. Freeman

SECA, Inc.
3311 Bob Wallace Avenue
Suite 203
Huntsville, AL 35805

May, 1990

PROJECT SUMMARY

The objective of this investigation was to produce a CFD model which is computationally efficient, robust and readily adaptable to complex geometries and which accurately describes the physics of a gas mixture reacting with a specified set of chemical kinetic rates. The primary application of this model is expected to be the evaluation of advanced rocket motor designs and the plumes associated with such motors. Analyses of the space shuttle main engine and solid rocket motors flow fields were also made.

The final result of this investigation is an advanced version of the FDNS code which performs all of the steps necessary to predict reacting gaseous propulsive flow fields. Numerous propulsion related problems were analyzed and the results were compared to other analyses or to test data in order to validate this advanced code. The FDNS code provides the methodology required to describe gas flows in advanced propulsion systems sufficient for preliminary design studies.

FORWARD

SECA wishes to acknowledge the technical advice and interest shown by Dr. C. M. Seaford and Mr. J. F. Alison, the NASA/MSFC technical monitors of this study.

TABLE OF CONTENTS

1.0 INTRODUCTION

1.1 Scope of Study

A computational fluid dynamics model was developed to accurately describe the physics of a gas mixture reacting with a specified set of chemical kinetic rates. This model is also computationally efficient, robust and readily adaptable to complex geometries. The primary application of this model is expected to be the evaluation of advanced rocket motor designs and the plumes associated with such motors. Analyses of the space shuttle main engine and solid rocket motors flow fields were also completed. This study did not include multi-phase effects associated with the SRM; although such effects could be added. This investigation provides the methodology required to describe gas flows in advanced propulsion systems sufficient for preliminary design studies.

A secondary objective of this investigation was to provide combustion analysis methodology compatible with sophisticated Navier-Stokes solvers which are in current use but limited to treatment of ideal gas flows. Many multidimensional gas flows have been successfully analyzed. However, only a few of these codes have been used to treat flows with combustion.

A further object of this study was to replace the piecemeal solutions in rocket motor performance analysis and plume analysis programs currently used in the JANNAF standard codes (Refs. 1 and 2) with analyses which are based on a robust Navier-Stokes solver that has been modified to include an efficient kinetics integration routine. The current JANNAF nozzle performance code (Ref. 2) is a composite solution based on an MOC solution with

viscous overlays for treating dissipative terms. For nozzle flows, such methods lead to estimating individual performance losses for the purposes of predicting specific impulse, without attempting to accurately calculate the entire coupled flowfield.

1.2 Summary

The final result of this investigation is an advanced version of the Finite Difference Navier-Stokes (FDNS) code (Ref. 3) which performs all of the steps necessary to predict reacting gaseous propulsive flow fields. The physical phenomena which govern these flows are listed in Table 1. Some of these phenomena may be treated independently with other codes, as indicated in the table. Spray combustion may be treated with KIVA (Ref. 4) and the results of the computation used as input to the FDNS gas code developed in this study. Particulate effects can be predicted with RAMP (Ref. 5) and/or with other codes which are currently under development (Ref. 6), hence these effects were not studied in this investigation. Plume radiation is predicted from flowfield properties which are provided as input to programs like SIRRM (Ref. 7) and ARC (Ref. 8). Since radiation is uncoupled from the flowfield analysis, it was not addressed in this investigation. The FDNS validation test cases completed during this study are also listed in Table 1.

Section 2.0 of this report describes the code development and Section 3.0 presents the validation cases which have been investigated. Table 1 also summarizes the validation cases which were simulated. Section 4.0 addresses the attributes and limitations of the code and indicates the applications for which the code is applicable.

Table 1. CFD Analysis of Rocket Motors and Plumes

FLOW PHENOMENA:

- Spray Analysis - from KIVA

- Multidimensional Compressible Flow[*]

- Inviscid, Laminar & Turbulent Flow[*]

  - Viscosity Options -
    Laminar Viscosity
    Algebraic Eddy Viscosity

  - Wall Boundary Conditions -
    Slip
    No Slip
    Wall Functions

- Steady & Transient Flow[*]

- Subsonic, Transonic & Supersonic Flow[*]

- Chemistry[*]

  - Ideal or Real Gas

  - Equilibrium or Finite Rate

  - Hydrogen or Hydrocarbon Fuel

  - Large Scale Mixing Effects

- Particulate Flows - from RAMP

- Plume Radiation - from SIRRM

VALIDATION CASES INVESTIGATED:

- Laminar, Compressible Supersonic Flat
  Plate Boundary Layer Flow

- SSME Nozzle Sea Level Static Test
  Performance Simulation

- SSME Exhaust Plume Simulation

- Rocket Plume Impingement of Flat Plate

- Base Flow with Clustered Nozzles

- Supersonic Axisymmetric & 3-D Blunt Body
  Flowfield Simulation

- Supersonic 3-D AFE Model Flowfield
  Simulation

[*] Indicates Phenomena Investigated with FDNS
& Validated with Test Cases Shown Above

3

2.0 ROCKET MOTOR VISCOUS/TURBULENT MULTICOMPONENT COMBUSTION FLOWFIELD METHODOLOGY DEVELOPMENT

The original concept of this study was to apply the calculus of variations to compressible fluid flow in order to develop accurate, efficient computational fluid dynamics (CFD) algorithms for production type analyses. The Phase I investigation revealed that the mechanics of a variational solution involved a predictor-corrector calculation in which a time advanced approximation is corrected by requiring that certain constraint equations be satisfied. SECA determined that the time advancement step could most efficiently be accomplished with a rigorous upwind algorithm which evaluated wave propagation along characteristic directions. When this upwind method was implemented, it was found that excellent solutions were obtained without requiring additional correction steps. The balance of the study was therefore devoted to utilizing and validating the upwind, explicit algorithm (GWIND) and to developing an upwind, implicit counterpart designed specifically for steady state problems.

During the initial phase of this Phase II research study other implicit algorithms were encountered that were further along in development and better suited to the accomplishment of the objectives of this effort. The most promising implicit algorithm, the Finite Difference Navier-Stokes (FDNS) solver, was chosen as the baseline methodology for this study. GWIND and FDNS are described in the remainder of this section of the report.

4

2.1 Methodology Developed In Phase I

The ALFA code which was developed by SECA under the Phase I
SBIR contract (Ref. 9) has been split into two codes LWIND and
GWIND applicable to liquid and gas flow problems, respectively.
The GWIND code, which was the original upwind explicit algorithm
considered as the basis for development of an implicit algorithm
in this Phase II SBIR contract, is described in detail in
Appendix A of this final report.

2.2 FDNS Implicit Algorithm Formulation

The FDNS code solves the following form of the conservation
equations, including the Navier-Stokes equations, an energy
equation and two-equation turbulence models, in curvilinear
coordinates:

$$(1/J)(\partial \rho q/\partial t) = \partial[-\rho U_i q + \mu_{eff} G_{ij}(\partial q/\partial \xi_j)]/\partial \xi_i + S_q \qquad (1)$$

where q stands for the dependent variables (i.e. unity, the
velocity vectors, temperature, turbulence quantities, and mass
fractions of chemical species). J, U_i and G_{ij} represent the
Jacobian of the coordinate transformation, transformed
velocities, and diffusion metrics, respectively. They are
written as:

$$J = \partial(\xi, \eta, \zeta)/\partial(x, y, z)$$

$$U_i = (u_j/J)(\partial \xi_i/\partial x_j)$$

$$G_{ij} = (\partial \xi_i/\partial x_k)(\partial \xi_j/\partial x_k)/J$$

μ_{eff} ($= (\mu_l + \mu_t)/\sigma_q$) is the effective viscosity when the turbulent eddy viscosity concept is employed to model turbulent flows. The turbulence eddy viscosity is $\mu_t = \rho C_\mu k^2/\epsilon$, and C_μ and σ_q denote turbulence modeling constants. μ_l is the laminar viscosity. Source terms S_q for the continuity, momentum, energy and species equations are given by:

$$S_q = (1/J) \begin{bmatrix} 0 \\[2ex] -p_x + \nabla[\mu_{eff}(u_j)_x] - (2/3)(\mu_{eff}\nabla u_j)_x \\[2ex] -p_y + \nabla[\mu_{eff}(u_j)_y] - (2/3)(\mu_{eff}\nabla u_j)_y \\[2ex] -p_z + \nabla[\mu_{eff}(u_j)_z] - (2/3)(\mu_{eff}\nabla u_j)_z \\[2ex] Dp/Dt + \Phi + \Sigma J_n C_{pn} \nabla T - \Sigma h_n W_n \\[2ex] \rho(P_r - \epsilon) \\[2ex] \rho(\epsilon/k)(C_1 P_r - C_2 \epsilon + C_3 T^{*C4} P_r^2/\epsilon) \\[2ex] W_n \end{bmatrix}$$

The equation of state for an ideal gas or a real gas is used to close the above system of equations. These equations were solved with the pressure based FDNS solver, which is discussed in detail in Refs. 3 & 10.

A pressure based solution method is employed in FDNS so that a wide range of flow speeds can be analyzed with the same code. Successful results of viscous flow computations using pressure based methods have been reported (Refs. 3, 10, 11). For high

speed flow cases, a hyperbolic pressure correction equation is retained by perturbing the density in the mass conservation equation. This provides a smooth transition from low speed to high speed flow. For time accuracy, a time-centered, time-marching procedure with a multiple pressure corrector algorithm is employed. This method provides numerical efficiency for time-dependent flow problems.

To solve the system of nonlinear coupled partial differential equations, Eq. (2), finite difference approximations are used to establish a system of linearized algebraic equations. A relaxation solution procedure is then employed to couple the equations. First, Eq. (2) is discretized in time with a time-centered (Crank-Nicholson) scheme. That is,

$$(1/J\Delta t)[(\rho q)^{n+1} - (\rho q)^n] = (R_q^{n+1} + R_q^n)/2 \qquad (2)$$

where the superscript n denotes the current time level. If a sub-iteration procedure, designated by a superscript k, within a timestep is applied, the following linearization can be incorporated:

$$(\rho q)^{n+1} = (\rho q)^k + \rho^n \Delta q^k$$

$$R_q^{n+1} = (\partial R_q/\partial q)^k \Delta q^k + R_q^k$$

With the above linearization, the final form of the time-marching scheme can be written as:

$$[(\rho/J\Delta t)^n - (\partial R_q/\partial q)^k] \Delta q^k$$

$$= -(1/J\Delta t)[(\rho q)^k - (\rho q)^n] + (R_q^k + R_q^n)/2$$

The solution at time level n+1 is then updated by:

$$q^{n+1} = q^{k+1} = q^k + \Delta q^k$$

When k = 1 is selected, a non-iterative time-marching scheme is used. As reported in Ref. 3, the non-iterative option with a multi-corrector solution method can provide time accurate solutions for transient flow problems. This multi-corrector procedure is described briefly below.

A simplified momentum equation is combined with the continuity equation to form a pressure correction equation. This pressure correction equation exhibits elliptical behavior for low speed flow and becomes continuously more hyperbolic as flow speed increases. The simplified momentum equation can be written as:

$$\partial \rho u_i / \partial t \approx - \nabla p'$$

or, in discrete form,

$$u'_i \approx - (\Delta t / \rho) \nabla p' \tag{3}$$

where the superscript ' denotes perturbations. The velocity and density fields in the continuity equation are then perturbed to form a correction equation. That is,

$$\nabla (\rho u_i)^{n+1} = \nabla [(\rho^n + \rho') (u^n_i + u'_i)]$$

By neglecting the $\rho' u'_i$ terms, the following equation results.

$$\nabla (u_i \rho') + \nabla (\rho u'_i) = - \nabla (\rho u_i)^n \tag{4}$$

8

Substituting Eq. (3) into Eq. (4) and letting $\rho' = p'/RT$, where R and T represent gas constant and temperature, respectively, the final form of the pressure correction equation is obtained.

$$\nabla[(u_i/RT)p'] - \nabla(\Delta t\, \nabla p') = -\nabla(\rho u_i)^n \qquad (5)$$

Equation (5) has the form of a transport equation with convection and diffusion terms. Upwind treatment can be used to model the left hand side of Eq. (5). A dissipation term is also added to the right hand side of Eq. (5) to provide smooth shock solutions. Using the solution of Eq. (5), the pressure and velocity fields are updated and the density field is then updated by using the equation of state. This corrector procedure is repeated several times (usually 4 times are sufficient) before marching to the next time step. This procedure insures that the mass conservation condition is satisfied for each time step. This represents the multi-corrector solution procedure. This method requires one predictor step and less than four corrector steps to provide numerical efficiency for transient flow computations.

2.2.1 FDNS Finite-Rate/Equilibrium Chemistry Models

a. The PARASOL Finite Rate Chemistry Algorithm for Steady and Unsteady Reacting Flows

The prediction of a non-equilibrium, reacting flowfield is a difficult computational task. In such a flow, the system of chemistry equations is extremely stiff due to the varying time constants of the competing chemical reactions. The stiffness of the chemical system will usually require very small time and/or spatial steps and also cause accuracy and stability problems in

the flow calculations. SECA engineers have developed an efficient finite rate chemistry algorithm (PARASOL) for the description of the highly complicated chemistry systems in reacting flow environments (Ref. 12). The computational analysis is efficient due to a unique treatment of the chemistry source terms. The PARASOL algorithm is available as an option in SECA's state-of-the-art flow analysis code, FDNS.

PARASOL is an implicit, unconditionally stable, accurate, and fast stiff chemistry algorithm. This unique algorithm includes local linearization of the chemical differential equations, and a rational approximation to the matrix exponential of the exact solution to the resulting linear differential equations. Diagonal Pade' approximants are used for the rational approximation and force the satisfaction of the unconditional stability criteria. Calculation of the eigenvalues of the species Jacobians is not required. Unconditional stability means that large integration steps can be taken, and the step size is limited only by the consideration of truncation and round-off errors. No iterative correction nor exponential fit of the solution is needed since this is a one sweep procedure and the matrix exponential of the exact solution is being approximated rationally. The formation of the species Jacobian is automated, and the calculation of the Jacobian pays off in improved stability and computational speed. LINPACK is used to further speed up the matrix evaluation.

The basic governing equations employed to describe the non-equilibrium, chemically reacting flow in generalized three dimensional coordinates are:

$$(1/J)(\partial \rho q/\partial t) = S_q + \Sigma\ (\partial [-\rho Uq + \mu G(\partial q/\partial \xi)]/\partial \xi) \tag{6}$$

where q represents species concentration, velocities, or energy in the governing equations. J is the Jacobian metric, ξ is a generalized curvilinear coordinate, and G is the metric coefficient. In Eq. (6) ρ is density, t is time, and S_q represents the source terms of the governing equations. The summation is over each of the three spatial dimensions.

Consider a general chemical system of n species undergoing m simultaneous elementary reactions:

$$\sum_{i=1}^{n} \nu'_{ik}A_i = \sum_{i=1}^{n} \nu''_{ik}A_i, \qquad k=1,2,\ldots\ldots m \tag{7}$$

where ν'_{ik}, and ν''_{ik} are the stoichiometric coefficients, and A_i is the chemical symbol of the ith species. The source term S_{qi} for volumetric chemical reaction mass production rate of species i is:

$$S_{qi} = \rho\,(d\alpha_i/dt)$$

$$= M_i \sum_{k=1}^{m} (\nu''_{ik}-\nu'_{ik})\,[K_{fk} \prod_{r=1}^{n} (\rho y_r)^{\nu rk} - K_{bk} \prod_{r=1}^{n} (\rho y_r)^{\nu rk}],$$

$$i=1,2,\ldots\ldots n \tag{8}$$

where $y_r = \alpha_r/M_r$, α_r is the mass fraction of species r and M_r is the molecular weight of species r.

The reaction rates are functions of temperature ,T, and are usually expressed in a general Arrhenius form. For example, the forward reaction rate can be expressed as:

$$K_f = CT^s\exp(-E/RT) \tag{9}$$

where C is the Arrhenius constant, s is the temperature dependency coefficient, E is the activation energy and R is the universal gas constant. Eq. (8) is a system of coupled, nonlinear ordinary differential equations. The stiffness of the chemistry system comes from the widely disparate time constants in the nonlinear terms in Eq. (8). Moretti (Ref. 13) showed that stiffness results from drastic changes of local eigenvalues which occur near a flame front.

Two general approaches can be used to solve the above reacting flow system: the full solution approach or the chemistry split/ chemistry factorization approach. The full solution approach advances the flow time step and the chemistry time step with the same step size. However, this procedure is not efficient since the stiff chemistry time step is always smaller than the flow step. The whole calculation would then be forced to advance with the smallest chemistry time step. The chemistry splitting simply means several chemistry steps are allowed within one flow step. A recent study of hydrogen/air reacting flow used a preconditioning matrix for advancing the calculation in larger time steps. The computational time steps, however, were still limited to the small chemistry time steps. It has been shown that the computational speed of the chemistry split approach using a stiff chemistry solver is always faster than that of the full solution, and the final solutions of each are very similar. An obvious computational strategy for reacting flow is to use the chemistry split approach and to develop an efficient finite rate chemistry algorithm for the integration of Eq. (6). Notice that in the chemistry split approach, the chemistry source terms are coupled with all the gas dynamic flow equations.

In theory, many standard explicit and implicit numerical methods can be used to integrate the chemistry system of Eq. (8). However, explicit methods generally require smaller time steps; whereas, implicit methods are generally more stable and allow larger integration steps to be taken within the limitation imposed by truncation and round-off errors. Unfortunately, the merits of the implicit method are dependent upon the form of the differential equations and the amplification factor; the method is not always convergent for stiff chemistry equations.

PARASOL is an unconditionally stable implicit scheme and is most suitable for integrating the finite rate chemistry equations. It is based on the formation of Pade' approximants to accelerate the convergence of a power series. This technique has been used extensively in physics and chemistry. However, its application in engineering has been limited, particularly in the finite rate chemistry field. Although an early study successfully applied the technique to combusting flow problems (Ref. 14), the method has largely been lost in the multitude of other published finite rate chemistry methods. The basic development of the PARASOL algorithm in solving the finite rate chemistry problems is presented below, starting with Eq. (6) cast in a general form.

$$dy/dt = f(y, T, \rho) \tag{10}$$

Nonlinear instability will occur if Eq. (10) were to be solved directly with even modest time steps. Expanding Eq. (10) through the first order terms, the linearized equation becomes:

13

$$dy/dt = f(y_o, T_o, \rho_o) + (\partial f/\partial y)_o \Delta y + (\partial f/\partial T)_o \Delta T + (\partial f/\partial \rho)_o \Delta \rho$$
$$+ O(\Delta y^2, \Delta T^2, \Delta \rho^2) \qquad (11)$$

where y, f, $\partial f/\partial T$ and $\partial f/\partial \rho$ are column vectors, $\partial f/\partial y$ is a species Jacobian matrix, and the subscript o stands for the initial value. Notice the neglected higher derivative terms involve Δy^2, ΔT^2 and $\Delta \rho^2$. The density term can be eliminated through the use of the equation of state. If the temperature term is eliminated by assuming that the temperature change is small within an integration step, Eq. (11) can be simplified as:

$$dy/dt = f(y_o, T_o, \rho_o) + (\partial f/\partial y)_o \Delta y + O(\Delta y^2) \qquad (12)$$

Conceptionally, the ΔT term could be retained in the following development, but this has been found to be unnecessary. Equation (12) is a system of n linear ordinary differential equations with constant coefficients and can be regrouped as:

$$dy/dt = A \, y(t) + B \qquad (13)$$

where A is a n x n species Jacobian matrix and B is a n element column vector. The formal solution of Eq. (13) at t=h is

$$y(h) = \exp(hA)(y_o + A^{-1}B) - A^{-1}B \qquad (14)$$

In Eq. (14), the matrix exponential term can not be evaluated directly but may be approximated with polynomials, and the form of the approximation will determine whether it is accurate, efficient and stable. For a family of unconditionally stable schemes, the Pade' approximants are found to be more efficient than the Hermitian approximants. The Pade' approximation of the matrix exponential of Eq. (14) can be expressed as:

$$\exp(hA) = Q^{-1}P + O(hA)^{p+q+1} \tag{15}$$

where:

$$P = \sum_{k=0}^{p} \frac{(p + q - k)!p!}{(p + q)!k!(q - k)!} (hA)^{k} \tag{16}$$

and

$$Q = \sum_{k=0}^{q} \frac{(p + q - k)!q!}{(p + q)!k!(q - k)!} (-hA)^{k} \tag{17}$$

and P and Q are Pade' approximants in their pth and qth order, respectively. The truncation error means that these formula must agree with the exponential power series for at least $p + q + 1$ terms. Substituting the approximants into Eq. (14), the integration formula becomes:

$$y(h) = Q^{-1}[Py_o + (P - Q)A^{-1}B] \tag{18}$$

Eq. (18) includes many types of single step integration methods and not all of them are stable. The Euler explicit method, which has been shown to be partially stable, is a special case of Eq. (18) with $P = I + hA$ and $Q = I$ ($p = 1$ and $q = 0$). While $P = I$ and $Q = I - hA$ ($p = 0$ and $q = 1$) is the stable Euler implicit formula. Diagonal Pade' approximants ($q = p$) have the smallest truncation error of those Pade' approximants and are A-stable. The approximation of the matrix exponential by diagonal Pade' approximants is called Pade' Rational approximation. The algorithm of applying Pade' Rational approximation to the formal solution of a system of finite rate chemistry equations has been named Pade' Rational Solution (PARASOL) by SECA.

The integration formula can be derived for any order of

15

truncation. For the cases of $p = q = 1$, the following solution is obtained for Eq. (13):

$$y(h) = (I - 0.5\ hA)^{-1}[(I + 0.5\ hA)y_o + hB] \tag{19}$$

The truncation error is $O(h^3)$ for Eq. (14), and is $O(h^5)$ for $p = q = 2$.

Mathematically, a network of equations is stable if the eigenvalues of the coefficient matrix of its locally linear representation have negative real parts. Unconditional stability means the numerical algorithm is stable for any step size with the restriction that errors introduced by truncation and roundoff may accumulate but not grow in an unbounded manner. To analyze the stability criteria of PARASOL, Eq. (18) can be written in a simpler form after the method is applied to its n+1 th step:

$$\underline{y}^{n+1} = Q^{-1}P\underline{y}^n + C \tag{20}$$

where $\underline{y} = y(nh)$. The true solution may be expressed as:

$$y^{n+1} = Q^{-1}Py^n + C + \tau^{n+1} \tag{21}$$

where τ^{n+1} is the truncation error. The error at each step will be the difference between the true solution and the integrated solution:

$$e^n = y^n - \underline{y}^n \tag{22}$$

Subtracting Eq. (20) from Eq. (21), we obtain

$$e^{n+1} = (Q^{-1}P)e^n + \tau^{n+1} \tag{23}$$

The truncation error can be ignored and the propagation of the error from the source term at the first step, e_o, to the error at the nth step can be represented as:

$$e^n = (Q^{-1}P)^n e_o \tag{24}$$

The error will grow or decay according to the amplification matrix $(Q^{-1}P)$. From the definition of stability, when the eigenvalues of the matrix A have negative real parts, the error must decrease as the number of integration steps increase. The error can only decrease if the absolute eigenvalue of the amplification matrix is less than one. For every eigenvalue of the matrix A, there is a corresponding eigenvalue for the amplification matrix. The stability criteria then requires:

$$|P(\underline{\lambda})| < |Q(\underline{\lambda})| \tag{25}$$

For the complex eigenvalue $\underline{\lambda} = h\lambda = -\alpha + \beta i$ ($\alpha > 0$), the complex eigenvalues for P and Q of Eq. (19) are

$$P(\underline{\lambda}) = (1 - 0.5 \alpha) + 0.5 \beta i \tag{26}$$

and

$$Q(\underline{\lambda}) = (1 + 0.5 \alpha) - 0.5 \beta i \tag{27}$$

Equation (26) and Eq. (27) satisfy the stability criteria. Since the stepsize h does not explicitly enter into the analysis, PARASOL is unconditionally stable for all step sizes. The above stability criteria can be easily applied to higher order diagonal Pade' approximants.

PARASOL in its current status, has been successfully applied to a number of chemistry systems such as: a transient combustor simulation (Ref. 15), the interaction with a stochastic reactor (Ref. 16), and a hydrogen/air reactive dump combustor using the FDNS code (Ref. 12). While comparing to TRW's predictor-corrector equation based on the same number of matrix operations, PARASOL's truncation error is $O(h^5)$ versus $O(h^3)$ for TRW's algorithm.

One of the more popular algorithms for solving stiff systems of ordinary differential equations is that developed by Gear, which was later adapted specifically for finite rate chemistry in the code GCKP. These schemes employ Adams' explicit method of variable order to solve nonstiff equations and implicit formulas to solve the stiff equations. GCKP84 is a revised version of GCKP that used an implicit predictor-corrector procedure for systems of stiff differential equations. Hindmarsh generalized the GEAR algorithms and developed a series of stiff ODE solvers like EPISODE and LSODE. CREK1D used a two part predictor-corrector and an exponentially fitted trapezoidal scheme. CHEMEQ also applied predictor-corrector methods to normal ODE's, but used an asymptotic integration method for the equations which are determined to be stiff. It is noted that separating the system of equations into nonstiff and stiff parts and treating them differently resulted in a mass conservation problem. A recent study has compared the performance of the above finite rate packages on a twelve step, H_2-O_2-CO-N_2 reaction system. Performance was measured by CPU computation times required for a range of error tolerance values. The error tolerance is the maximum allowable change of specified dependent variables in an integration step while still maintaining the system stability and accuracy. The error tolerance can be related to species

concentrations, temperature, or density. <u>A better finite rate
chemistry algorithm will have shorter CPU times at higher error
tolerance values</u>. Figure 1 shows a comparison of the performance
of several algorithms reported in that study, and the performance
obtained by SECA using PARASOL on the same test case. Notice all
the codes tested were designed for stiff chemistry systems. It
can be seen that CHEMEQ is the slowest scheme tested, although
CHEMEQ is probably much faster than a classical second order
predictor-corrector scheme. GCKP84 and EPISODE do not run for
error tolerance greater than 1.0E-6. This makes them highly
inefficient when used with gas dynamic equations since small
chemistry steps must be taken. LSODE and CREK1D are the faster
ones; CREK1D has a slight advantage over the LSODE near the
higher error tolerance. CREK1D is faster than LSODE because it
uses old Jacobians and a filter mechanism. PARASOL has two
curves plotted in Fig. 1, the upper one is the regular PARASOL
while the lower one is a diagonalized version used during
numerical experimentation. Both PARASOL curves show longer CPU
time at lower tolerance values and shorter CPU time at higher
tolerance values than those of CREK1D and LSODE. It should be
pointed out that the regular PARASOL curve is consistently lower
than that of CREK1D for tolerance greater than 4.0E-4. The CPU
time required for regular PARASOL at 0.01 tolerance is half of
that required by CREK1D. SECA has collected <u>all</u> of the codes
used in the comparisons shown in Fig. 1 for use in future
kinetics studies.

Two points need to be made in regard to the merits of
PARASOL. Firstly, the PARASOL can be further improved, e.g., by
using filter schemes. Secondly, the computational strategy for
reacting flow calculations is to set the tolerance level as high
as possible, since fewer chemistry steps must be taken within one
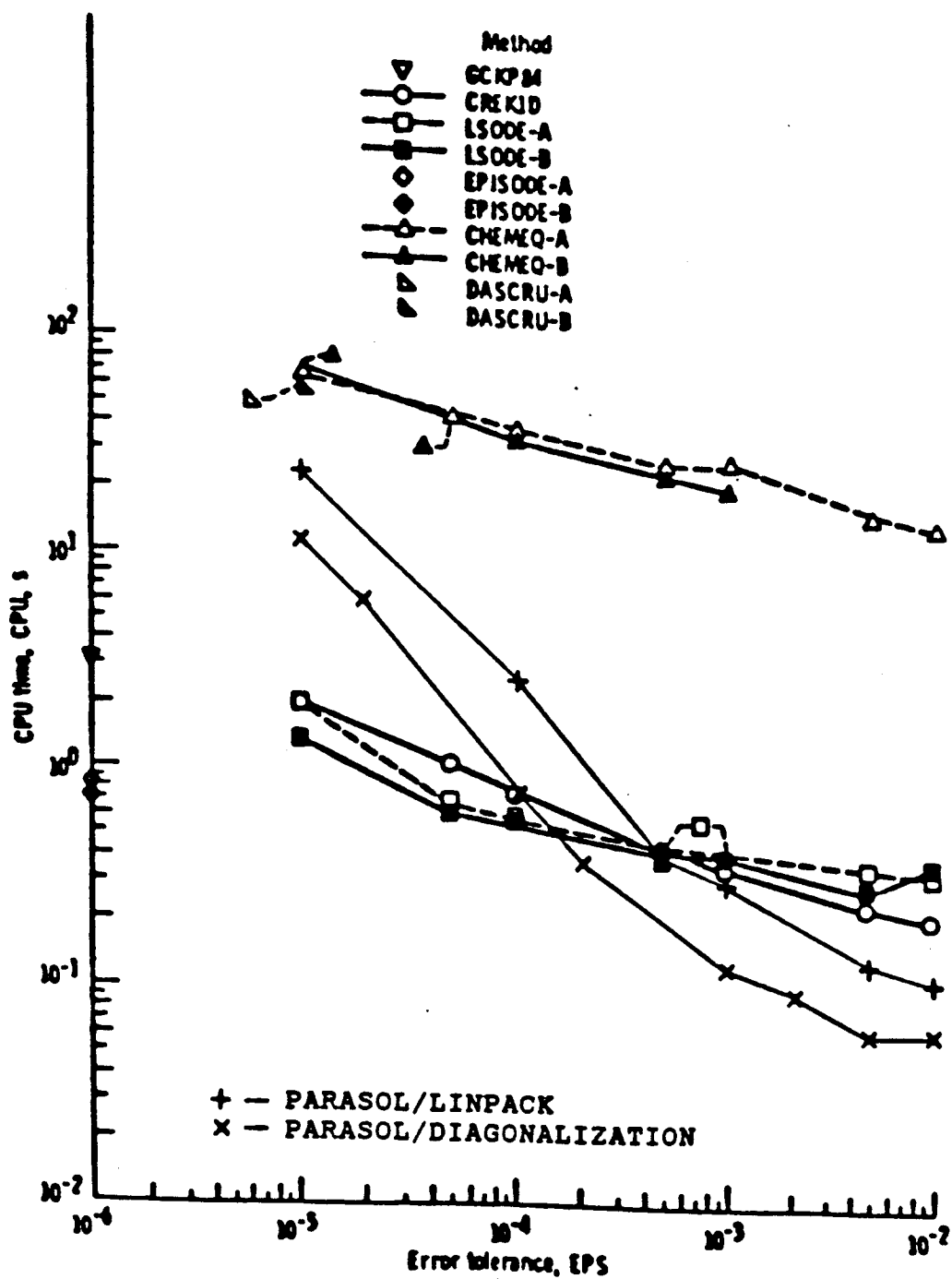flow step; hence, the advantage of PARASOL is evident.

Fig. 1. Comparison of the CPU Time Against Error Tolerance for
a H_2-O_2-CO-N_2 Chemistry System

b.   Special Chemistry Models for Steady State Reacting Flows

An efficient equilibrium chemistry procedure based on the method of equilibrium constants and an accelerated finite rate chemistry solver have been developed and added as options to the FDNS code. The equilibrium species concentrations were calculated with the equilibrium constant method. A four-reaction mechanism plus two element balance equations were used for the H_2-O_2 system (i.e. six equations for six species).   For the finite rate chemistry procedure, the species concentrations were solved by a set of species continuity equations with source terms calculated based on the forward and backward reaction rate constants of an elementary reaction set. The forward reaction rate constants in Arrhenius form were obtained from known data. Equilibrium constants calculated by using Gibbs free energy were used to evaluate the backward rate constants.

In order to further reduce the stiffness problem in solving the finite-rate species equations with very strong source terms, two methods were used to accelerate the FDNS relaxation solution procedures. In the first approach, the source terms of species equations were split into an implicit and an explicit part associated with sink and source terms, respectively. This provides about the same magnitude for the left and the right hand sides of the transport equations. The second method utilized a different time step size for the species equations to reduce the extent of the chemical reaction within a time step. Both methods were found to be very efficient in obtaining steady state solutions. The procedures described above for the equilibrium and finite rate chemistry steady state flow solver are summarized below. The H_2-O_2 system is discussed as an example.

c. Equilibrium Chemistry Model

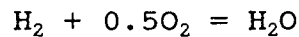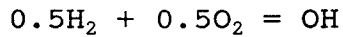For H_2-O_2 chemical system, the global reaction with six species are written as:
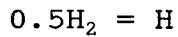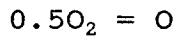
$$AH_2 + BO_2 = n_1H_2O + n_2O_2 + n_3H_2 + n_4O + n_5H + n_6OH$$
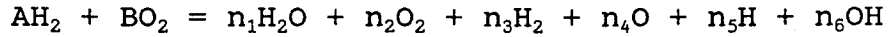
The following element balance relations hold:

$$H: \quad 2A = 2n_1 + 2n_3 + n_5 + n_6 \tag{28}$$

$$O: \quad 2B = n_1 + 2n_2 + n_4 + n_6 \tag{29}$$

The following elementary reactions to provide the additional four equations for solutions of the six-species system.

$$0.5O_2 = O$$
$$0.5H_2 = H$$
$$0.5H_2 + 0.5O_2 = OH$$
$$H_2 + 0.5O_2 = H_2O$$

Using the equilibrium constants, the following algebraic equations can be obtained.

$$n_1 = (n/p)^{-0.5}n_3n_2^{0.5}K_4 \tag{30}$$
$$n_4 = (n/p)^{0.5}n_2^{0.5}K_1 \tag{31}$$
$$n_5 = (n/p)^{0.5}n_3^{0.5}K_2 \tag{32}$$
$$n_6 = n_2^{0.5}n_3^{0.5}K_3 \tag{33}$$

where $n = \Sigma\, n_i$ is the molar density and p is the local pressure. K_1, K_2, K_3, and K_4 are equilibrium constants which are calculated

with the Gibbs free energy, f.

$$K_1 = \exp\{-(0.5f_{O2} - f_O)\}$$
$$K_2 = \exp\{-(0.5f_{H2} - f_H)\}$$
$$K_3 = \exp\{-(0.5f_{H2} + 0.5f_{O2} - f_{OH})\}$$
$$K_4 = \exp\{-(f_{H2} + 0.5f_{O2} - f_{H2O})\}$$

Equations (28) through (33) can be solved for every grid point by using Newton's iteration procedure.

d. Accelerated Finite Rate Chemistry Model

At best, finite-rate combustion calculations require much computation time. The PARASOL algorithm was used previously for analyzing the transient operation of the fuel preburner in the SSME (Ref. 15). However, when either extremely high pressures or temperatures cause the reaction rates to be very fast, finite-rate calculations can require very small time steps. For steady-state, finite-rate CFD calculations can be accelerated by the following method. This method was developed under contract NAS8-38454 (Ref. 16) by SECA.

A general system of chemical reactions can be written as in Eq. (7), and the net rate of change in the molar concentration of species i due to reactions j (X_{ij}) can be written as in Eq. (8). The forward and backward reaction rates are related by:

$$K_{ej} = K_{fj}/K_{bj}$$

23

where:

K_{ej} = equilibrium constant

$= (1/RT)^{\Sigma(\nu_{ij}' - \nu_{ij})} \exp\{\Sigma(f_i'\nu_{ij}' - f_i\nu_{ij})\}$

f_i = Gibbs free energy of species i

and the species production rate, ω_i, (in terms of mass fraction) is calculated by summing over all reactions.

$$\omega_i = M_{Wi} \sum_j X_{ij}$$

The i-th species continuity equation can be written:

$$\rho\ D_t\alpha_i - \nabla[(\mu_{eff}/\sigma_\alpha)\nabla\alpha_i] = \omega_i$$

where μ_{eff} = effective turbulent eddy viscosity

σ_α = Schmidt number for turbulent diffusion

As mentioned previously, this set of species continuity equations can be solved by: (1) splitting ω_i into two terms, that is

$$\omega_i = (\omega_i)_{explicit} - (\omega_i)_{implicit}$$

where $(\omega_i)_{implicit} = (\partial\omega_i/\partial\alpha_i)\Delta\alpha_i$

with the implicit part moved over to the left hand side of the equations; or (2) employing a small time step size based on the assigned tolerance for species correction within a time step, that is

$$(\Delta t)_{chemistry} = \rho(\Delta\alpha_i)_{assigned}/\omega_i$$

The second method was selected for the test cases given in this report. This is due to the basic feature of this method that all species at a given point in space evolve consistently according to rates computed explicitly. The only disadvantage of this method is that the time step size is non-uniform in space which limits its applicability to steady-state flow problems only.

After the chemistry source terms are evaluated for known flow conditions and species concentrations given by the previous time level, the system of species continuity equations are solved using the source-term-limited time step size for each grid point. A Euler implicit time marching scheme is employed with implicit convection and diffusion terms. This method is unconditionally stable and is suitable for steady-state solutions. The species continuity equations are solved one by one using a modified Stone's strongly implicit matrix solver.

In summary, efficient procedures for solving equilibrium and finite-rate chemistry systems have been incorporated into the FDNS code. Applications of these methods to SSME nozzle steady state flow test cases which are described in Section 3.0 of this report have shown good accuracy compared with measured data. Only 30 to 50 percent more CPU time than non-reacting cases is required in the present investigations.

2.2.2 FDNS Turbulence Models

The two-equation k-ϵ turbulence modeling approach is employed in FDNS. The general form of two-equation k-ϵ turbulence models including model constants and damping functions from several models are shown in Table 2. It has been shown that

Table 2. Two Equation k-ε Turbulence Models

The general form of two-equation k-ε turbulence models can be written as:

$$\rho D_t k = \nabla[(\mu+\mu_t/\sigma_k)\nabla k] + \rho(P_r-\epsilon+D)$$

$$\rho D_t \epsilon = \nabla[(\mu+\mu_t/\sigma_\epsilon)\nabla \epsilon] + \rho[(\epsilon/k)(C_1 f_1 P_r - C_2 f_2 \epsilon)+E)]$$

where the turbulent viscosity and kinetic energy production rate are given by:

$$\mu_t = \rho C_\mu f_\mu k^2/\epsilon$$

$$P_r = (\mu_t/\rho)[2(u_x^2+v_y^2+w_z^2)+(v_x+u_y)^2+(w_y+v_z)^2+(u_z+w_x)^2 - (2/3)(u_x+v_y+w_z)^2]$$

D and E are defined by the following parameters:

R_T = turbulent Reynolds number = $\rho k^2/\mu\epsilon$

R_y = dimensionless distance from the wall = $\rho y\sqrt{(k)}/\mu$

y^+ = another dimensionless distance from the wall

$$= \rho y\sqrt{(\tau w/\rho)}/\mu$$

Also note: $\lambda \approx \sqrt{(10\nu k/\epsilon)}$

$$p^+ = (\mu/\rho^2 u_\tau^3)(\partial_s p)_w$$

$$u_\tau = \sqrt{(\tau_w/\rho)}$$

The turbulence model constants, C_μ, C_1 and C_2, are tuned against basic turbulent flows (e.g. homogeneous turbulence, wall equilibrium conditions, planar and circular jets, etc.). The turbulence Schmidt numbers, σ_k and σ_ϵ, are determined based on the spreading rate of k and ε which satisfy the consistency condition.

The model constants and damping functions used in several k-ε models are summarized in subsequent pages of this table.

Table 2. Turbulence Models, cont. p.1

Model	standard	extended Chen-Kim	Launder-Sharma
k_w, ϵ_w B.C.	wall functions	wall functions	$k_w = \epsilon_w = 0$
C_μ	0.09	0.09	0.09
C_1	1.44	$1.15+0.25\mathrm{Min}\{3,P_r/\epsilon\}$	1.44
C_2	1.92	1.90	1.92
σ_k	1.0	0.8927	1.0
σ_ϵ	1.3	1.15	1.3
f_μ	1.0	1.0	$\exp\{-3.4(1+R_T/50)^{-2}\}$
f_1	1.0	1.0	1.0
f_2	1.0	1.0	$1-0.3\exp\{-R_T^2\}$
D	0.0	0.0	$-2\nu(\partial_y\sqrt{k})^2$
E	0.0	0.0	$2\nu\nu_t(\partial_{yy}U)^2$

Model	Hassid-Poreh	Hoffman	Dutoya-Michard
k_w, ϵ_w B.C.	$k_w = \epsilon_w = 0$	$k_w = \epsilon_w = 0$	$k_w = \epsilon_w = 0$
C_μ	0.09	0.09	0.09
C_1	1.45	1.81	1.35
C_2	2.0	2.0	2.0
σ_k	1.0	2.0	0.9
σ_ϵ	1.3	3.0	0.95
f_μ	$1-\exp\{-0.0015R_T\}$	$\exp\{-1.75/(1+R_T/50)\}$	$1-0.86\exp\{-(R_T/600)^2\}$
f_1	1.0	1.0	$1-0.04\exp\{-(R_T/50)^2\}+(\lambda/2y)^2$
f_2	$1-0.3\exp\{-R_T^2\}$	$1-0.3\exp\{-R_T^2\}$	$1-0.3\exp\{-(R_T/50)^2\}-0.08(\lambda/y)^2$
D	$-2\nu k/y^2$	$-(\nu/y)\partial_y k$	$-2\nu(\partial_y\sqrt{k})^2$
E	$-2\nu(\partial_y\sqrt{\epsilon})^2$	0.0	$-C_2 f_2(\epsilon D/k)^2$

Table 2.   Turbulence Models, cont. p.2

Model: Reynolds		Chien	Lam-Bremhorst
k_w, ϵ_w B.C.	$k_w=0, \ \epsilon_w=\nu\partial_{yy}k$	$k_w = \epsilon_w = 0$	$k_w=0, \ \epsilon_w=\nu\partial_{yy}k$
C_μ	0.084	0.09	0.09
C_1	1.0	1.35	1.44
C_2	1.83	1.80	1.92
σ_k	1.69	1.0	1.0
σ_ϵ	1.3	1.3	1.3
f_μ	$1-\exp\{-0.0198R_y\}$	$1-\exp\{-0.0115y^+\}$	$[1-\exp\{-0.0165R_y\}]^2(1+20.5/R_T)$
f_1	1.0	1.0	$1+(0.05/f_\mu)^3$
f_2	$f_\mu[1-0.3\exp\{-R_T^2/9\}]$	$1-0.22\exp\{-R_T^2/36\}$	$1-\exp\{-R_T^2\}$
D	0.0	$-2\nu k/y^2$	0.0
E	0.0	$-2\nu(\epsilon/y^2)\exp\{-0.5y^+\}$	0.0

Model	Nagano-Hishida	Lai-So-Hwang
k_w, ϵ_w B.C.	$k_w = \epsilon_w = 0$	$k_w = \epsilon_w = 0$
C_μ	0.09	0.09
C_1	1.45	1.35
C_2	1.90	1.80
σ_k	1.0	1.0
σ_ϵ	1.3	1.3
f_μ	$[1-\exp\{-y^+/26.5\}]^2$	$1-\exp\{-0.0113y^+(1-4.372p^+)\}$
f_1	1.0	1.0
f_2	$1-0.3\exp\{-R_T^2\}$	$1-(2/9)\exp\{-R_T^2/36\}$
D	$-2\nu(\partial_y\sqrt{k})^2$	$-2\nu k/y^2$
E	$\nu\nu_t(1-f_\mu)(\partial_{yy}U)^2$	$-2\nu(\epsilon/y^2)\exp\{-0.5y^+\}$

in the extended k-ϵ model (Ref. 18), two time scales (the production rate time scale, k/P_r, and the dissipation rate time scale, k/ϵ) can be included in the dissipation rate equation to cause the dissipation rate to respond more effectively to the mean strain than it does in the standard k-ϵ model. The net effect of the energy transfer function is to enhance the development of ϵ when the mean strain is strong or the production rate is large, and the generation of ϵ is suppressed if the converse is true. The source term for the dissipation rate equation is:

$$S_\epsilon = \rho (C_1 P_r \epsilon / k - C_2 \epsilon^2 / k + C_3 P_r^2 / k) \qquad (34)$$

The last term represents the energy transfer from large scale turbulence to small scale turbulence and is controlled by the production rate and the dissipation rate time scales. This formulation enables the dissipation rate to respond to the mean flow field more rapidly so as to control the development of the turbulent kinetic energy more effectively. It has proved to be effective for isothermal flows such as boundary layers and general elliptic type flows. For non-isothermal flows such as a chemically reacting flow in a ramjet dump combustor configuration, the isothermal standard k-ϵ and extended k-ϵ models predict too rapid a decay of the centerline kinetic energy profile. The extended k-ϵ model predicts a slower centerline velocity decay than the standard k-ϵ model. It was therefore postulated that a temperature dependent term could be added to the last term of Eq. (34) for non-isothermal flows, without changing the modeling constants already determined for the isothermal turbulent flows. The value of the temperature dependency term is unity for isothermal flows and does not effect the turbulent flowfield. The rationale behind this new

29

turbulence model [k-ϵ{T}] is that the temperature rise in the reacting flow causes an increase in the dissipation rate, and the net effect is a reduced effective viscosity. The final expression for the dissipation rate equation source term is:

$$S_\epsilon = \rho(C_1 P_r \epsilon / k - C_2 \epsilon^2 / k + C_3 (T^*)^{C_4} P_r^2 / k) \tag{35}$$

The final values of these model constants for the k-ϵ{T} turbulence model are: $C_1 = 1.15$, $C_2 = 1.9$, $C_3 = 0.25$ and $C_4 = 0.6$.

Large scale turbulence effects can be introduced into the species continuity equations with probability distribution functions (PDF) to simulate unmixedness effects, as described in Ref. 16, if the need arises.

2.2.3 FDNS Grid Options

Computational grids for FDNS may be generated by an external grid generator such as the GWIND grid module. GRID is an algebraic grid generator capable of creating 2-D, axisymmetric and 3-D grids over complex fluid flow regions. The module uses a library of edge and surface shape functions which may be bilinearly or trilinearly blended to obtain a body fitted coordinate system.

The shape functions currently in the module include; straight edges, a set of fixed points, circular arcs, elliptical arcs, parabolic arcs, and helical arcs. Surface shapes available are flat plates, cylindrical surfaces, cones, spheres, biconics and edges of revolution.

Each edge of the region may consist of more than one shape and each surface may consist of segments of different shapes. In addition, intermediate edges may be imposed on any of the surfaces to facilitate modeling complex features or the geometry.

Other helpful features of the module are the capability to employ uneven nodal distributions via a quadratic stretching function and the capability to divide a complex geometry into separate, distinct regions to be mated in the pre-processor module.

An example of a 3-D grid for FDNS produced by the GWIND GRID module is shown in Section 3.4.3 of this report in Fig. 57. Grids for FDNS may also be provided by other interactive grid generators, such as GENIE.

2.2.4 FDNS Boundary Condition Options

Various types of boundary conditions can be incorporated in the FDNS code by simply changing the input data for boundary control parameters. These boundary types are: supersonic inlet, subsonic inlet, outlet boundary, symmetry boundary, free surface boundary, cyclic boundary, and solid wall boundary. For supersonic inlet boundaries, all flow conditions are fixed unless transient inlet boundary conditions are required. For subsonic internal flow inlet boundaries, v- & w-velocities and pressure wave characteristics are extrapolated upstream. At subsonic external in-flow boundary, only the v- & w-velocity components are extrapolated. Along the outlet boundary, all variables are extrapolated unless a fixed pressure subsonic exit boundary condition is specified. For symmetry planes, zero gradient boundary conditions are applied for all scalars and vectors

parallel to the symmetry planes. Along free boundaries, a zero gradient condition is applied to all variables. For cyclic boundary conditions, the FDNS solver employs overlapping cyclic boundaries. This method is also used for multi-zone arrangements. For the solid wall boundaries, a non-slip boundary condition is applied for the momentum equations and the pressure field is assumed to have a zero gradient normal to the walls. Either isothermal or adiabatic wall boundary conditions can be used for the energy equation. In the case of turbulent flow computations, the conventional wall function approach is employed.

2.2.5 FDNS Graphics Output Options

Output from FDNS flowfield solutions can be displayed graphically in the form of X vs. Y or contour plots. Plotting software is machine dependent. The plotted output from FDNS which is presented in Section 3 of this report was generated on either the NASA/MSFC IBM 3084 front end to the CRAY X-MP4 or the VAX 11/785 computers. That is, the external plot programs that are currently used to plot FDNS results use PLOT 10 software and are operational on the IBM 3084 and VAX 11/785 computers.

3.0 FDNS CODE VALIDATION

A variety of gaseous flows were studied to establish the validity of the FDNS code. Heat transfer effects, multiple speed regimes, and the chemistry models were studied to test FDNS for a wide range of applications. The results of the specific cases investigated will be presented and discussed in this section.

3.1 Laminar Compressible Boundary Layer Flow

3.1.1 Heat Transfer Characteristics

Wall heat transfer characteristics are presented in this section prior to the description of the boundary layer validation test cases. For simple flows (e.g. flat plate boundary layer flows), similarity solutions can be used for data comparisons. For instance, the Reynolds analogy factor, S, for perfect gas with constant property is given in Ref. 19 as:

$$S = C_f/(2C_h) = P_r^{2/3} = 0.8033, \quad \text{for flat-plate boundary}$$
$$\text{layers with freestream Mach}$$
$$\text{number M.}$$

where:

C_f = skin friction coefficient

$C_h = q_w/(0.2 \; r \; Q_{ref} \; M^2)$

P_r = Prandtl number = 0.72

q_w = heat flux at wall

$Q_{ref} = C_p$(freestream density * velocity)(wall temp.)

r = temperature recovery factor = $P_r^{0.5}$

With Sutherland's viscosity law, it has been shown in Ref. 20 that S and r decrease with increasing freestream Mach number.

This temperature dependent viscosity effect is not considered in the following flat-plate boundary layer heat transfer analyses.

For blunt body heat transfer problems, however, a temperature-viscosity function for air at low pressure and low temperature is employed based on Sutherland's formula. That is,

$$\text{Viscosity} = 0.312986 \, (\text{Viscosity})_{ref} \, T^{1.5}/(T + 198)$$

with a reference temperature of 95.89°R. The local fluid temperature is represented by T. This formula is suitable for the wind tunnel operating conditions reported in Refs. 21 – 23. The measured pressure and heat transfer data in these references are the basis of comparisons for the blunt body test cases presented in Section 3.4 of this report. One useful correlation developed by Fay and Riddell (Ref. 19) for blunt body stagnation point heat transfer at supersonic speed is also used for data verification. This correlation is given as:

$$q_w = C \, P_r^{-0.6}(\rho \, \mu \, K)_e^{0.5}[(\rho\mu)_w/(\rho\mu)_e]^{0.1}(H_e - H_w)$$

where the subscript e stands for the conditions behind the shock.

C = 0.763, for a sphere.
C = 0.57, for a cylinder.
K = 1.14 U_o/D, for cylinder or sphere at freestream Mach number greater than 4.

Based on this correlation, the stagnation point Stanton number can be written as:

$$St = q_w/[(\rho U)_o(H_t - H_w)]$$

34

$$St \approx C\ P_r^{-0.6}[(1.14/Re)(\rho\mu)_e/(\rho\mu)_o]^{0.5}[(\rho\mu)_w/(\rho\mu)_e]^{0.1}\ (H_e-H_w)/(H_t-H_w)$$

3.1.2 Laminar, Compressible Boundary Layer Flow FDNS Validation Test Cases

These 2-D planar test cases consider an ideal gas, and the laminar, compressible boundary layer developed along a flat plate. The free stream Mach numbers considered are 4, 6, 8 and 10, the flow Reynolds number is 6.2E+5 per meter and the wall temperature is assumed to be isothermal at free stream temperature. The Prandtl number is assumed to be 0.72. The computational domain has a size of 1.0 x 0.02 with the inflow boundary layer thickness of 0.001. A grid size of 61 x 21, with more grid points clustered near the wall boundary, is used for this case. The Mach 4.0 boundary layer axial velocity and temperature profiles predicted by FDNS at the downstream boundary are compared in Fig. 2 with similarity solutions given by Hantzsche and Wendt in Ref. 20 which used a Prandtl number 0.7. Figure 2 shows good agreement between the FNDS results and the cited similarity profiles. The discrepancy in the boundary layer thickness may be caused by different upstream flow conditions used in the FDNS calculation. The increased calculated temperature level outside of the boundary layer $(Y/X_{ref}>0.011)$ is due to a compression wave developed at the inflow boundary, which reduces the freestream Mach number to 3.96. Table 3 summarizes the Reynolds analogy factor comparisons for the four boundary layer test cases. It is clear that the FDNS predictions are in good agreement with the Reynolds analogy factor analytical value of 0.8033.

(a) ## U-VELOCITIES
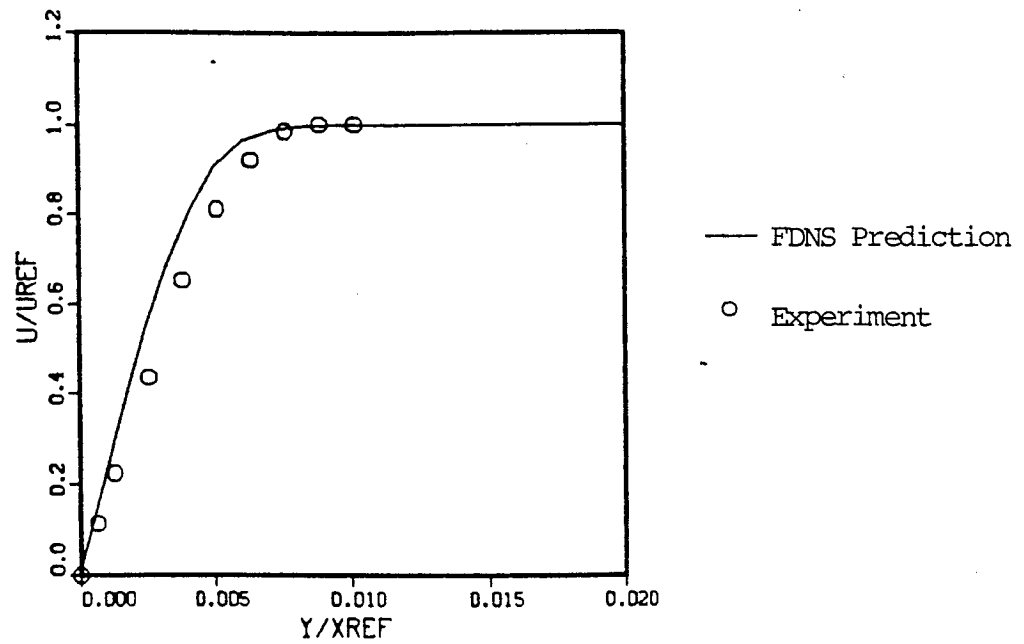
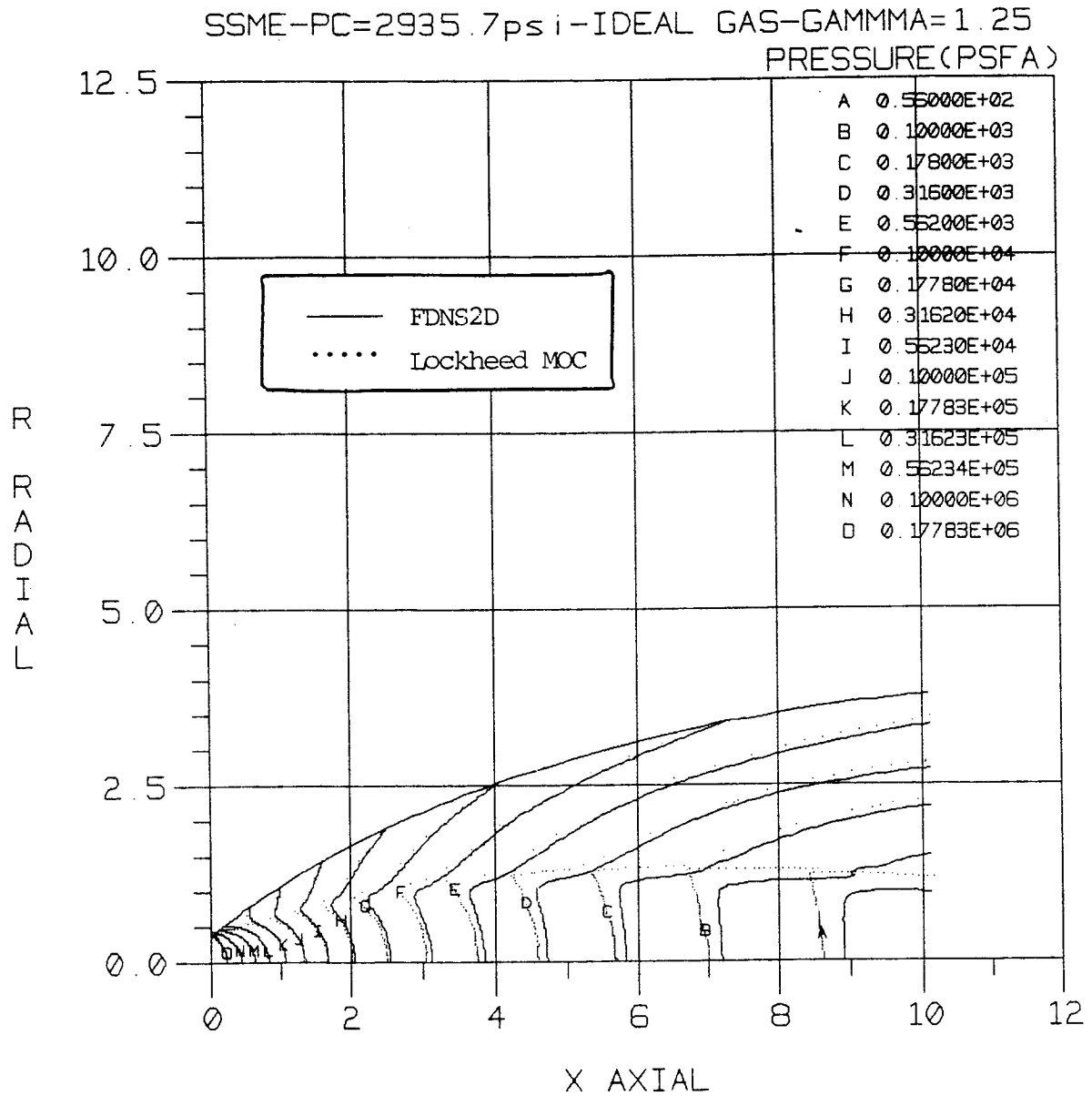(b) ## TEMPERATURE
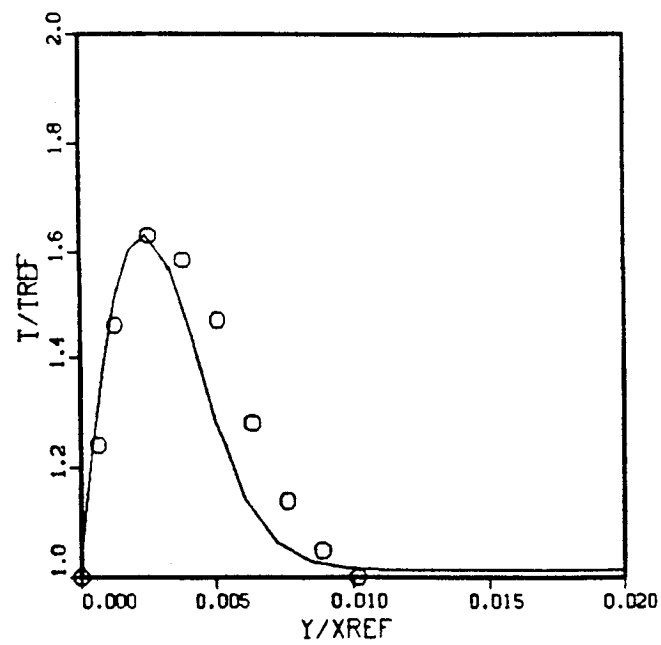
Fig. 2.   FDNS Flat Plate Boundary Layer Solution

Table 3. Comparison of Predicted and Standard Reynolds
          Analogy Factors (S)

Mach Number	Predicted S	Standard S	Percent Error
4.0	0.8105	0.8033	0.90
6.0	0.8101	0.8033	0.85
8.0	0.8097	0.8033	0.80
10.0	0.8090	0.8033	0.71

3.2 SSME Nozzle Flow Fields and Performance Calculations

3.2.1 Perfect Gas

The comparison of 2D axisymmetric perfect gas and adiabatic
wall temperature SSME thrust chamber flowfield solutions (gamma =
1.25, chamber pressure = 2935.7 psia) between the Lockheed MOC
(Ref. 24) and FDNS codes is presented in this section of the
report. Comparisons of the FDNS2D solutions for the pressure,
Mach number and temperature contours to those of the MOC are
shown in Fig. 3. Solid lines represent the FDNS solution, while
the dotted lines are the Lockheed MOC solution. It is clear that
these two solutions are in good agreement. Figure 4 shows a
comparison of predicted center-line and nozzle wall pressure
distributions. A comparison of predicted center-line Mach number
distributions is given in Fig. 5. These results illustrate good
agreement between the two methods. Figure 6 shows the axial
distribution of FDNS2D computed global mass flowrate inside the
nozzle. The overall mass error of the present solution is well
within 1 percent of the inlet mass flow rate. Also, the FDNS2D

(a) Static Pressure Contours

Fig. 3. Perfect Gas SSME Nozzle Calculated Flowfield
Comparison, FDNS2D vs. Lockheed MOC

(b)   Mach Number Contours

Fig. 3.   Perfect Gas SSME Nozzle Calculated Flowfield
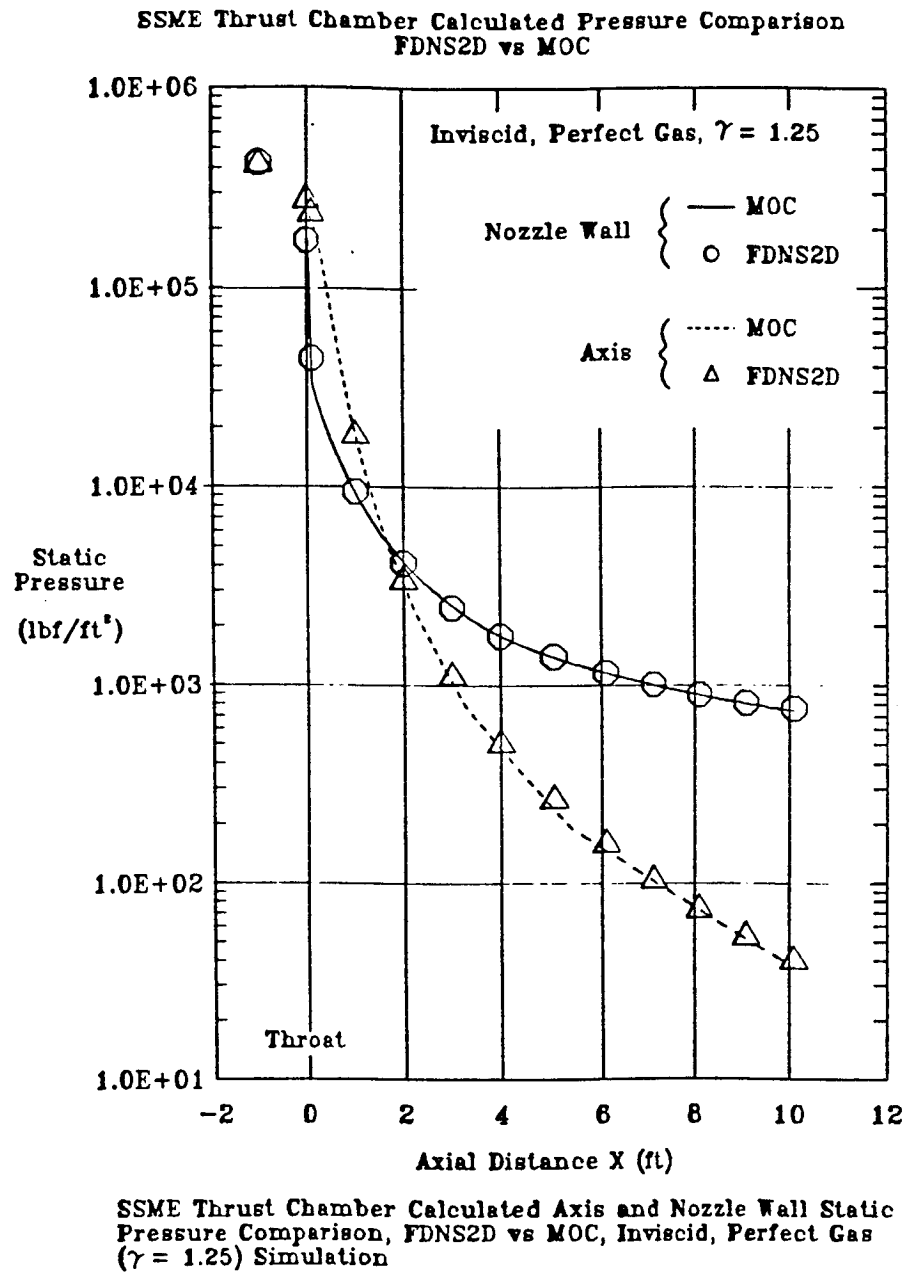   Comparison, FDNS2D vs. Lockheed MOC

39

SSME-PC=2935.7psi-IDEAL GAS-GAMMMA=1.25
T (DEG R)

A	0.12500E+04
B	0.15000E+04
C	0.17500E+04
D	0.20000E+04
E	0.22500E+04
F	0.25000E+04
G	0.27500E+04
H	0.30000E+04
I	0.32500E+04
J	0.35000E+04
K	0.37500E+04
L	0.40000E+04
M	0.42500E+04
N	0.45000E+04
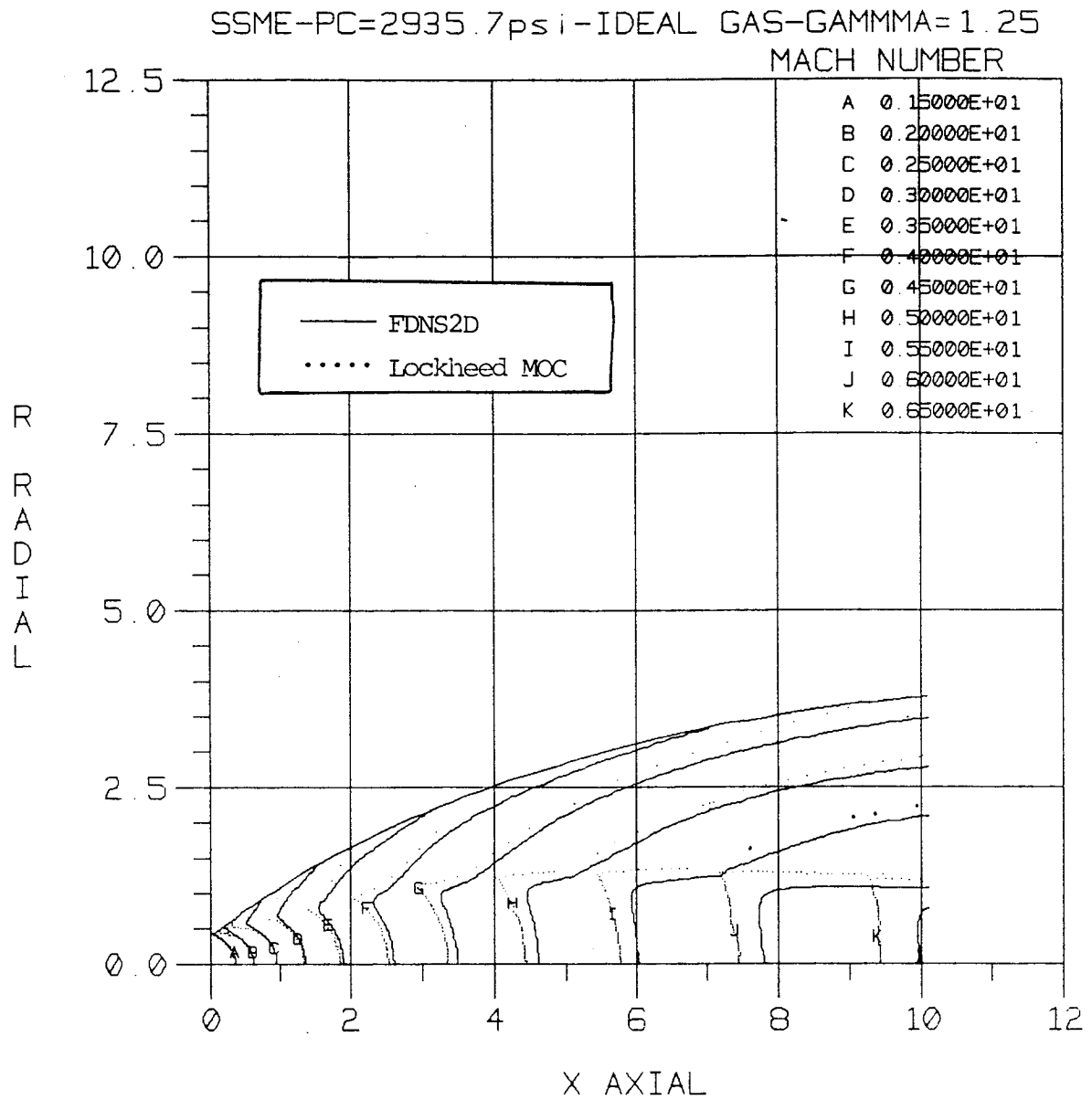
FDNS2D
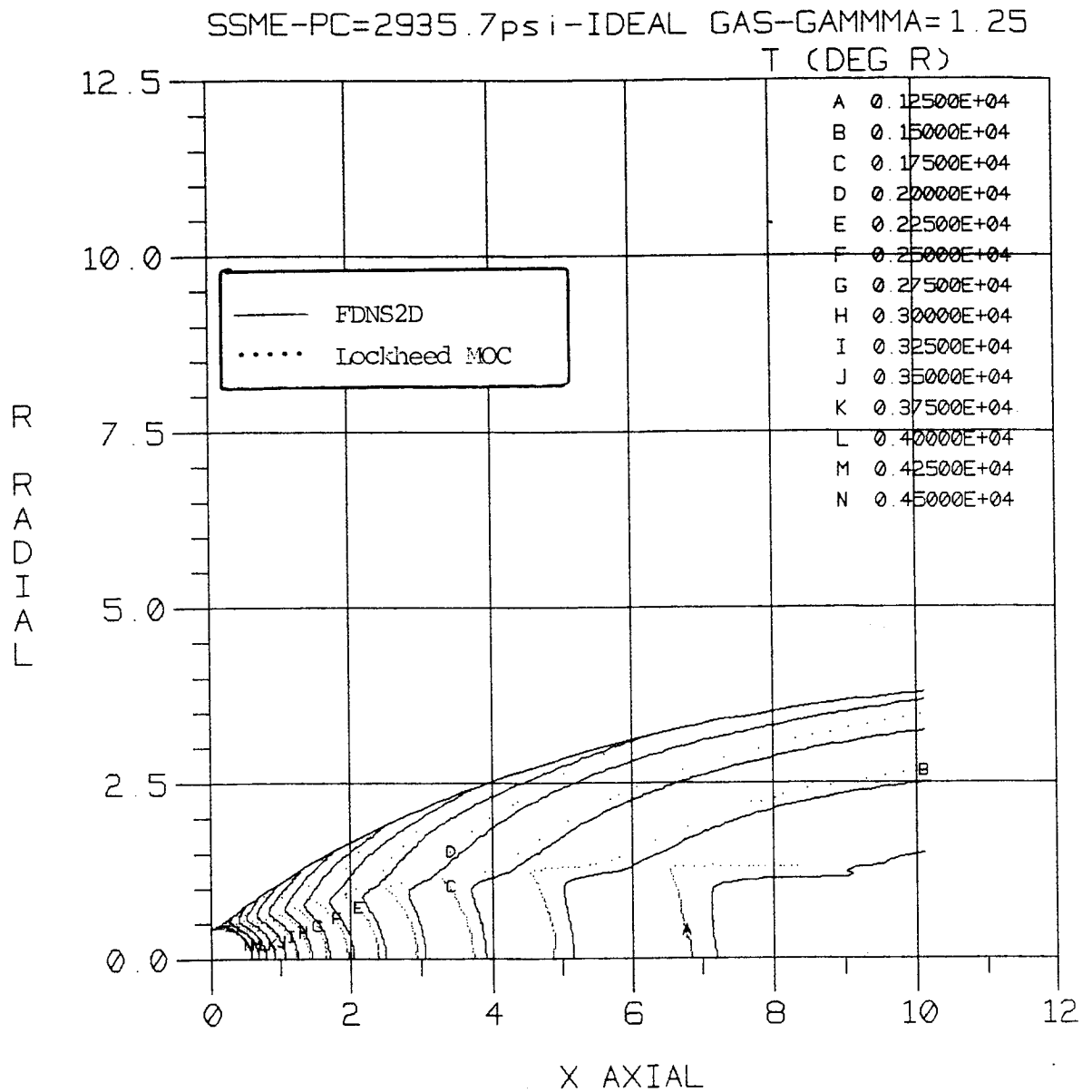
Lockheed MOC

(c)   Static Temperature Contours

Fig. 3.   Perfect Gas SSME Nozzle Calculated Flowfield
Comparison, FDNS2D vs. Lockheed MOC

40

SSME Thrust Chamber Calculated Pressure Comparison
FDNS2D vs MOC
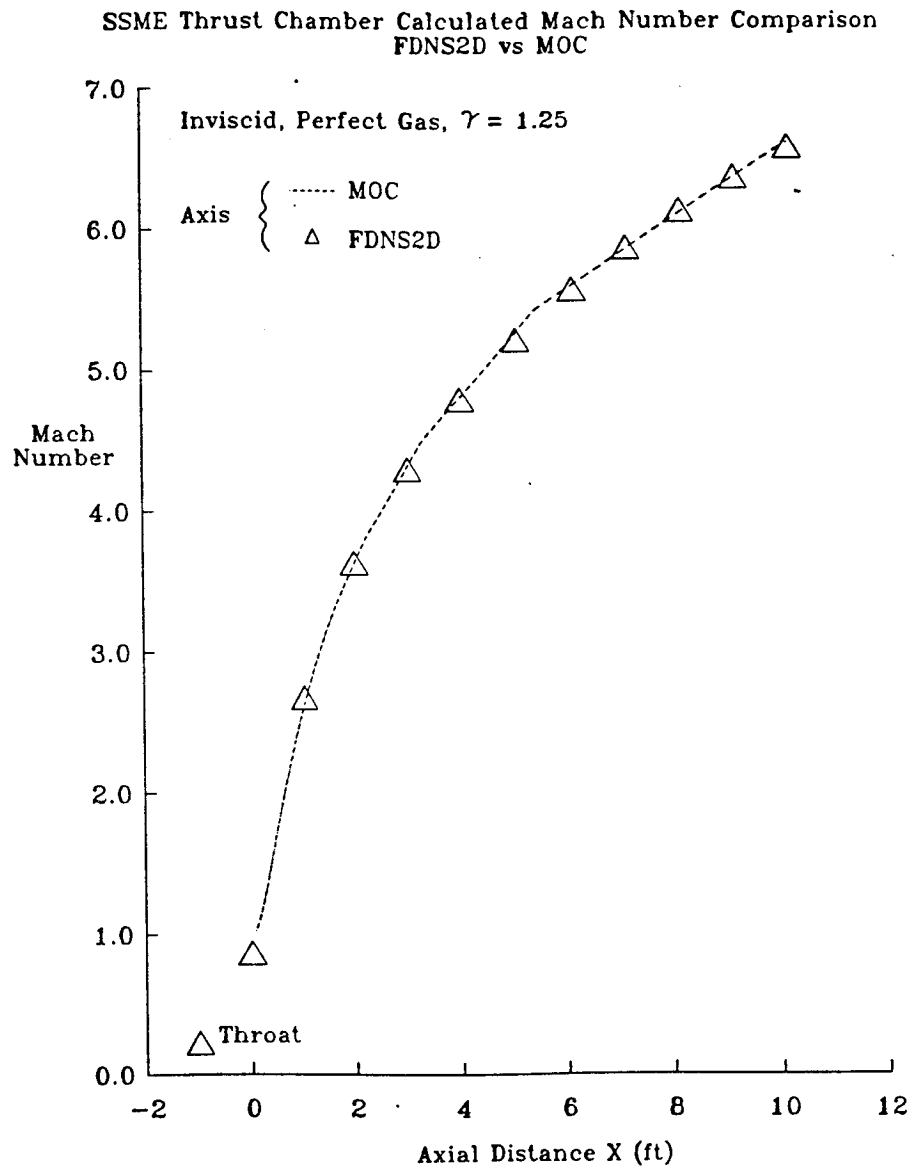
SSME Thrust Chamber Calculated Axis and Nozzle Wall Static
Pressure Comparison, FDNS2D vs MOC, Inviscid, Perfect Gas
($\gamma = 1.25$) Simulation

Fig. 4   Pressure Distribution Comparisons

41

Fig. 5. Center-line Mach number comparisons

MASS FLOW RATE
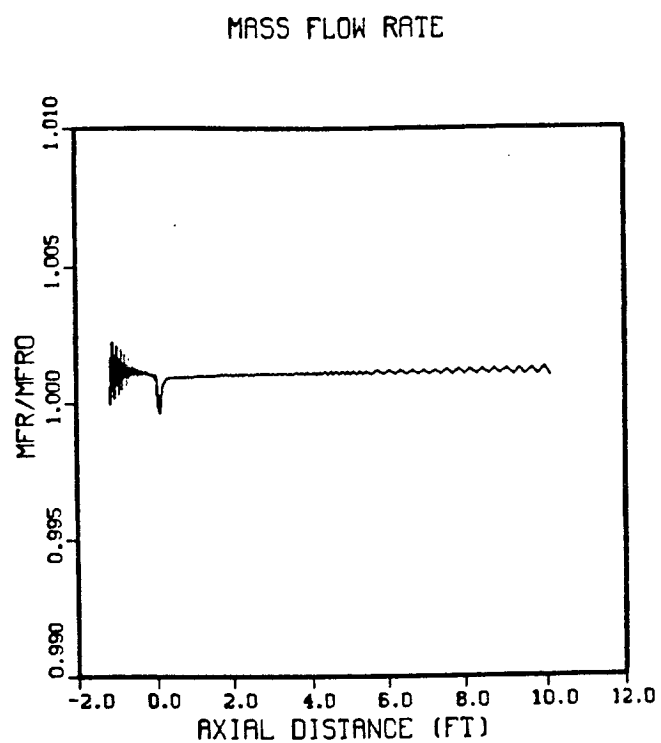
Fig. 6.   FDNS2D SSME Nozzle Flowfield

43

calculation maintains a center-line total pressure loss of less than 1 percent for the SSME nozzle flow computation.

3.2.2   Real Gas/Equilibrium Chemistry

The FDNS equilibrium chemistry model has been tested for a wide range of temperature, pressure and equivalence ratios. The resultant equilibrium species concentrations are in good agreement with CEC (Ref. 1) code calculations. Application of this method to an SSME nozzle flow computation for a 104% power-level test case was performed and compared with the solutions of the TDK/TDE code (Ref. 2) and the measured thrust. Figure 7 shows the predicted flowfield (pressure and temperature contours) which indicate that the induced shock hits the nozzle center line before the exit plane. Computed vs. measured thrust and I_{sp} comparisons are given in Table 4. Both the FDNS equilibrium chemistry procedure and the TDE method over-estimate the thrust and the I_{sp}, as expected.

Comparisons of the Lockheed MOC versus the FDNS SSME flowfield solutions for inviscid, adabatic wall temperature, and real gas (equilibrium chemistry) assumptions for the 104% power level case (chamber pressure = 3126.3 psia) were also made. The real gas MOC solution and the FDNS equilibrium chemistry solutions were in excellent agreement. The only observable difference being that the FDNS solution has not accelerated to the point that the MOC solution has near the nozzle axis at the exit plane.
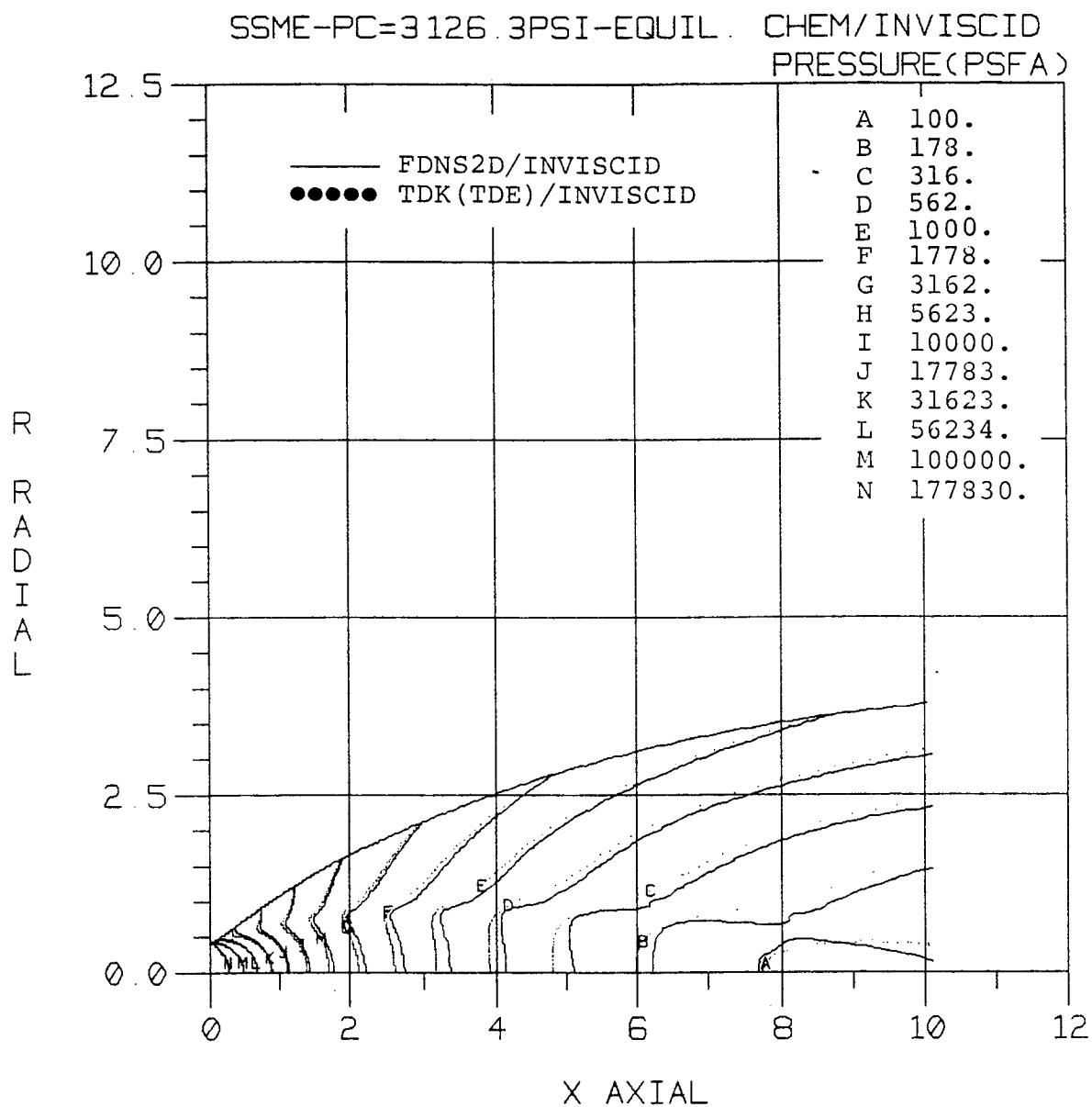
SSME-PC=3126.3PSI-EQUIL. CHEM/INVISCID
PRESSURE(PSFA)

——— FDNS2D/INVISCID
●●●●● TDK(TDE)/INVISCID

A 100.
B 178.
C 316.
D 562.
E 1000.
F 1778.
G 3162.
H 5623.
I 10000.
J 17783.
K 31623.
L 56234.
M 100000.
N 177830.

Fig. 7a.   SSME Thrust Chamber Calculated Flowfield Comparison
FDNS vs. TDK - Equilibrium Chemistry

SSME-PC=3126.3PSI-EQUIL. CHEM/INVISCID
T (DEG R)

A	1750.
B	2000.
C	2250.
D	2500.
E	2750.
F	3000.
G	3250.
H	3500.
I	3750.
J	4000.
K	4250.
L	4500.

FDNS2D/INVISCID
●●●●● TDK(TDE)/INVISCID

R RADIAL

X AXIAL
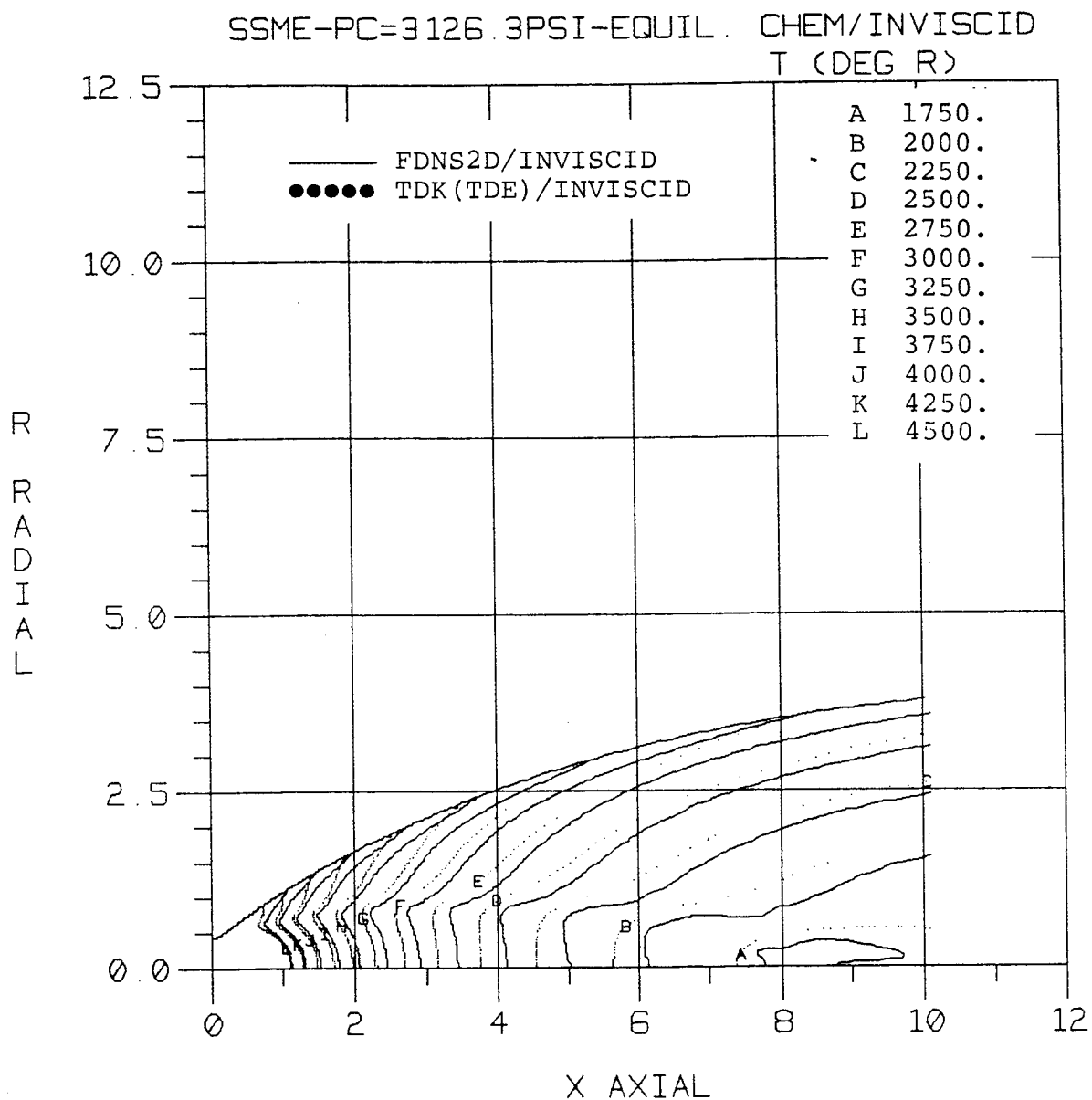
Fig. 7b.   SSME Thrust Chamber Calculated Flowfield Comparison
FDNS vs. TDK – Equilibrium Chemistry

Table 4. SSME Thrust Chamber Performance Predictions Compared to Rocketdyne Measurements

| Parameter | Rocketdyne Measurements Test 9020437 104% | TDK Viscous Predictions | | FDNS2D Viscous Predictions | |
		TDE/BLM 1 Pass[3],[4]	TDK/BLM 1 Pass[3],[4]	Equilibrium Chemistry[4]	Finite Rate Chemistry[4]
Chamber Press., Injector End Static (psia)	3126.25	3126.25	3126.25	3126.25	3126.25
Combustion Total Temp (°R)	———	6652.03	6652.03	6652.03	6652.03
Propellant Flowrate (lbm/sec)	1077.56[1]	1079.87	1079.42	1077.68	1077.68
Vacuum Thrust (lbf)	488,677.[2]	497,537.	495,082.	492,822.	490,052.
Vacuum Specific Impulse (lbf-sec / lbm)	453.51[2]	460.74	458.66	457.30	454.73

Notes:
(1) Derived from facility flowmeters excluding pressurization and overboard leakage flowrates.
(2) Vacuum thrust scaled from site load cell measurement by Rocketdyne.
(3) TDE/TDK injector inlet enthalpies determined by ODE hot gas/gaseous oxygen combustion analysis using Rocketdyne power balance program output: measured pressures and flowrates, and calculated temperatures including heat input from regen cooling cycle.
(4) Specified nozzle wall temperature distribution.

47

3.2.3 Finite Rate Chemistry

Application of the FDNS2D finite rate chemistry procedure to a 104% power level SSME nozzle flow test case was also performed by using a H_2-O_2 eight reaction system. A nine reaction system is shown in Table 5. The last eight of these reactions were used since they are the same as those in TDK, but the rate coefficients used were not the same. The nine reaction system is SECA's recommended set for H_2-O_2 motors and their associated afterburning plumes. The function of the first reaction is to initiate combustion. Whether or not this reaction is used does not significantly affect the predicted performance; however, its use does correctly produce the lag in radical recombination, which occurs in rocket nozzles. Since H_2O and H_2 comprise more than 99.9% of the flow, while finite-rate effects are adjusting the composition, both the 8 and 9 reaction system with FDNS compare well to the TDK results.

Figure 8 shows the predicted flowfield and comparisons with the TDK (Ref. 2) solution in the form of static pressure and temperature contours. Unlike the previous equilibrium chemistry calculations, the induced shock extends to the exit plane without intersecting the nozzle center line. The predicted nozzle thrust and specific impulse for the finite rate chemistry case are also compared with the measured data in Table 4.

3.2.4 SSME Nozzle Performance Calculations

A comparison of SSME thrust chamber performance predicted by the JANNAF standard methodology (TDK code) and FDNS2D for a specified wall temperature distribution and Rocketdyne measured performance for engine 2028, test no. 9020437, at the 104% power

Table 5. Reaction Kinetics Model for H_2-O_2 Propellants

rate = A T^B exp{E/RT}

Units: cm, gm moles, K, sec

No.	Reaction	A	B	E/R
1.	$H_2 + O_2 = OH + OH$	1.7000E13	0	2.4070E4
2.	$OH + H_2 = H_2O + H$	2.1900E13	0	2.5900E3
3.	$OH + OH = O + H_2O$	6.0230E12	0	5.5000E2
4.	$O + H_2 = H + OH$	1.8000E10	1.0	4.4800E3
5.	$H + O_2 = O + OH$	1.2200E17	−0.91	8.3690E3
6.	$M + O + H = OH + M$	1.0000E16	0	0
7.	$M + O + O = O_2 + M$	2.5500E18	−1.0	5.9390E4
8.	$M + H + H = H_2 + M$	5.0000E15	0	0
9.	$M + H + OH = H_2O + M$	8.40000E21	−2.0	0

Third body efficiencies are taken to be the same for all species.

SSME-PC=3126 3PSI-FINITE RATE CHEMISTRY
T (DEG R)

FDNS2D/VISCOUS
●●●●● TDK/INVISCID

A	1750.
B	2000.
C	2250.
D	2500.
E	2750.
F	3000.
G	3250.
H	3500.
I	3750.
J	4000.
K	4250.
L	4500.

X AXIAL

SSME-PC=3126 3PSI-FINITE RATE CHEMISTRY
PRESSURE(PSFA)

FDNS2D/VISCOUS
●●●●● TDK/INVISCID

A	100.
B	178.
C	316.
D	562.
E	1000.
F	1778.
G	3162.
H	5623.
I	10000.
J	17783.
K	31623.
L	56234.
M	100000.
N	177830.

X AXIAL
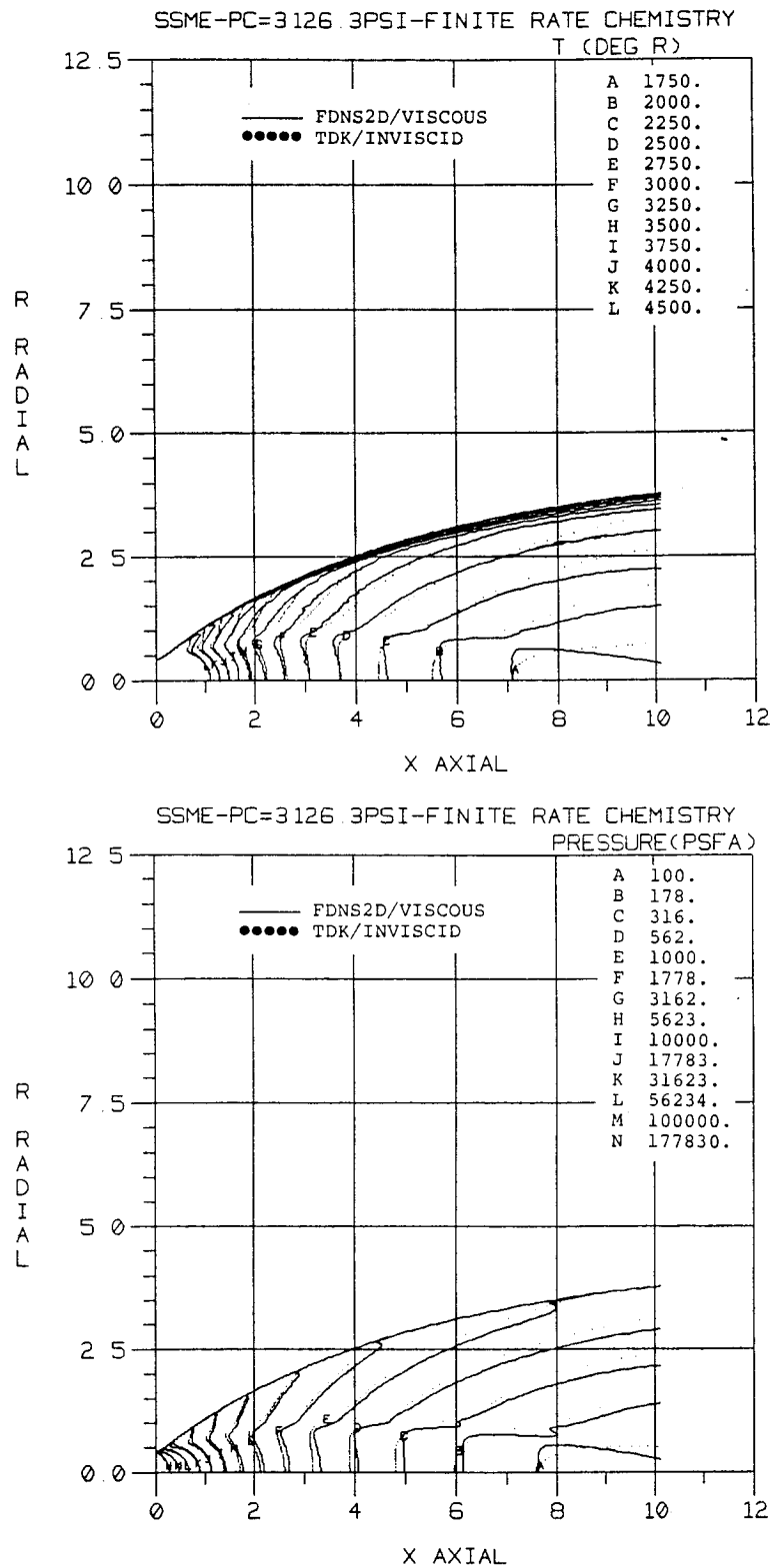
Fig. 8.   Temperature and Pressure Profiles for FDNS and TDK
Finite Rate Solutions

level is shown in Table 4. For the TDK predictions shown in
Table 4 both the two dimensional equilibrium (TDE) and two
dimensional kinetic (TDK) analyses are viscous and consider
boundary losses, [i.e., the boundary layer module (BLM), and a
specified wall temperature distribution] and also consider heat
input from the regenerative cooling cycle. The FDNS2D
predictions are viscous with the specified wall temperature
distribution taken from (Ref. 25) and account for the boundary
layer loss. Notice that all of the performance predictions
presented in Table 4 start from identical chamber pressure and
combustion total temperature. The FDNS2D equilibrium chemistry
result for vacuum specific impulse is approximately 3.8 sec.
higher than the Rocketdyne result, which is derived from test
data. The FDNS2D finite rate chemistry analysis demonstrates
that the SSME finite rate/equilibrium chemistry specific impulse
loss is approximately 2.6 sec., and the final FDNS2D result for
predicted vacuum specific impulse is within 1.2 sec. or 0.3% of
the reported Rocketdyne measurement.

3.3 Plume Flow Fields

3.3.1 SSME Nozzle and Plume

Flow in the SSME nozzle was predicted for the grid shown in
Fig. 9. The grid size was 141 x 61. The flow was assumed to be
for an ideal gas with a constant gamma of 1.25. The near
equilibrium conditions which exist in this nozzle exhibit a
variable gamma, especially near the throat, but MOC solutions run
at constant gamma with the gamma evaluated as the exit plane
value for a shifting equilibrium flow agree well with real gas
solutions. This experience was used in selecting the 1.25 value
for gamma. A solution is also shown for gamma of 1.30 to
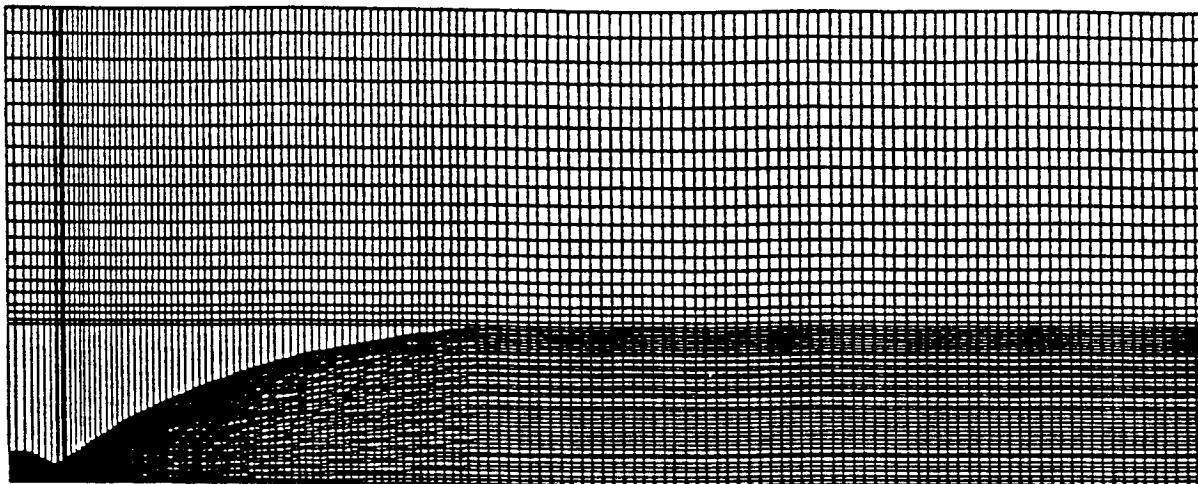
Fig. 9.   Computational Grid for the SSME (141 x 61)
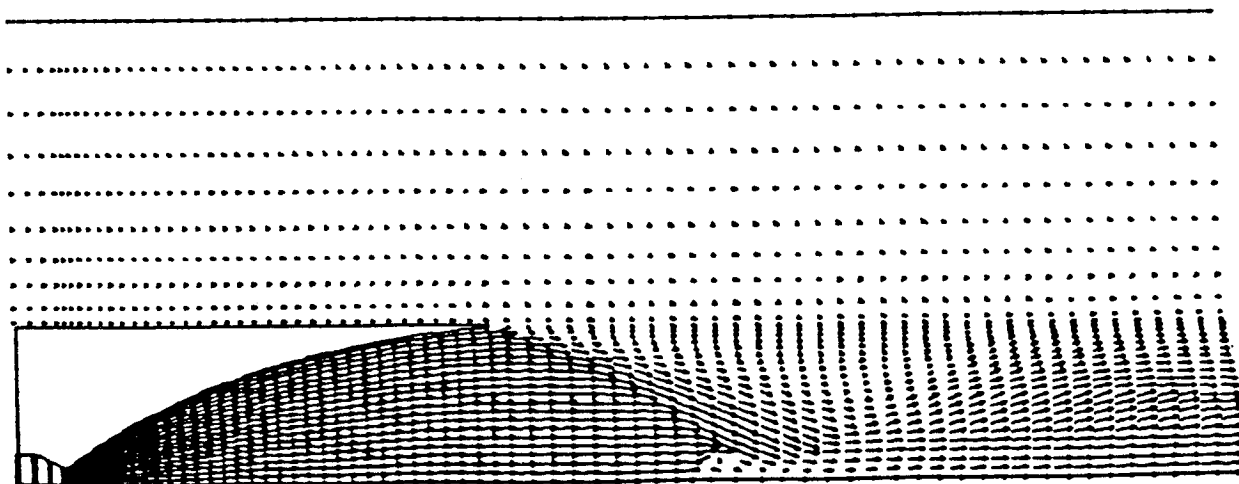
Fig. 10.   Velocity Vectors for the SSME with $\gamma = 1.25$

indicate sensitivity. Velocity vectors are shown in Fig. 10; convergence histories are shown in Fig. 11. Pressure, temperature, density, and Mach number profiles are shown in Figs. 12 and 13. These plots indicate the location of the nozzle shocks which are in good agreement with MOC results. A crucial test of a CFD solution for propulsion nozzle flows is the ability to correctly account for the differences in centerline and wall pressure distributions. These distributions, which are shown in Fig. 14, indicate excellent agreement with values obtained from an MOC solution. MOC solutions are known to properly predict such flows. The centerline Mach number profile is given in Fig. 15. Similar results are given for the gamma 1.30 solution in Figs. 16 through 20. The change of gamma from 1.25 to 1.30 has very little effect on the solution. The calculations were performed using an extended $k-\epsilon$ turbulence model with wall functions. The turbulence model extension was made to better simulate flows over back steps; it is represented by the last term in Eq.(34) which is discussed in Section 2.2.2 of the report. The velocity vector plots indicate large, realistic velocities near the walls in both cases.

Notice that the calculated velocity vectors for both cases indicate a non-realistic recirculation zone behind what should be a Mach disc outside of the nozzle. Further grid refinements and/or turbulence model improvements, which are discussed subsequently are needed to improve the flowfield prediction past the triple point.

a.   Variable Specific Heat Ratio Effect on SSME Nozzle and Plume Flow

γ = 1.25
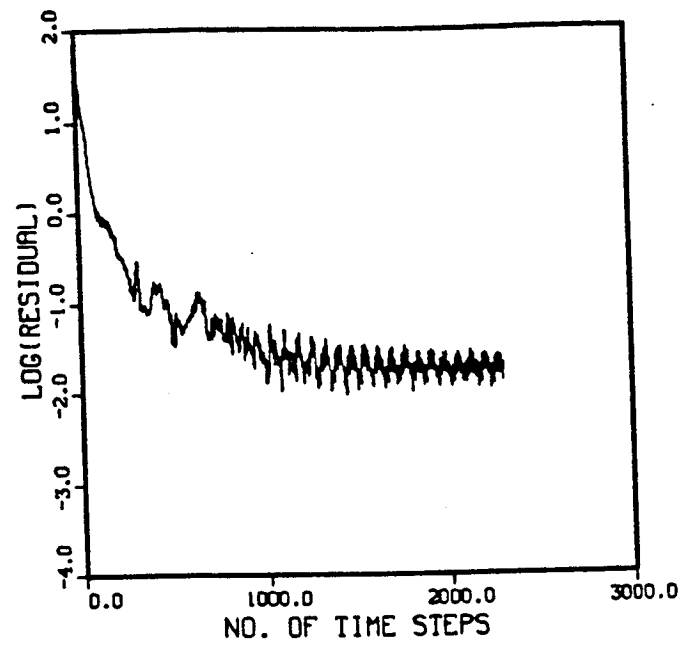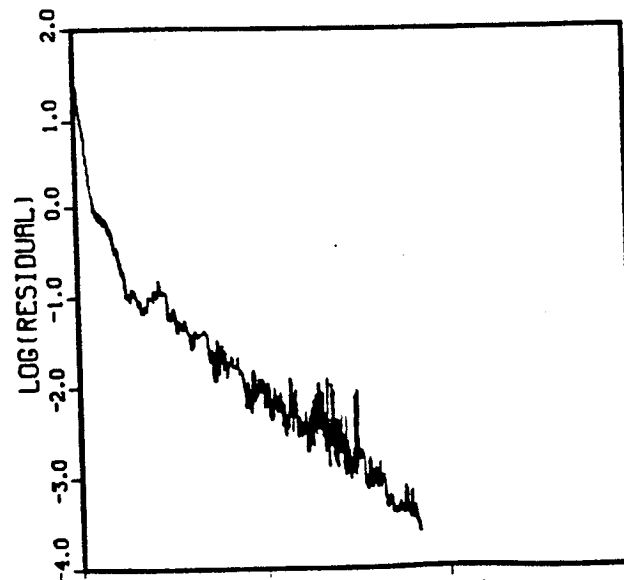
γ = 1.30

Fig. 11.   Convergence Histories for Two SSME Cases

54
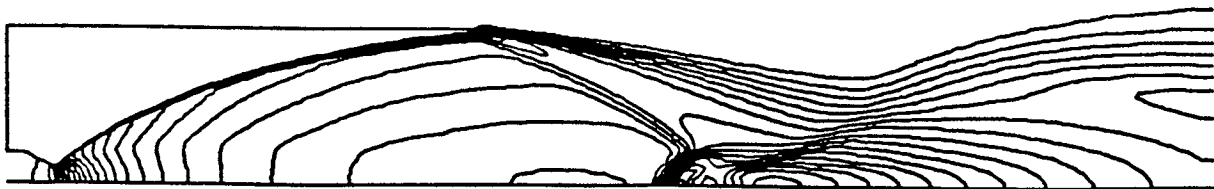
Pressure

Temperature

Fig. 12. Pressure and Temperature Contours for SSME with
$\gamma = 1.25$
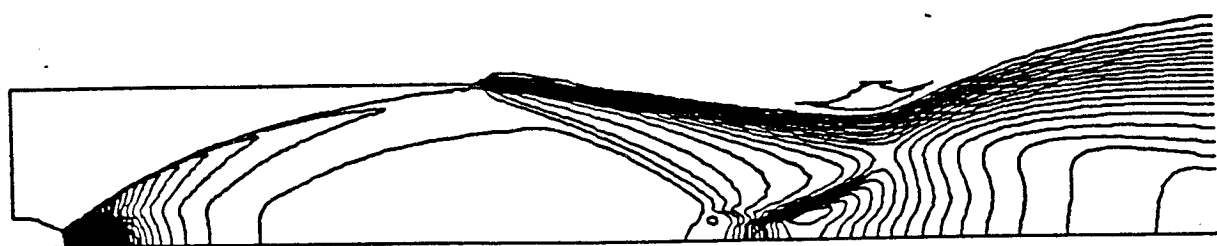
Density

Mach No.

Fig. 13.   Density and Mach Number Contours for SSME with $\gamma = 1.25$
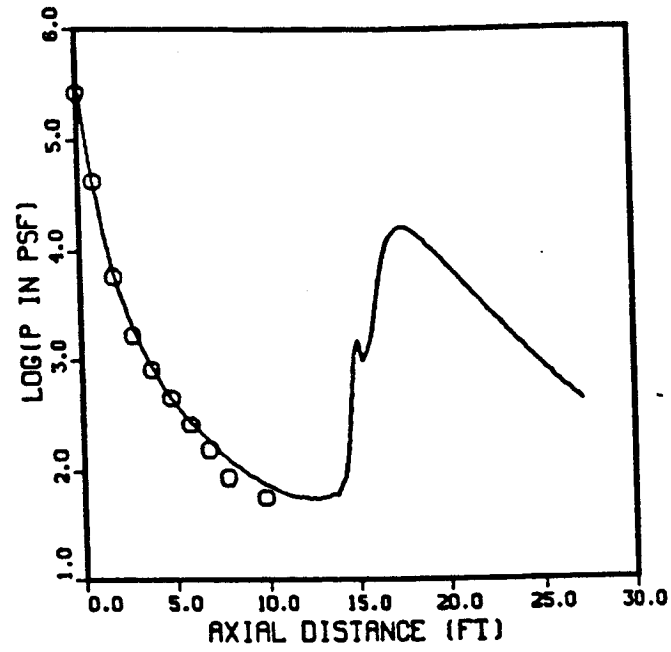
Center Line Pressure
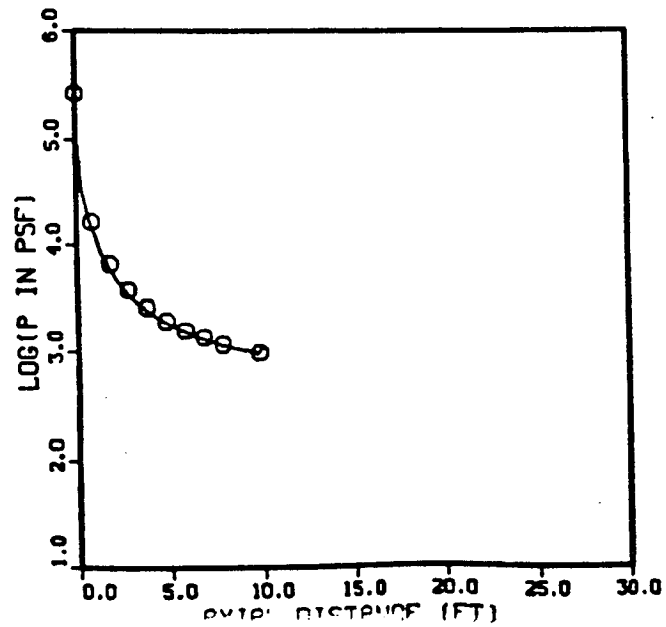
Wall Pressure

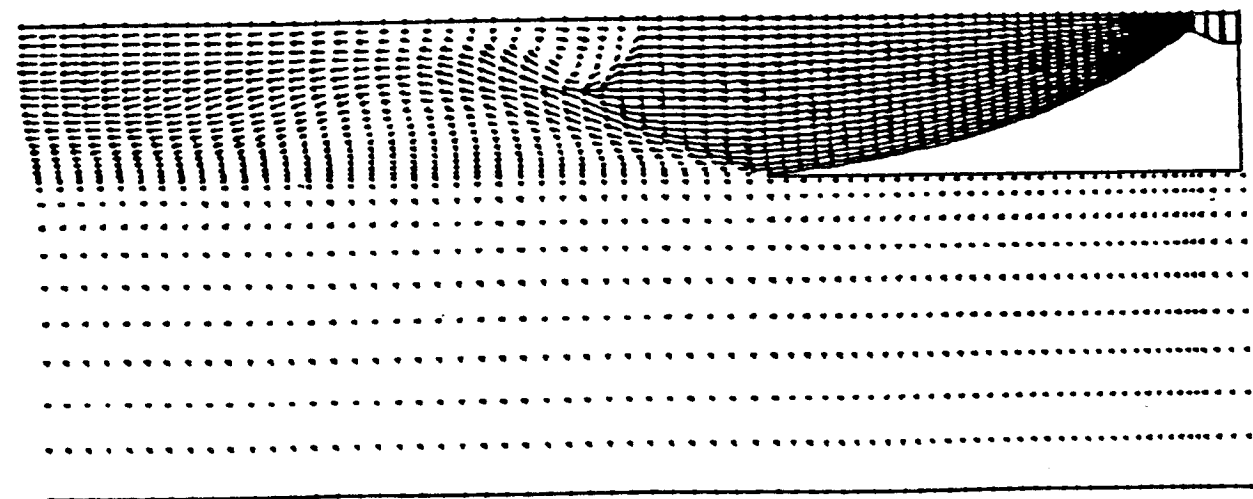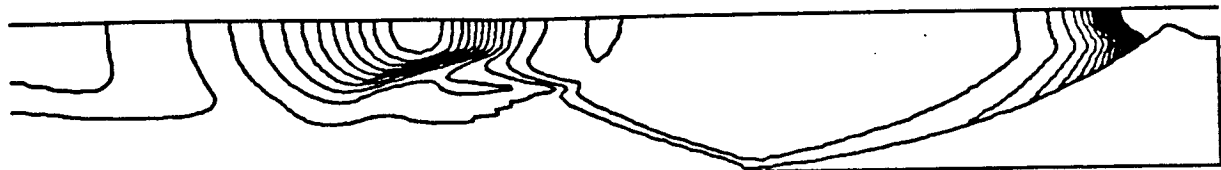Fig. 14. Pressure Distributions for SSME with $\gamma = 1.25$
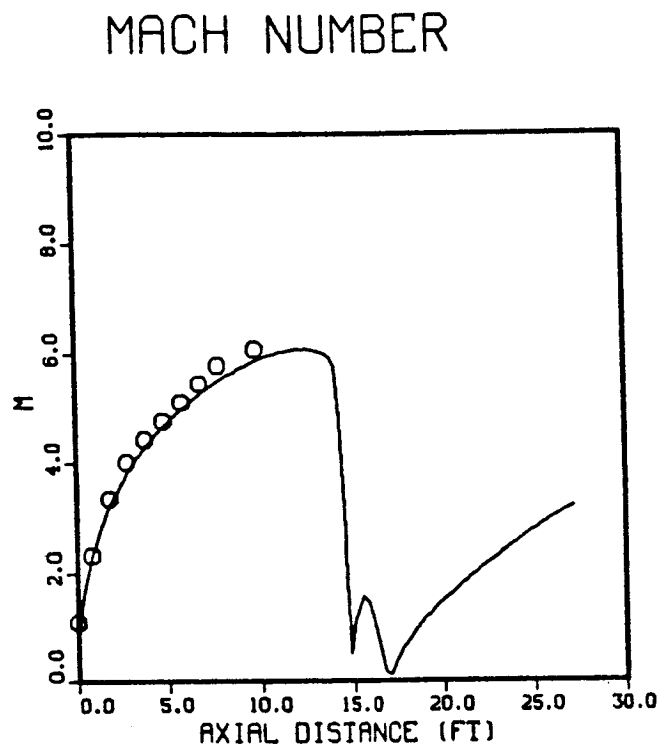
MACH NUMBER

Fig. 15.   Mach Number Distribution Along Centerline for the SSME
with $\gamma = 1.25$
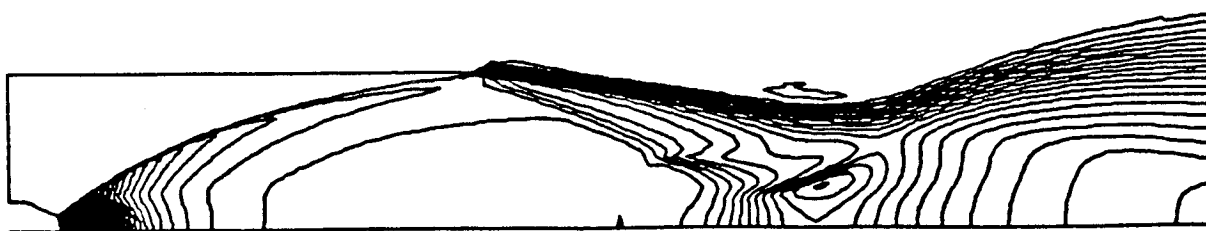
Temperature

Density

Fig. 17. Temperature and Density Contours for the SSME with
$\gamma = 1.30$

60
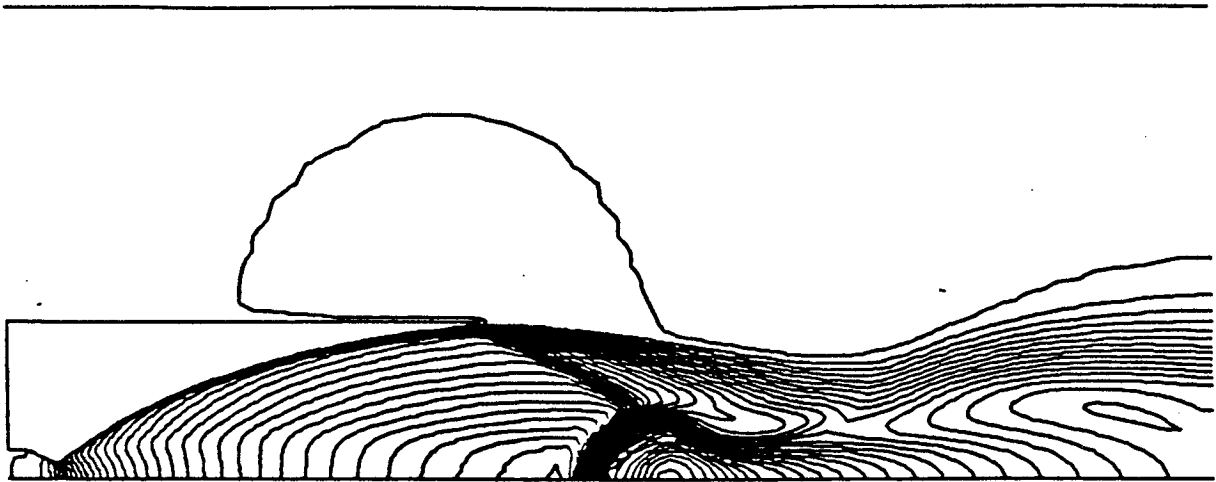
Mach No.

Streamlines

Fig. 18. Mach Number Contours and Streamlines for SSME with
        $\gamma = 1.30$

Centerline Pressure

Wall Pressure
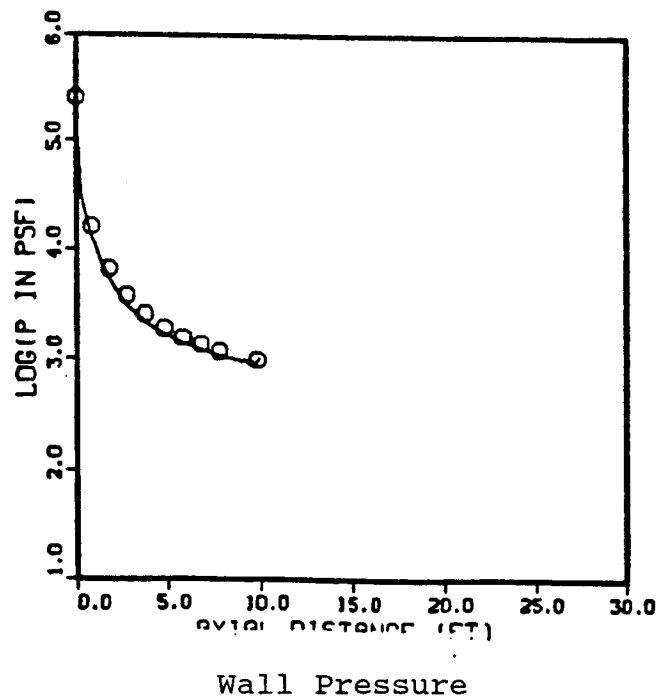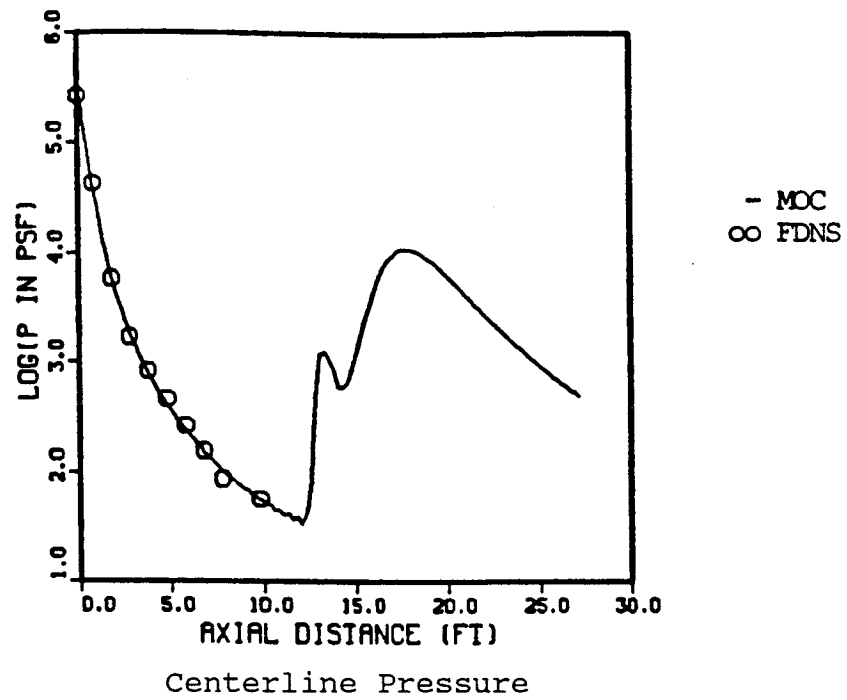
Fig. 19. Centerline Pressure Distributions for SSME with γ = 1.30

MACH NUMBER

Fig. 20.   Centerline Mach Number Distributions for SSME with
           $\gamma = 1.30$

To further test the gamma effect, a variable gamma test case was also investigated. For this case, the external plume region is considered. Four species, namely N_2, O_2, H_2 and H_2O, are involved in the species transport computations. Only H_2 and H_2O are used inside the nozzle while N_2 and O_2 are assigned for the freestream region. Chemical reactions are not activated here so that the molecular weight is kept constant throughout the nozzle. Gamma and C_p are evaluated based on temperature dependent fluid properties. This gives a variation of gamma from 1.18 inside the chamber to 1.255 near the nozzle exit. A grid size of 201 x 81 and a time step size of 0.001 were used for this case. The inclusion of the variable gamma effect slows down the solution convergence rate. Around 4000 time steps are required to obtain a steady state solution. The predicted velocity vectors and temperature contours are shown in Fig. 21. The Mach disc size and location are very close to the features observed in SSME nozzle static firings. However, there is still a small region of reversed flow downstream of the Mach disc which inclines the Mach disc.

One possible reason for the inclination of the predicted Mach disc described above may be due to the dissipation scheme employed for and the time derivative term included in the continuity equation. To evaluate these effects, a conical nozzle flow problem was investigated using the 4th-order dissipation parameter reduced 5 times for the continuity equation (the original 4th-order damping parameter is 0.01). A grid size of 201 x 81 and a time step size of 0.001 were used in the simulation. Two cases with and without the time derivative term included in the continuity equation were computed. Results of these two cases are given in Figs. 22a and 22b respectively. It is clear that the exclusion of the time derivative term in the
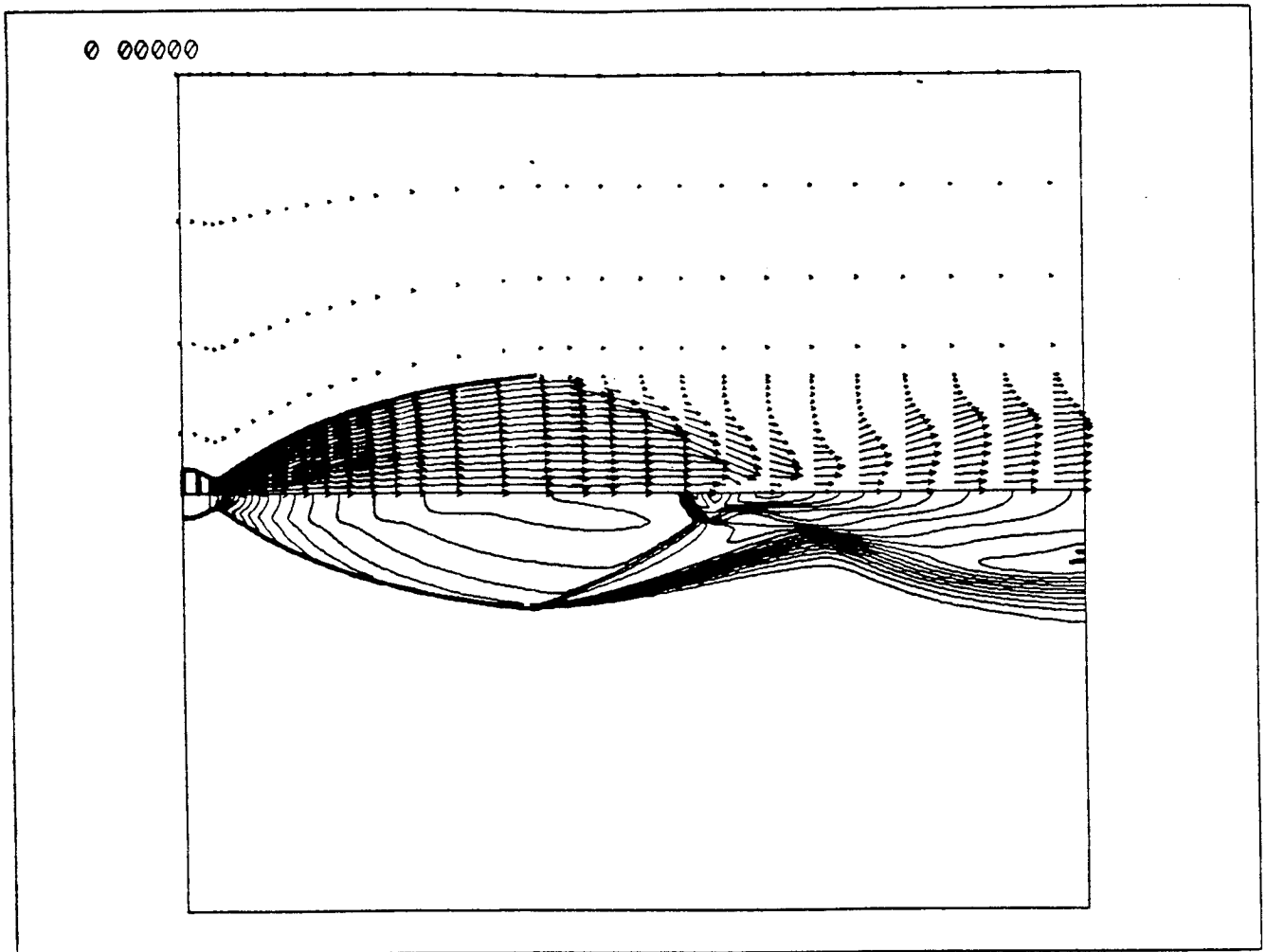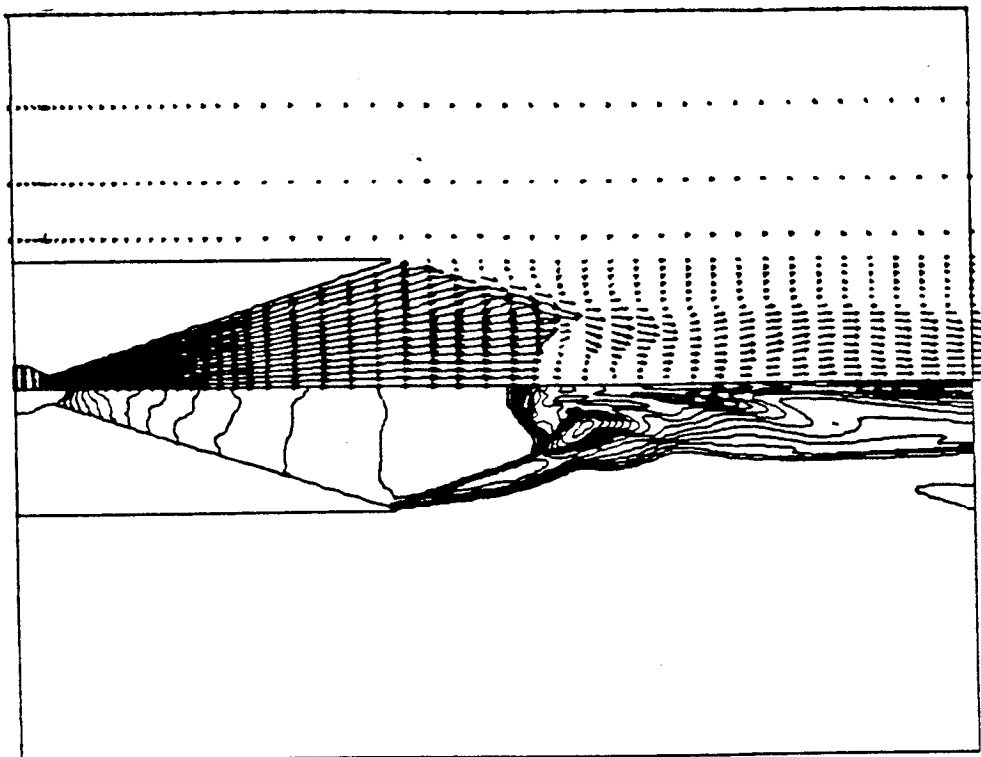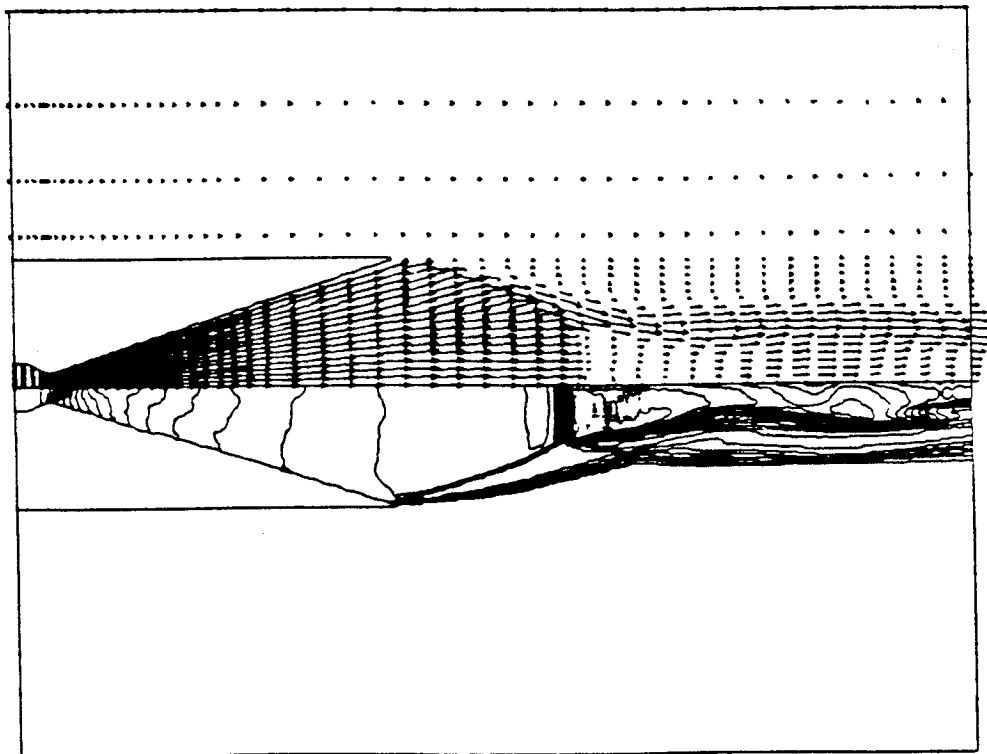
Fig. 21. SSME Nozzle Flow Solution Velocity Vectors and
          Temperature Contours for Variable Specific Heat Ratio

(a)   Solution With Time Derivative

(b)   Solution Without Time Derivative

Fig. 22   Conical Nozzle Flow Solutions. (Laminar Flows)

continuity equation makes the Mach disc straight and eliminates flow recirculation downstream of the disc. The exclusion of the time derivative term enforces steady state mass conservation and contributes to a steady state solution of the Mach disc. This proves that the accuracy of the mass conservation calculation critically affects the Mach disc shape. However, this treatment reduces but does not eliminate the recirculation zone downstream of the Mach disc of the SSME nozzle plume.

b. Resolution of the Mach Disc

Axisymmetric flows with Mach discs are accurately predicted with FDNS for approach Mach numbers less than or equal 3. Figure 23 shows the predictions for an exit Mach number of 2 discharge into still air. A shadowgraph from Ref. 26 is also reproduced in this figure at the same scale. Notice that the flowfield is reasonable and that the disc is predicted to be in approximately the correct location. Figure 24 presents solutions for a conical nozzle and for separation in a conical nozzle. The shape of the predicted disc and the subsonic flow downstream of the disc are reasonable, although no test data are available for comparison to this case.

For flows approaching the Mach disc which are faster than about Mach 3, strong recirculation zones form behind the disc, which is an erroneous result. Many of the parameters which influence the performance of the computational algorithm were investigated to determine what controls the calculated behavior of the subsonic flow region behind a Mach disc. Eliminating the unsteady term in the continuity equation when it is used as part of the pressure correction term, improves the Mach disc prediction. Pressure profiles and velocities for such a
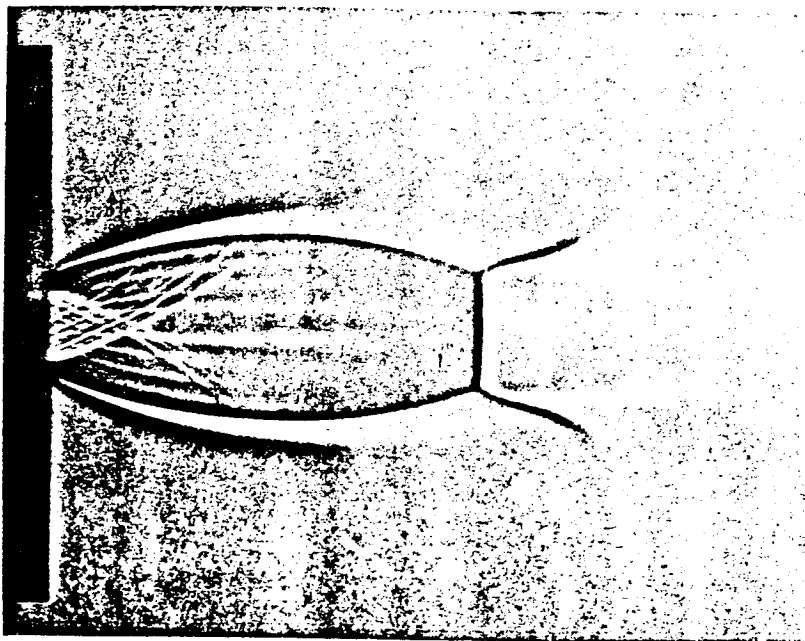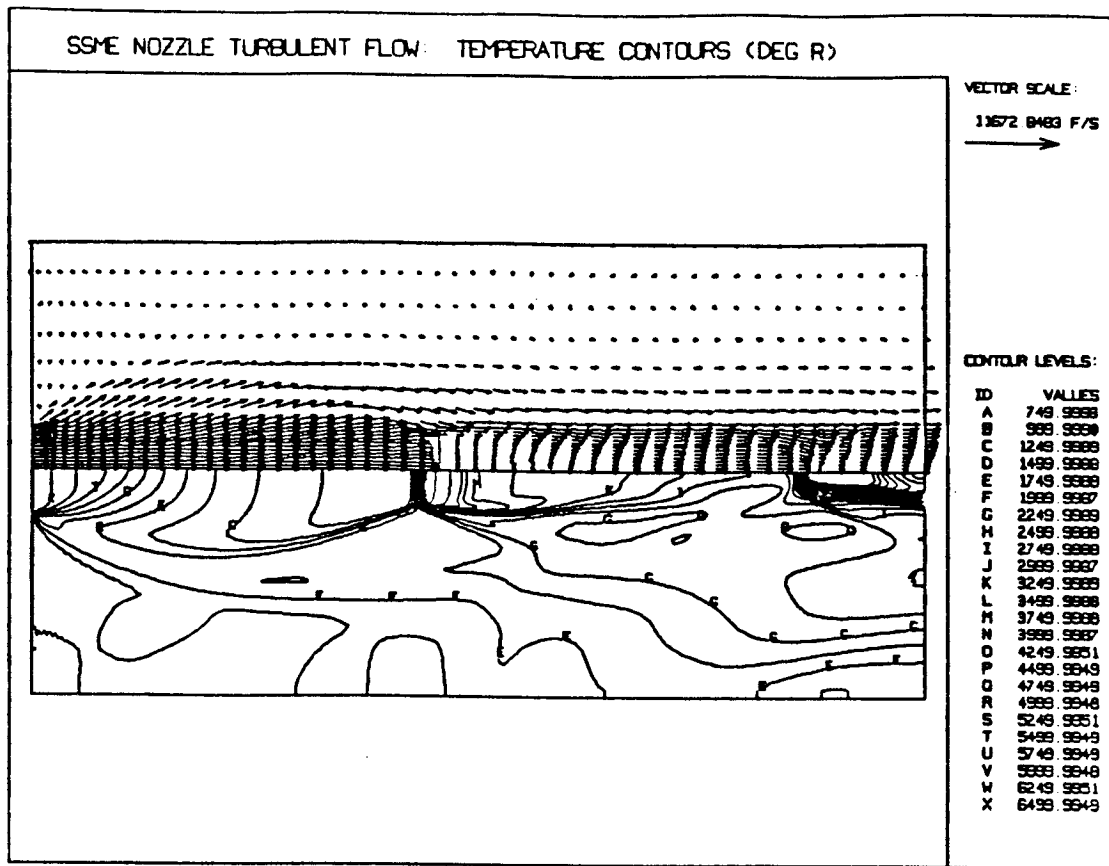
SSME NOZZLE TURBULENT FLOW TEMPERATURE CONTOURS (DEG R)

VECTOR SCALE:

11672 8483 F/S

CONTOUR LEVELS:

ID	VALUES
A	749.9998
B	999.9990
C	1249.9988
D	1499.9988
E	1749.9988
F	1999.9987
G	2249.9989
H	2499.9988
I	2749.9988
J	2999.9987
K	3249.9988
L	3499.9988
M	3749.9988
N	3999.9987
O	4249.9951
P	4499.9949
Q	4749.9949
R	4999.9948
S	5249.9951
T	5499.9949
U	5749.9949
V	5999.9948
W	6249.9951
X	6499.9949

Fig. 23. Shadowgraph of Mach 2.0 Discharging Into Still Air

Velocity Vector

Temperature

Pressure
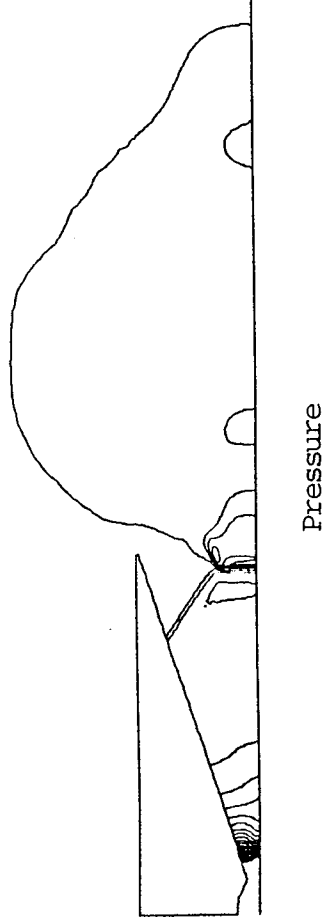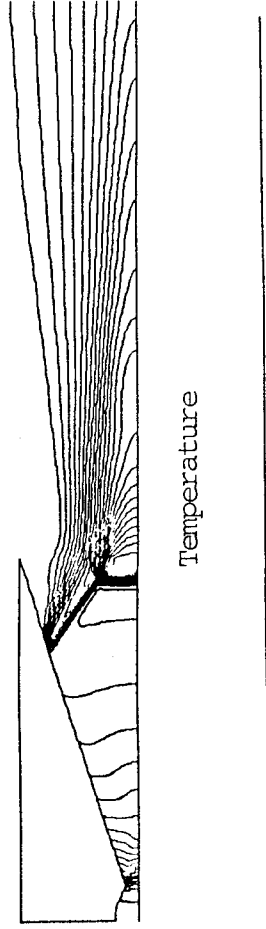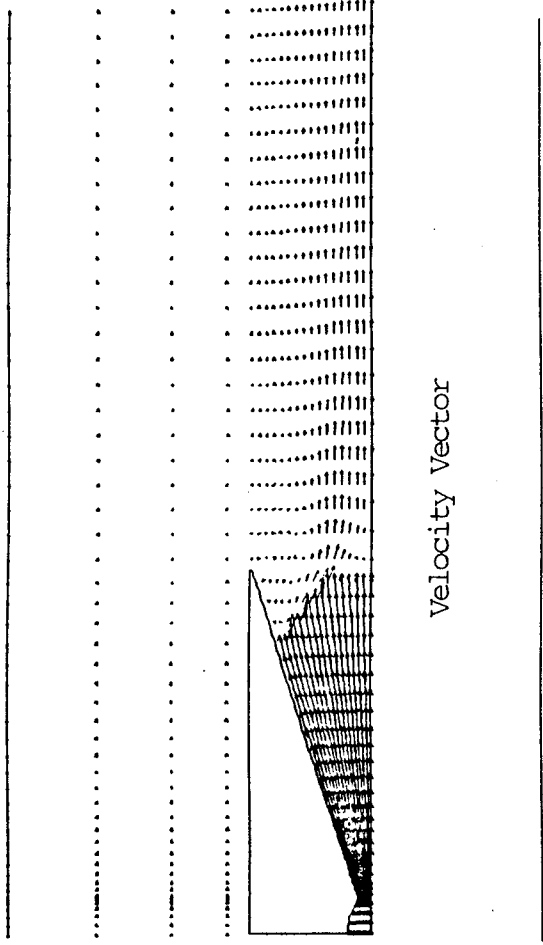
Fig. 24. FDNS Conical Nozzle Solutions

69

prediction are shown in Fig. 25 for the SSME at sea level. Temperature profiles are shown in Fig. 26. Notice that there is some recirculation behind the disc. Normal windward differencing with FDNS allows the pressure to be central differenced. Eliminating this feature of the algorithm also improves strong Mach disc predictions, at the expense of slightly smearing the shocks. When the pressure is differenced in a completely windward fashion, the solution must be started by first forcing all of the axial velocity components to be positive, then relaxing this requirement. Temperature profiles and velocities predicted using such an algorithm are shown in Fig. 27, notice the normal shock appears to be predicted as a strong oblique shock. The lip shock and the Mach disc predicted by this method do not have exactly the correct shape, but the entire predicted flowfield appears to have the proper flow direction. It is recommended that windward differencing on the pressure be used for describing strong Mach discs, unless it is shown that the Mach disc structure strongly affects other critical plume features. The recommended solution is reasonably accurate and allows other important plume related phenomena, like radiation and impingement, to be accurately predicted.

c. Effects of Numerical Schemes on Mach Disc Structure

It was demonstrated above that the FNDS method can predict reasonable Mach disc structure for a conical nozzle with the same expansion ratio and operating conditions at sea-level. However, the same scheme failed to give a correct Mach disc shape for the SSME contoured nozzle plume. The basic difference between the flow features of the conical nozzle and the actual SSME nozzle is the large radial gradients produced by the bell-shaped wall of the SSME while the exit flow properties of the conical nozzle remain almost 1-D in nature. Several different treatments of
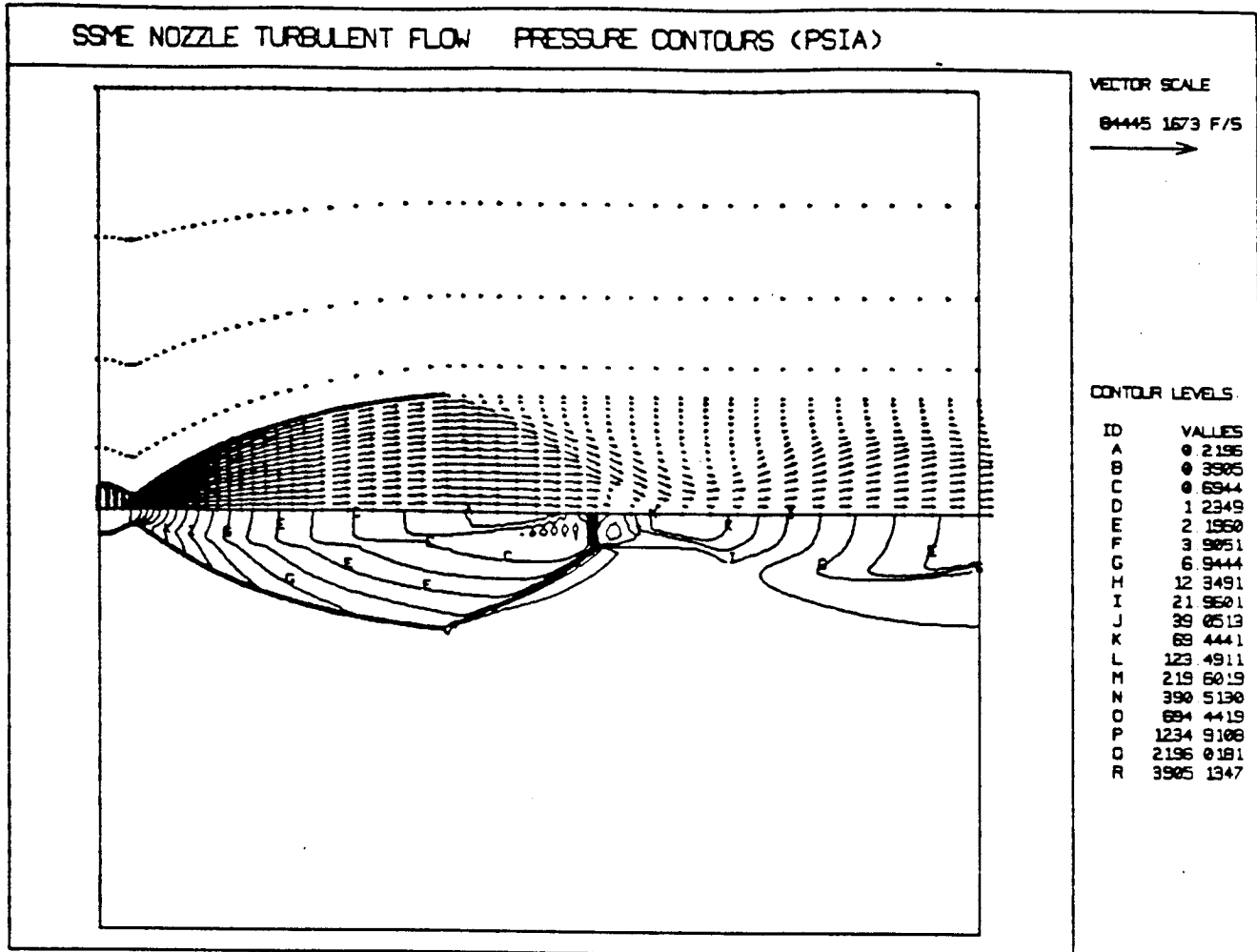
70

SSME NOZZLE TURBULENT FLOW   PRESSURE CONTOURS (PSIA)

VECTOR SCALE

84445 1673 F/S

CONTOUR LEVELS

ID	VALUES
A	0.2196
B	0.3905
C	0.6944
D	1.2349
E	2.1960
F	3.9051
G	6.9444
H	12.3491
I	21.9601
J	39.0513
K	69.4441
L	123.4911
M	219.6019
N	390.5130
O	694.4419
P	1234.9108
Q	2196.0191
R	3905.1347

Fig. 25.   FDNS SSME Nozzle and Plume Flowfield at Sea Level,
          Pressure Contours and Velocity Vectors
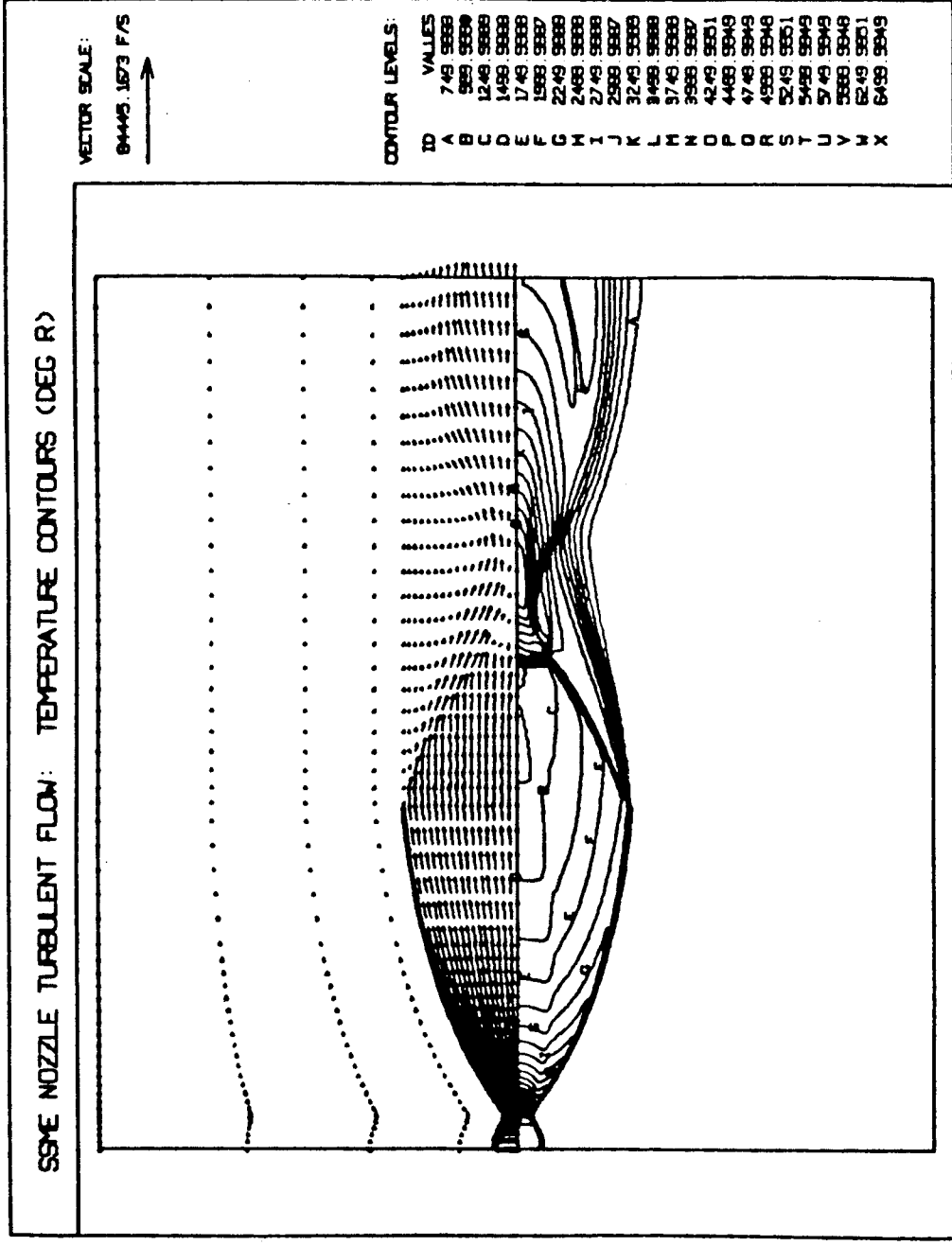
71

Fig. 26. FDNS Nozzle and Plume Flowfield at Sea Level,
Temperature Contours and Velocity Vectors

SSME NOZZLE TURBULENT FLOW   TEMPERATURE CONTOURS (DEG R)

VECTOR SCALE

84445 1673 F/S

CONTOUR LEVELS	
ID	VALUES
A	749.9983
B	999.9990
C	1249.9988
D	1499.9986
E	1749.9998
F	1999.9987
G	2249.9999
H	2499.9988
I	2749.9988
J	2999.9997
K	3249.9988
L	3499.9988
M	3749.9996
N	3999.9997
O	4249.9951
P	4499.9943
Q	4749.9949
R	4999.9948
S	5249.9951
T	5499.9949
U	5749.9949
V	5999.9948
W	6249.9951
X	6499.9949
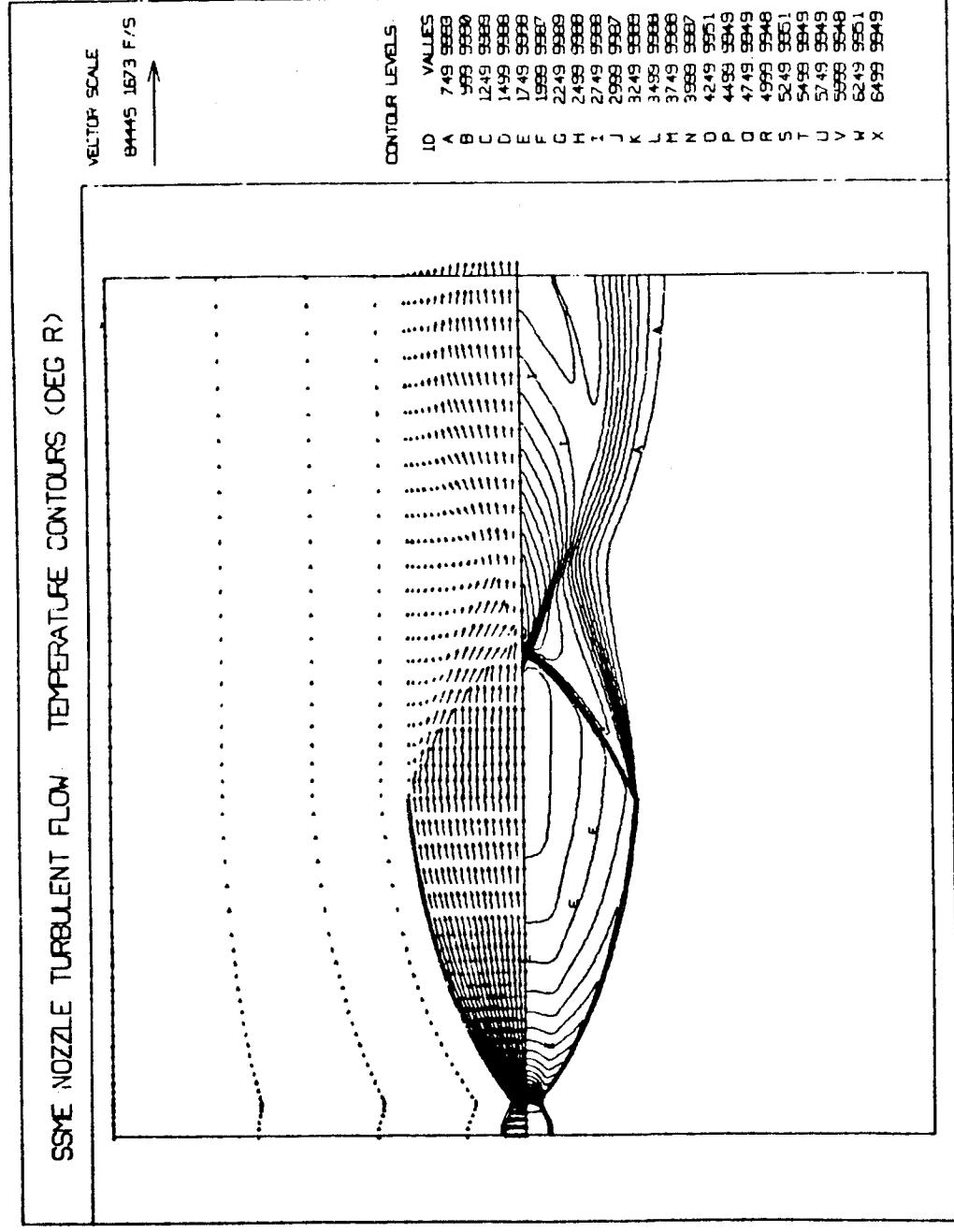
Fig. 27. FDNS Nozzle and Plume Flowfield at Sea Level,
Temperature Contours and Velocity Vectors, Windward
Differncing

73

numerical fluxes have been tested which are summarized below:

(a)   Conservative upwind scheme based on local pressure
       variations predicted with central differenced pressure.

(b)   Conservative upwind scheme (including pressure
       gradients) based on the local pressure variations.

(c)   Scheme (a) using Mach number as the upwind parameter.
       (fully upwind for supersonic flows)

(d)   Scheme (b) using Mach number as the upwind parameter.
       (fully upwind for supersonic flows)

(e)   Fully upwind scheme for the convection terms while
       keeping the pressure central differenced.

All these cases were tested using the variable gamma option
with a grid size of 201 x 81 and time step size of 0.0005. An
extended two-equation turbulence model was used in this study.
Scheme (a) is the case reported previously, which produced a
large recirculation region behind the disc. Scheme (b) improves
the predicted Mach disc structure (Fig. 28) with the drawback
that the residuals do not go down monotonically which indicates
that a steady state solution has not been reached. The flow
behind the disc is still recirculating. The entire Mach disc
disappeared when scheme (d) was applied (Fig. 29). The excessive
smearing of the induced shock inside the nozzle caused by strong
damping of scheme (d) is apparent from Fig. 29. Schemes (c) and
(e) produce essentially the same result (Fig. 30). Very good
convergence behavior was also obtained for these two cases. This
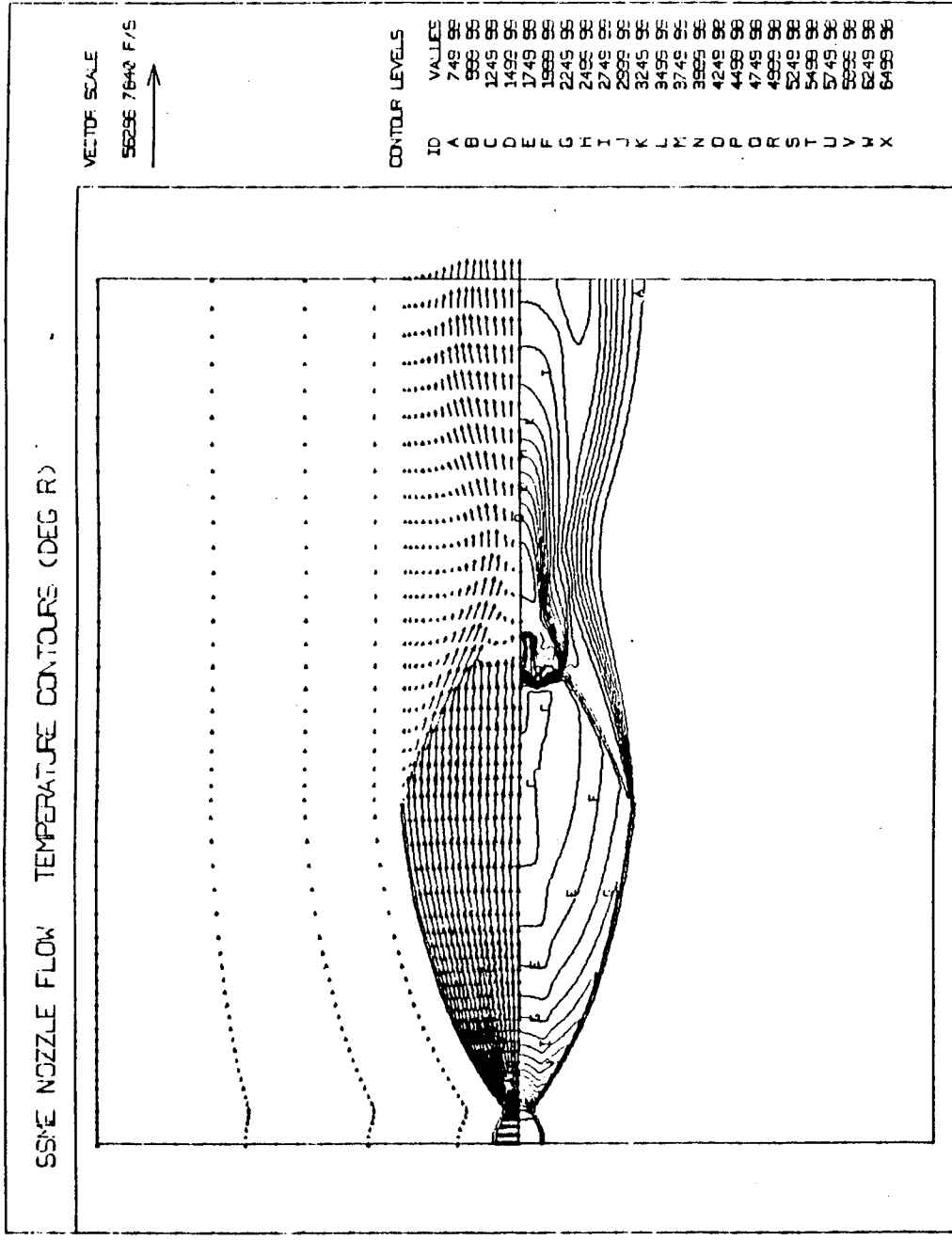is the best result obtained among all the schemes tested.
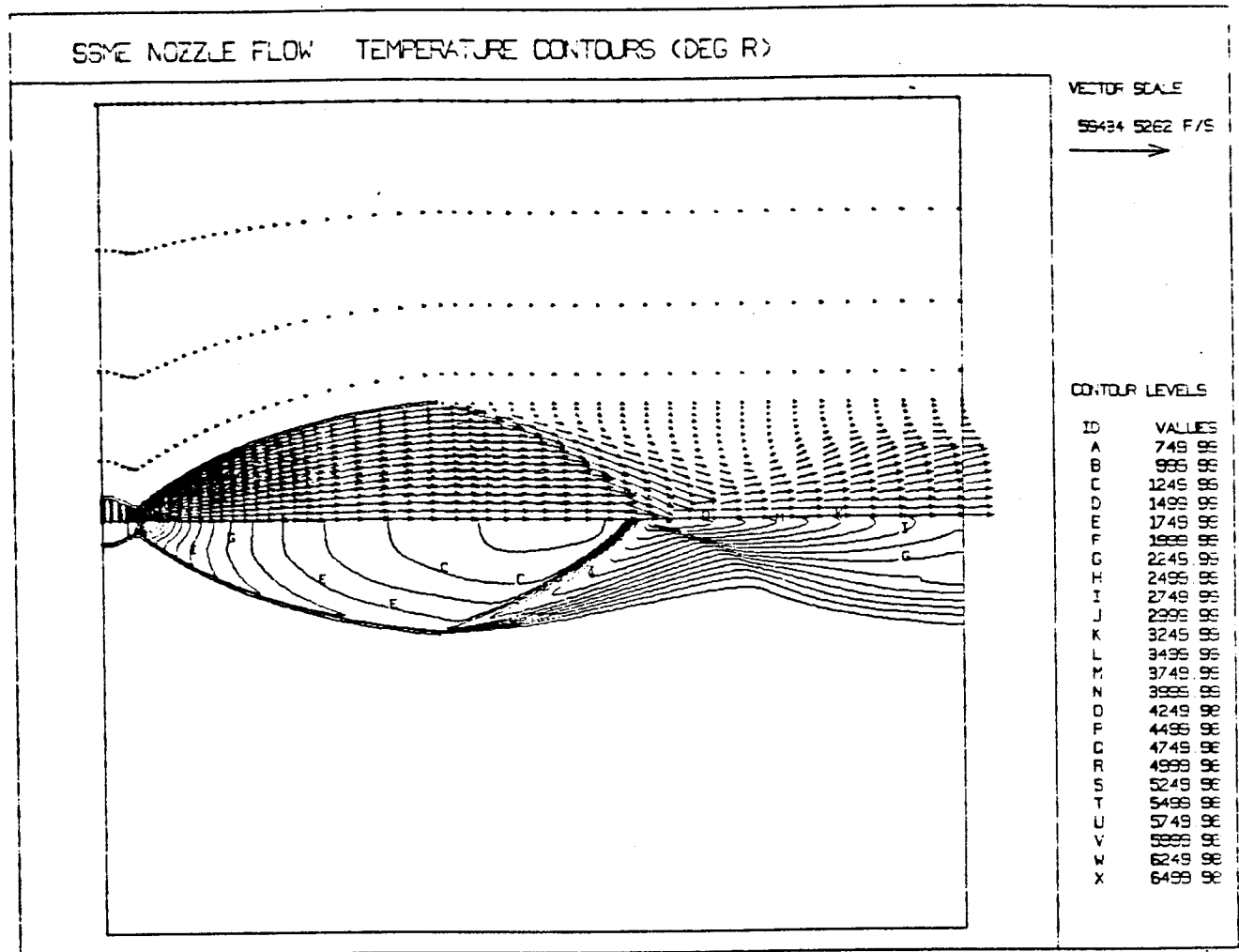
Fig. 28. SSME Plume Solution With Scheme (b)

75

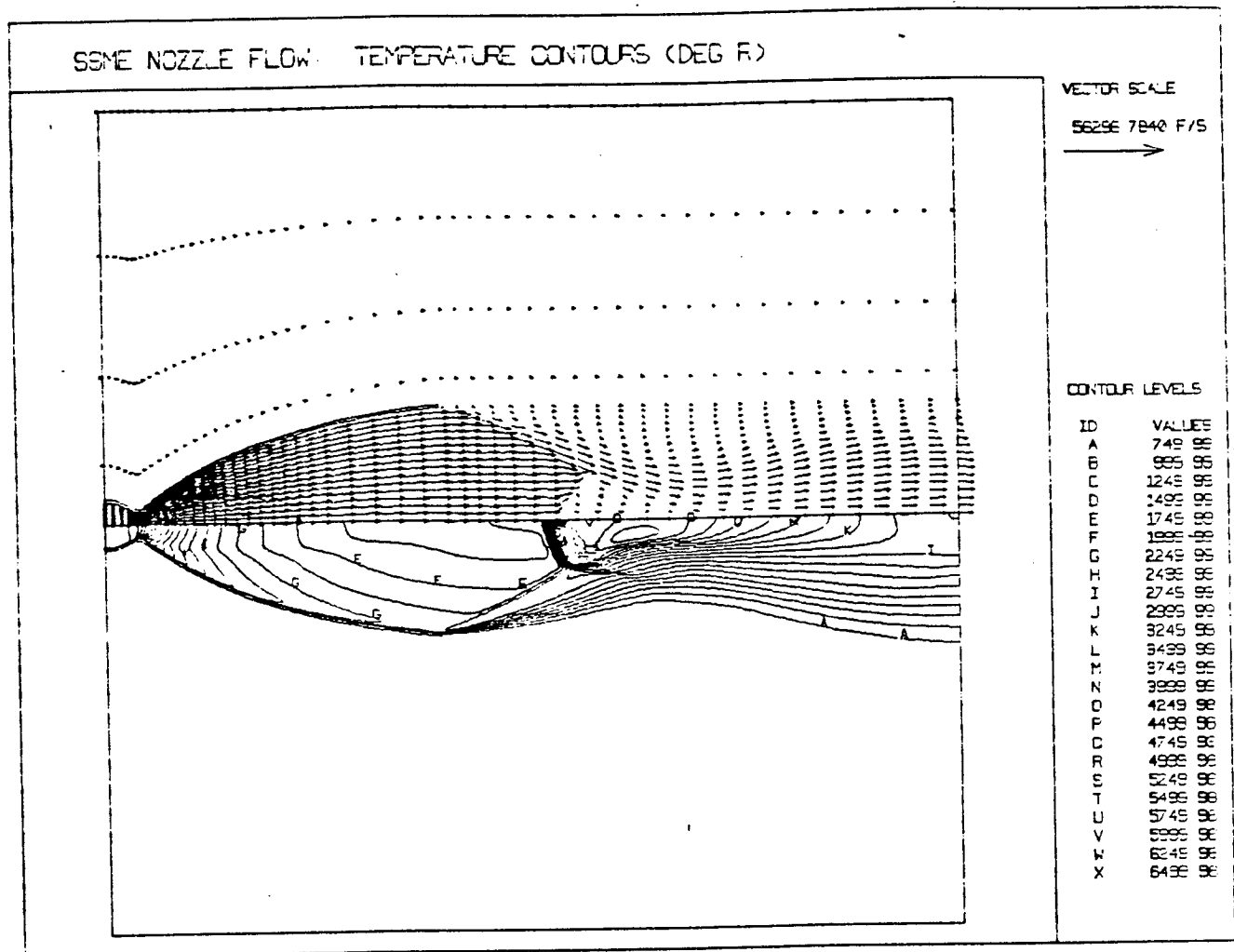Fig. 29. SSME Plume Solution With Scheme (d)

SSME NOZZLE FLOW   TEMPERATURE CONTOURS (DEG R)

VECTOR SCALE

5629E 7840 F/S

CONTOUR LEVELS

ID	VALUES
A	749.98
B	999.98
C	1249.99
D	1499.99
E	1749.88
F	1999.88
G	2249.99
H	2499.98
I	2749.99
J	2999.99
K	3249.98
L	3499.99
M	3749.98
N	3999.98
O	4249.98
P	4499.98
Q	4749.98
R	4999.98
S	5249.98
T	5499.98
U	5749.98
V	5999.98
W	6249.98
X	6499.98

Fig. 30.   SSME Plume Solution With Schemes (c) or (e)

However, the recirculating flow feature is still predicted by this method. The recirculating flow, which is induced by the fast spreading of the shear layer along the slip line, causes tilting of the Mach disc. This suggests that a more elaborate treatment of the turbulence near the triple point may eliminate the recirculating flow behind the Mach disc.

3.3.2 Solid Motor Flat Plate Plume Impingement

The most elementary plume property to be predicted is the centerline pressure decay. To match measured centerline pressure decay data, the FDNS extended k-ϵ turbulence model was modified in such a way that the predicted eddy viscosity was reduced as the local Mach number increased, i.e. as the density decreased. The cases run to establish this correlation were for a gas only approximation to a two-phase solid rocket motor plume, hence the results should be interpreted as qualitative only. The resulting impact pressure prediction and comparison to measurements on a plate at two axial stations are shown in Figs. 31a and 31b. The corresponding Mach number profiles are shown in Figs. 32a and 32b. The implication of this prediction is that a Mach number correction to the extended k-ϵ model is required to suppress turbulence at high Mach numbers. The source term for energy dissipation in the FDNS extended k-ϵ model is:

$$\rho\,(\epsilon/K)\;(C_1 P_r - C_2 \epsilon + C_3 P_r^2/\epsilon)$$

To apply this expression to plume impingement, C_3 must be replaced by:

$$C_3[1.0 + 0.08M^{0.25}]$$

78
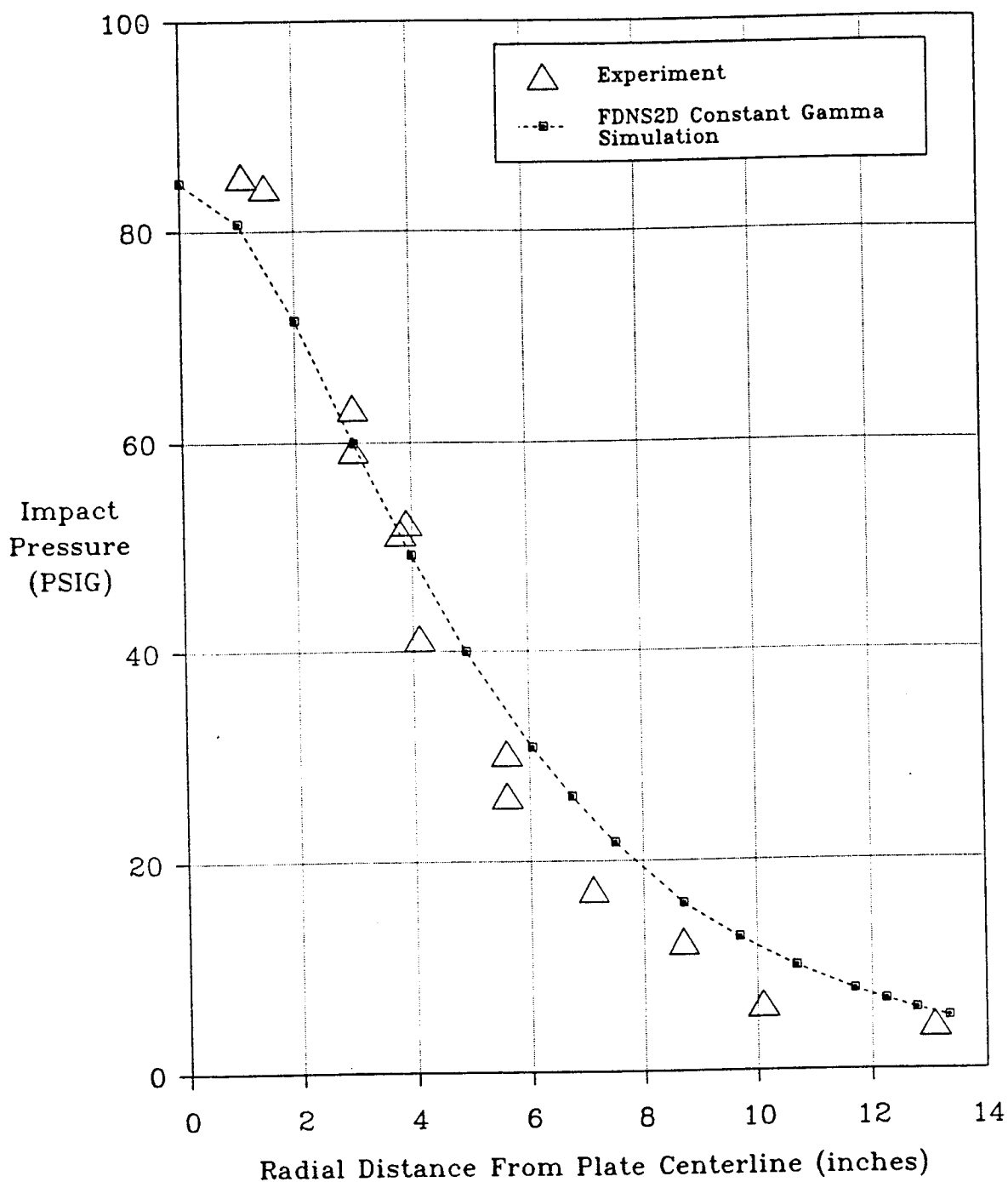
Fig. 31a. Comparison of Experimental and Calculated Impingement
Pressure Distribution on Flat Plate 12.2 feet From Exit
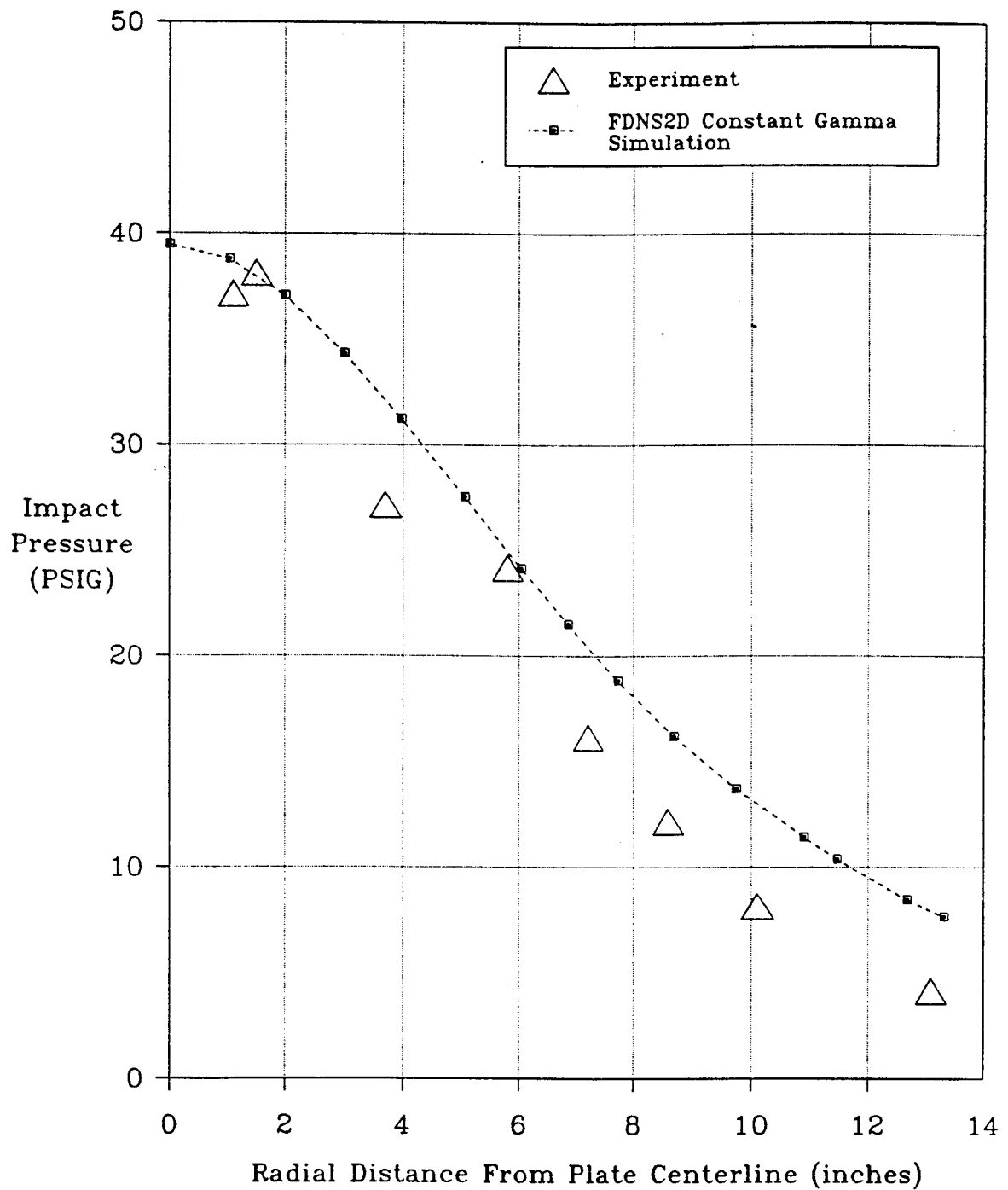Plane of Tomahawk Motor, FDNS2D Constant Gamma
Simulation

Fig. 31b. Comparison of Experimental and Calcualated Impingement
Pressure Distribution on Flat Plate 17.0 feet From Exit
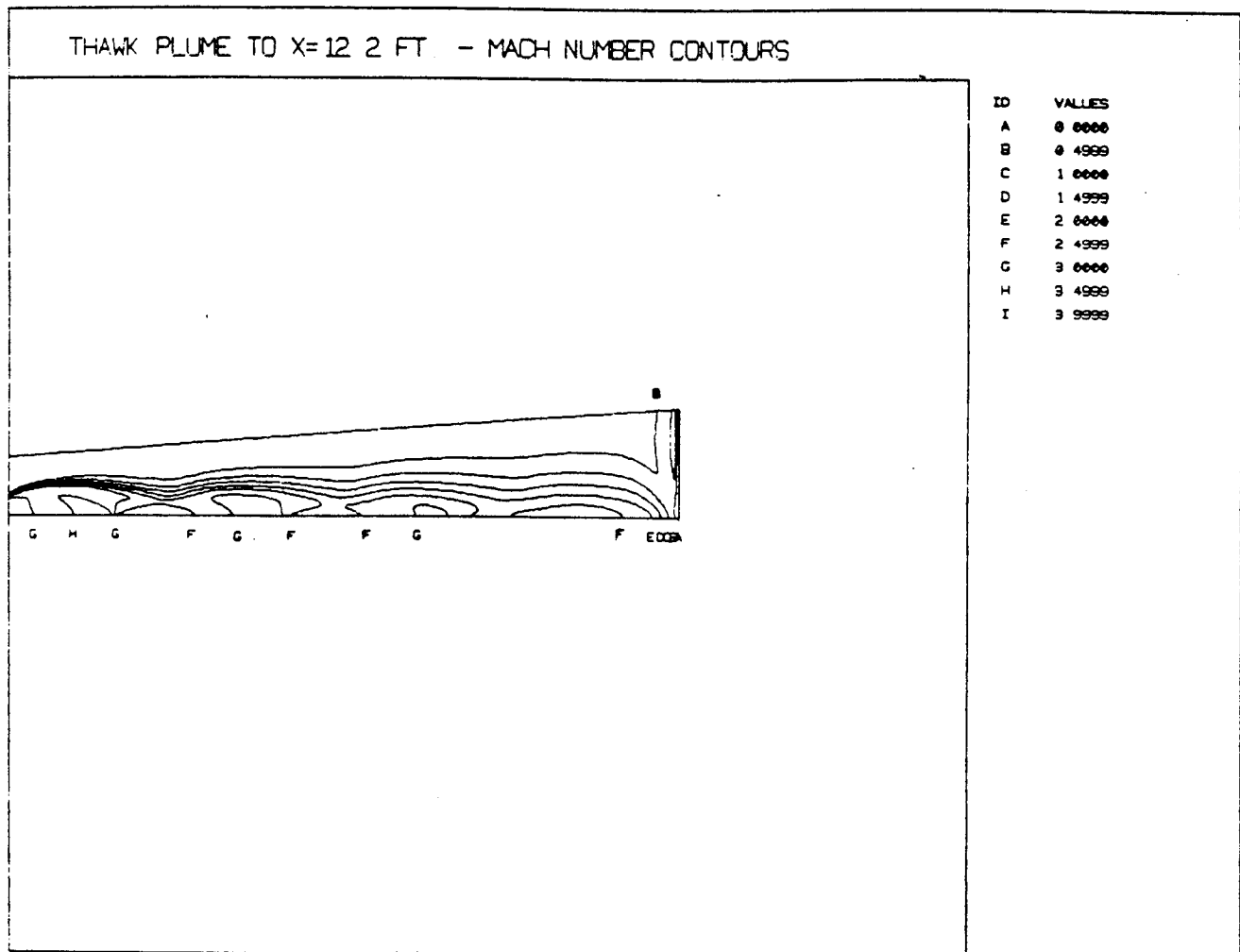Plane of Tomahawk Motor, FDNS2D Constant Gamma
Simulation

THAWK PLUME TO X=12 2 FT - MACH NUMBER CONTOURS

ID	VALUES
A	0 0000
B	0 4999
C	1 0000
D	1 4999
E	2 0000
F	2 4999
G	3 0000
H	3 4999
I	3 9999

Fig. 32a. Tomahawk Plume Impingement on a Plate 12.2 feet From
           Nozzle Exit, Calculated Mach Number Contours, Constant
           Gamma Simulation

THAWK PLUME TO X=17.0 FT. - MACH NUMBER CONTOURS

ID	VALUES
A	0.0000
B	0.4999
C	1.0000
D	1.4999
E	2.0000
F	2.4999
G	3.0000
H	3.4999
I	3.9999
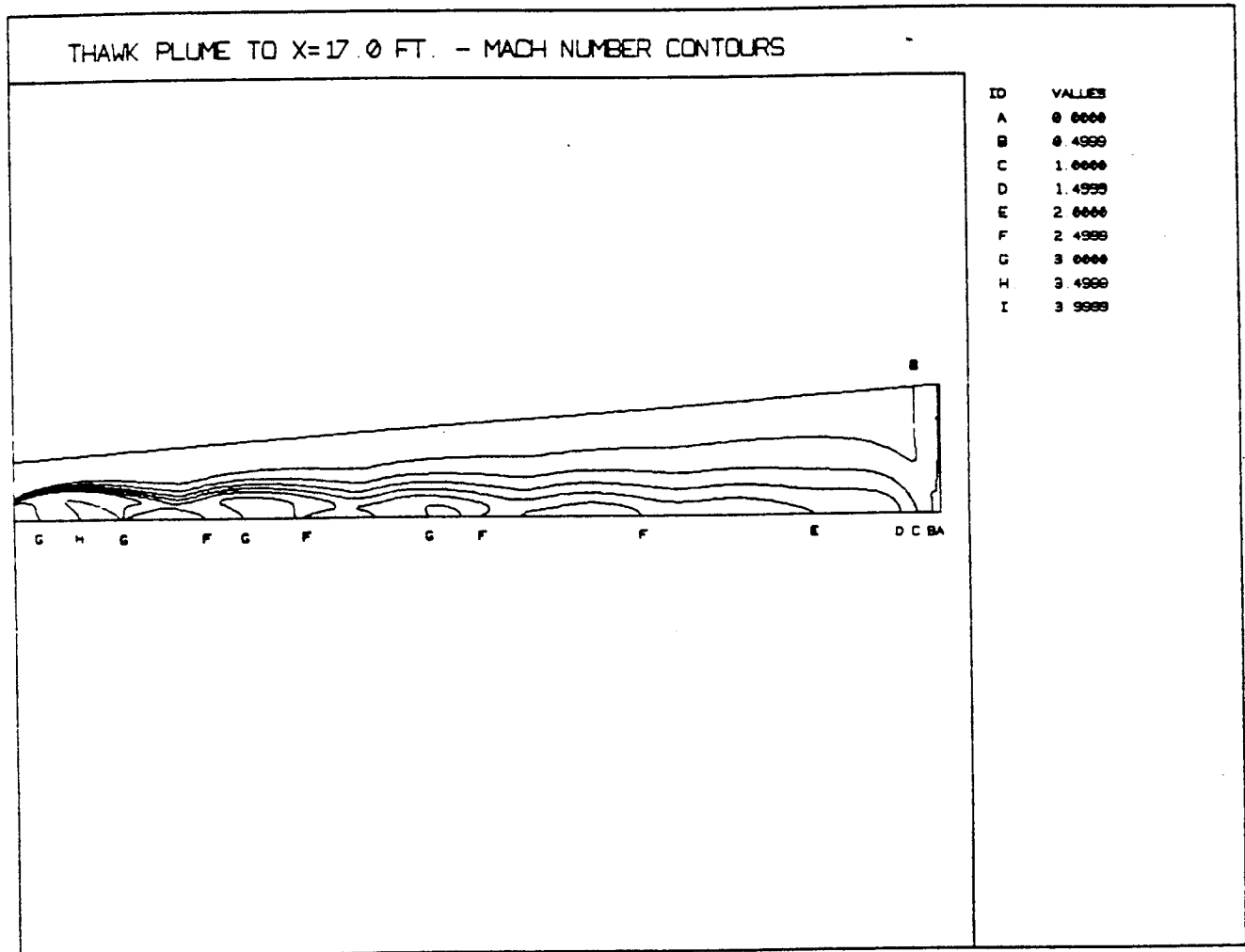
Fig. 32b. Tomahawk Plume Impingement on a Plate 17.0 feet From
Nozzle Exit, Calculated Mach Number Contours, Constant
Gamma Simulation

Such a model is needed not only to make accurate plume predictions, but it may have a strong influence on predicted Mach disc flows. Large viscous mixing effects and smaller artificial damping effects, severely compromise the prediction of complex shock structure. The artificial effects must be removed from the prediction and the real turbulence effects must be accurately predicted, not overpredicted. It has been previously shown that a similar treatment of turbulence was required to describe a dump combustor flow (Ref. 15) which exhibited a large density reduction associated with the combustion.

3.4 Blunt Body Flow Fields

3.4.1 Supersonic Axisymmetric Blunt Body Flows

Supersonic axisymmetric flow parallel to a spherical-cylinder configuration has been simulated for three Mach numbers for which test data are available (Ref. 22). The computational mesh is shown in Fig. 33 and consists of 81 by 41 points. FDNS2D solution convergence histories for the Mach 6 and 10 cases are shown in Fig. 34. Stagnation-line pressure and temperature plots are shown in Fig. 35 for the Mach 6 case. Pressure, temperature, and Mach number plots are shown in Figs. 36 and 37. Non-dimensional surface pressure distributions are shown in Fig. 38 and compared to the test data indicated by the open circles. Figs. 39 through 42 show similar predictions and data comparisons for the Mach 10 case. A stagnation line pressure plot and surface pressure distributions are shown in Fig. 43 for a Mach 20 case. These predictions are for a viscous flow using an extended k-ϵ turbulence model. The flow is adiabatic and the total temperature is conserved to within 1% throughout the flow field.
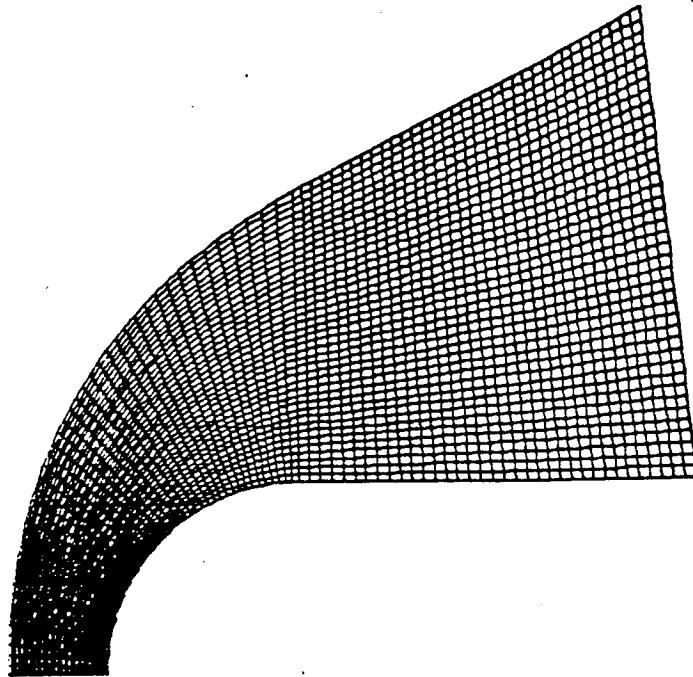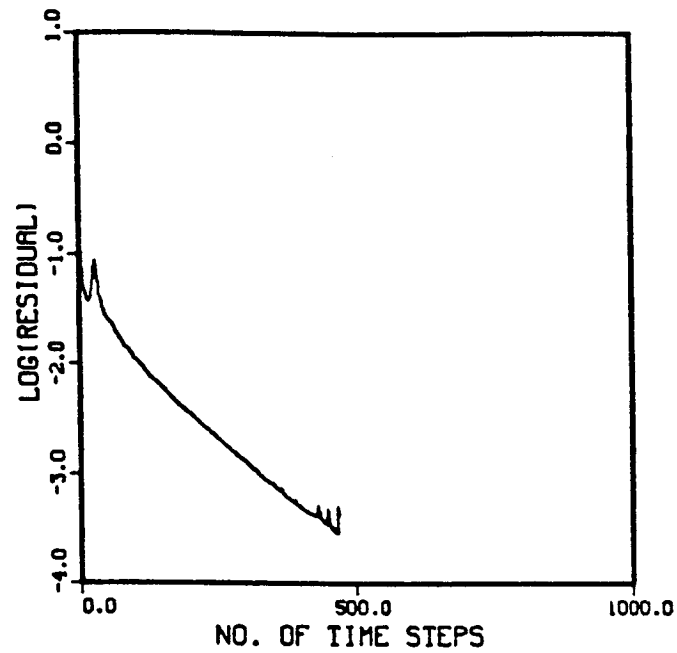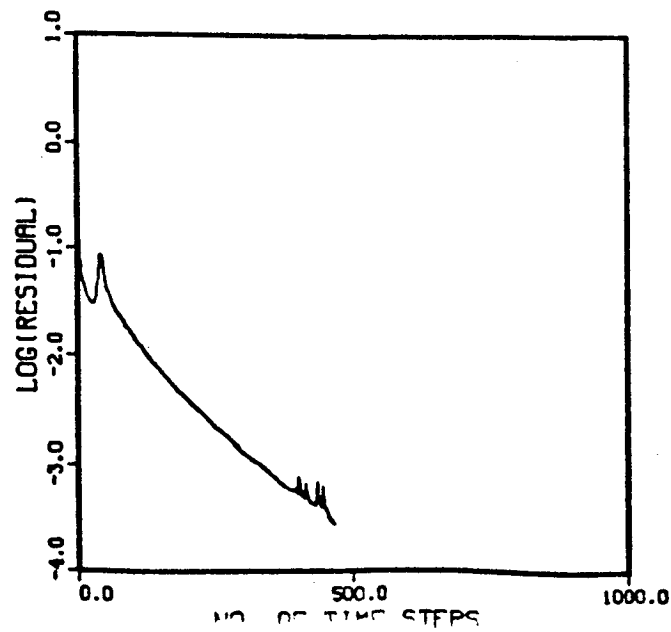
Fig. 33. Computational Mesh for Spherical-Cylinder Blunt Body
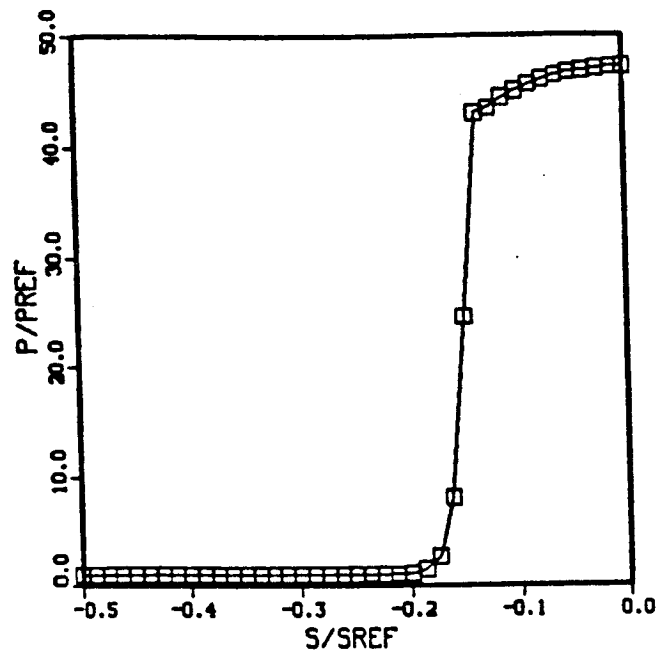Configuration (81 x 41)

CONVERGENCE HISTORY $M_{oo} = 6.05$

CONVERGENCE HISTORY $M_{oo} = 10.20$

Fig. 34. Convergence History for M_{oo} = 6 and 10 cases
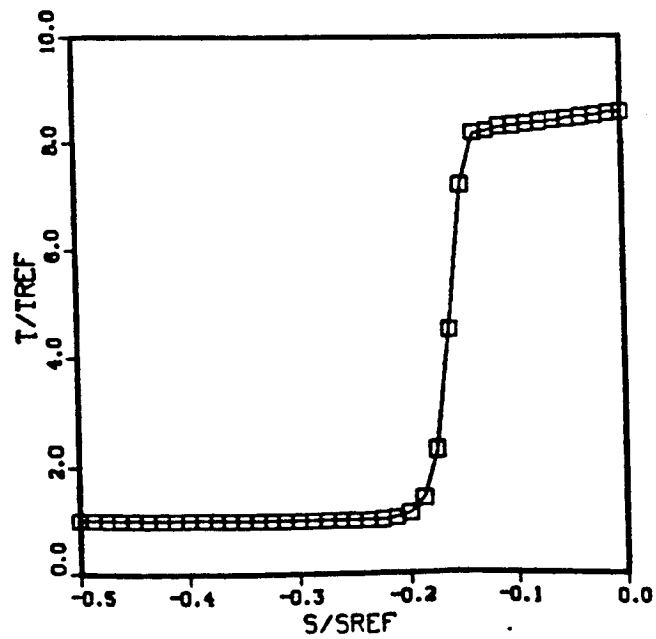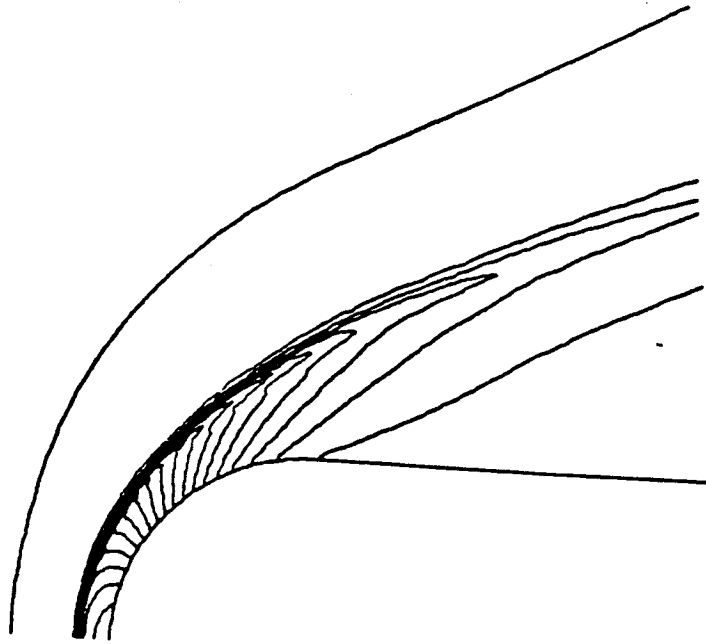
85

PRESSURE

TEMPERATURE

Fig. 35. Stagnation Line Axial Pressure and Temperature Profiles
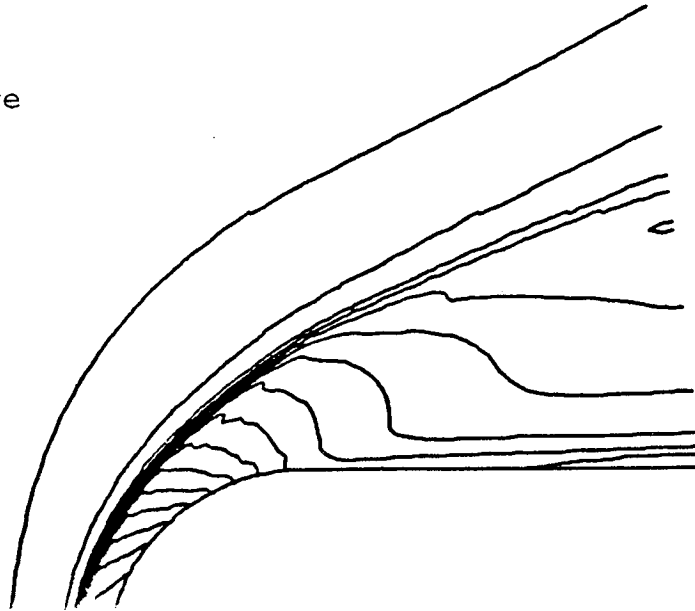for Blunt Body at $M_{oo} = 6.05$

Pressure

Temperature

Fig. 36. Pressure and Temperature Contours for Blunt Body at
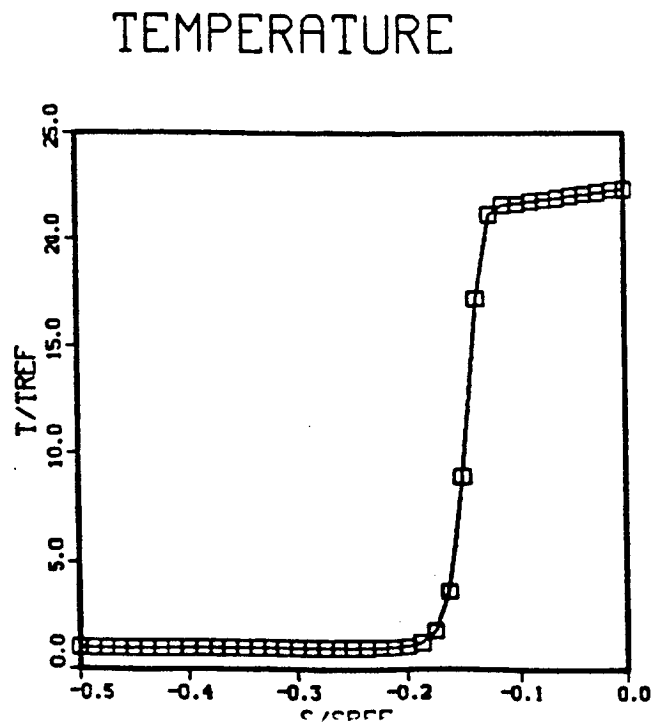$M_{oo} = 6.05$

Mach No.

Fig. 37. Mach Number Contours for Blunt Body at $M_{\infty} = 6.05$
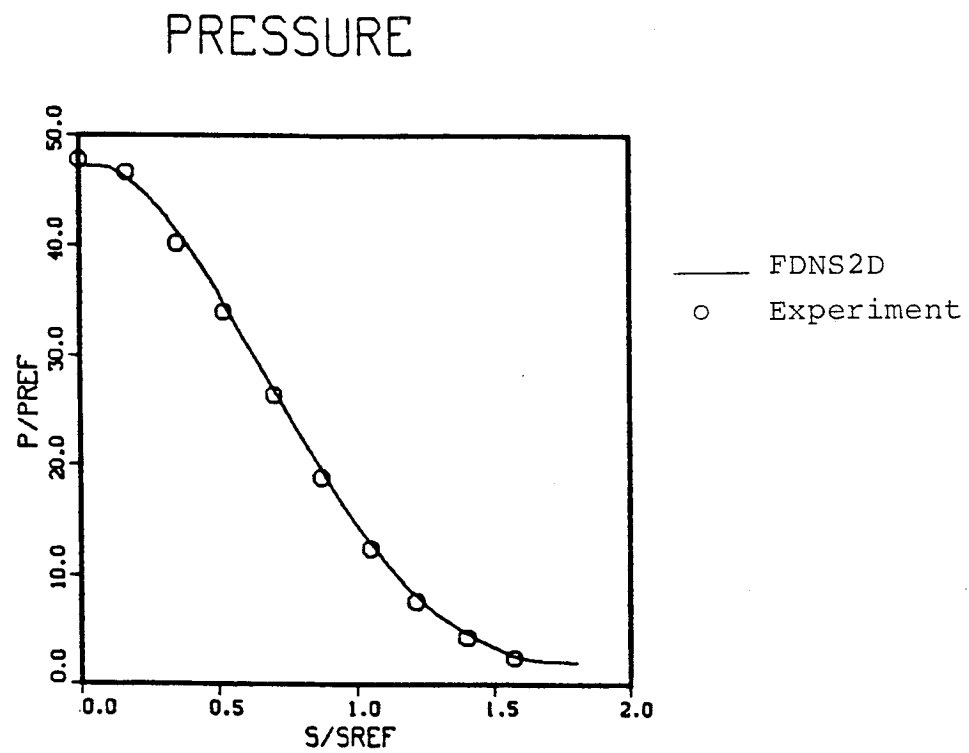
PRESSURE

Fig. 38.   Surface Pressure Distribution for Blunt Body at
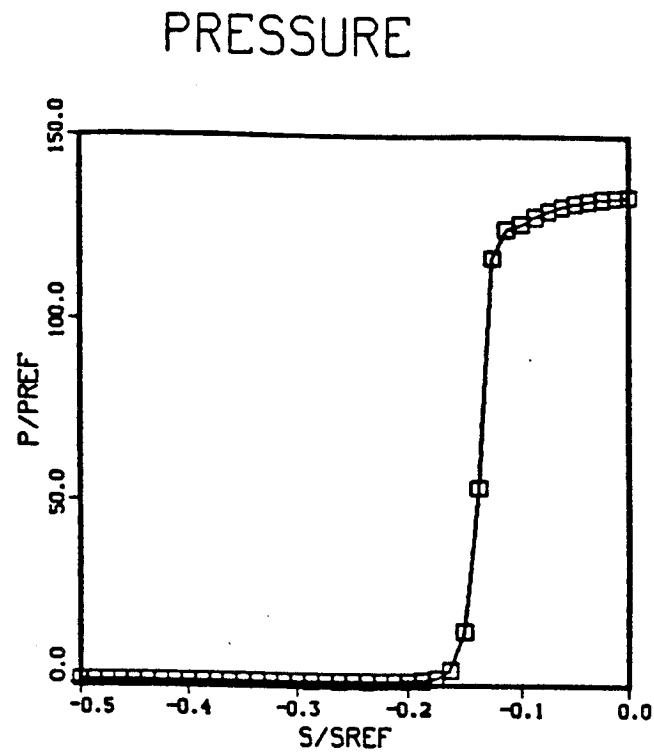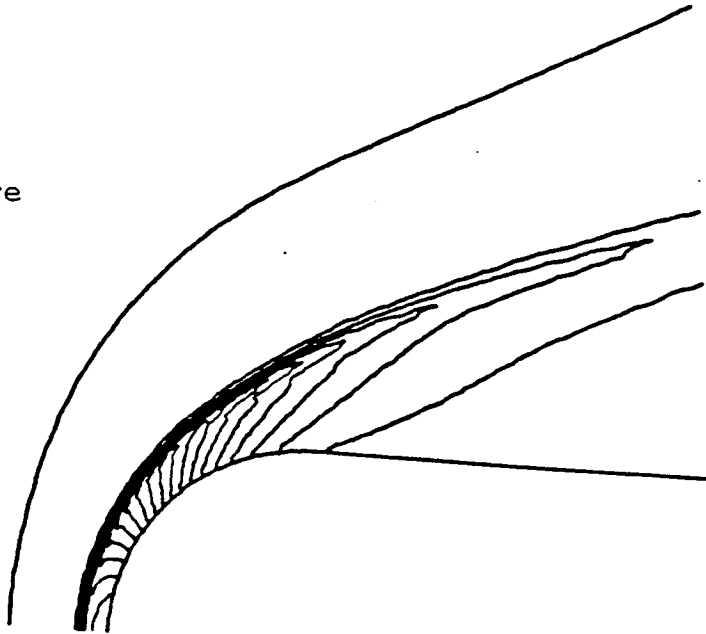$M_{oo} = 6.05$

PRESSURE

TEMPERATURE

Fig. 39.   Stagnation Line Axial Pressure and Temperature
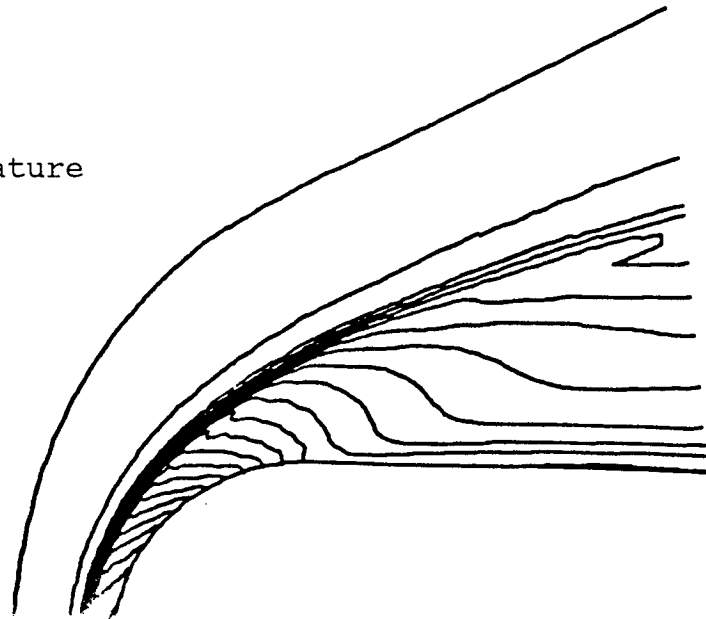Distributions for Blunt Body at M_{oo} = 10.20

90

Pressure

Temperature

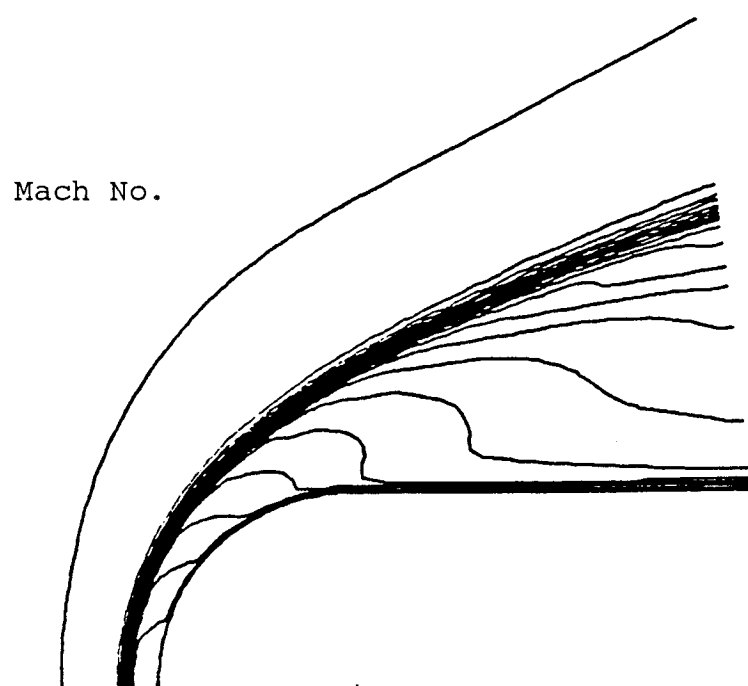Fig. 40. Pressure and Temperature Contours for Blunt Body at
M_{oo} = 10.20

Mach No.

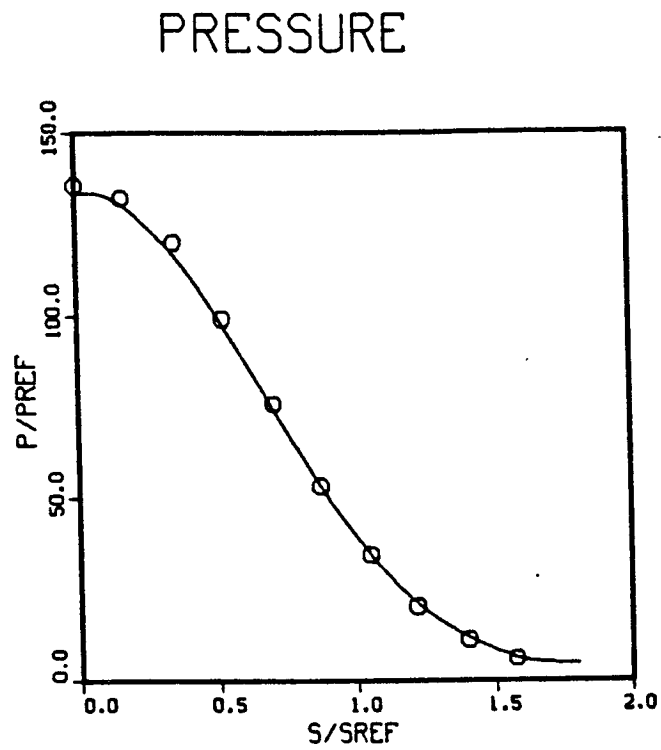Fig. 41. Mach Number Contours for Blunt Body at M_{oo} = 10.20

C-2.

PRESSURE

Fig. 42.   Surface Pressure for Blunt Body at $M_{\infty} = 10.20$

PRESSURE

On Surface
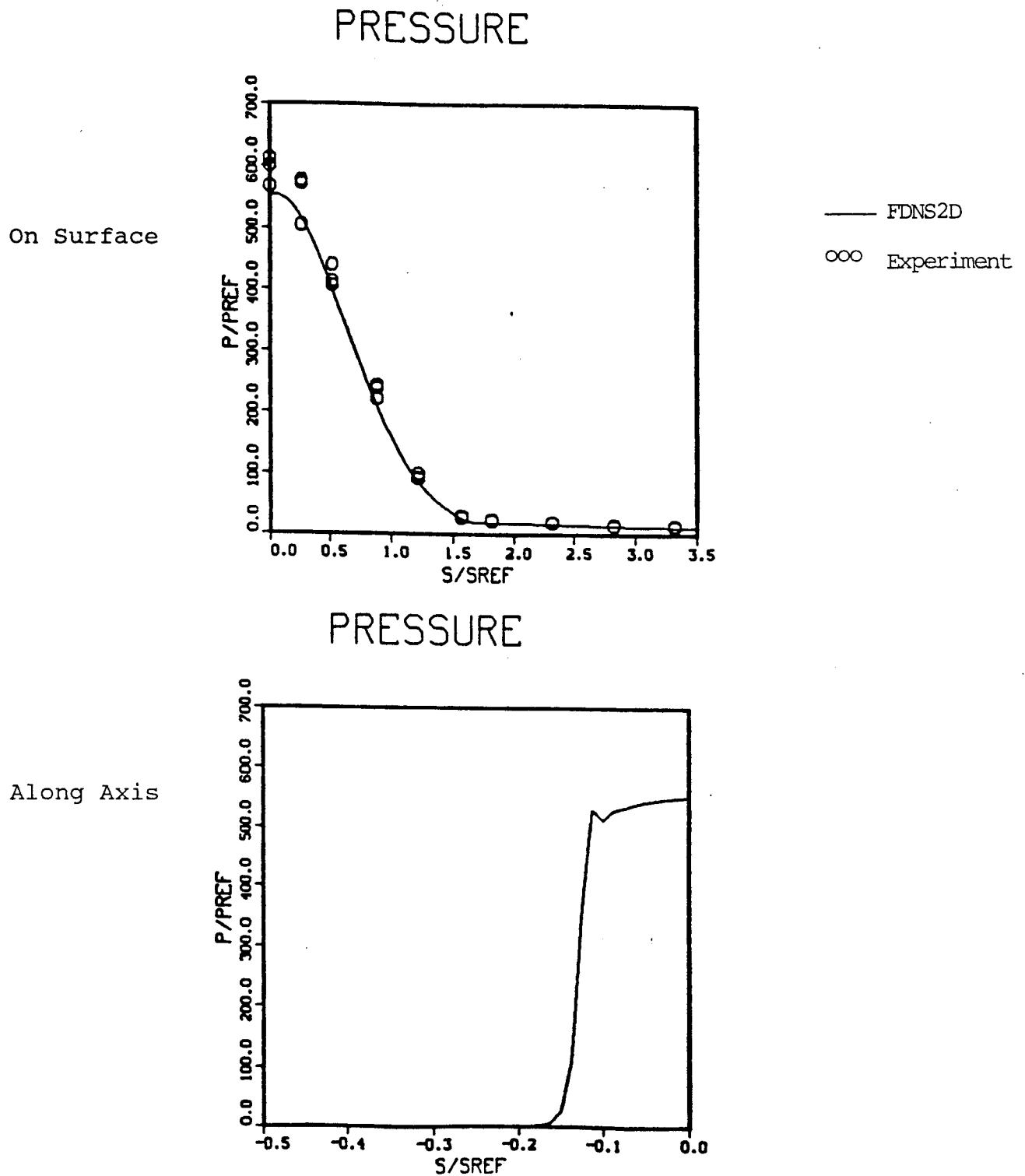

——— FDNS2D

OOO Experiment

PRESSURE

Along Axis

Fig. 43. Surface Pressure and Stagnation Line Pressure
Distributions for Blunt Body at M_{oo} = 20.8

94

Total pressure is conserved every where except near the wall where viscous effects cause it to be reduced. These predictions are in excellent agreement with the test data.

Results of simulations of axisymmetric supersonic flow over a blunt body for free stream Mach numbers of 6.05, 10.20 and 20.8 are shown in Fig. 35 through 43. To further benchmark this case, an inviscid flow and a turbulent flow with a free stream Mach number 8.02 were computed. Effects of the turbulence model on the surface pressure and temperature distributions were investigated. A grid size of 81 x 41 and time step size of 0.01 were used. For the inviscid case, total temperature loss of the solution can be quantified. To run the FDNS code with zero viscosity, a slip-wall boundary condition was implemented. Convergence history for the inviscid case is shown in Fig. 44. For turbulent flow case, only about one half of the time steps were needed to get the same convergence. Figure 45 shows the predicted pressure, temperature and Mach number contours for the turbulent flow case. Figure 46 shows the surface pressure and temperature distributions for the same case while results for the inviscid case are given in Fig. 47. Figures 46a and 47a show good agreement between the predictions and the measured data (Ref. 28). Figures 46 and 47 show that although both cases give almost identical surface pressure distributions, the turbulent flow produces higher stagnation temperature than the inviscid case. This is due to the viscous heat generation term in the energy equation. Total temperature distributions on the body surface and along the axis are shown in Fig. 48. Total temperature loss on the wall surface is apparent near the shoulder of the cylinder (i.e. $S/X_{ref} = 1.57$). A large total temperature dip (16 percent of the free stream total) is also predicted across the shock. This is a common feature of most
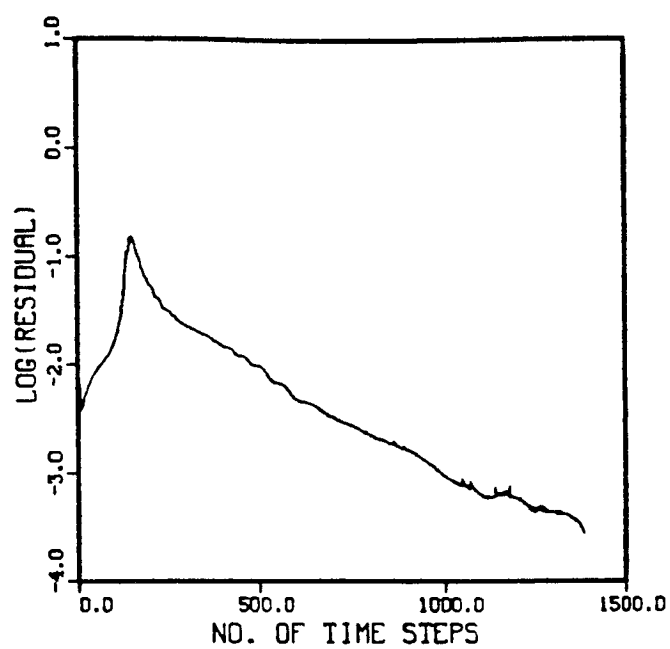
CONVERGENCE HISTORY
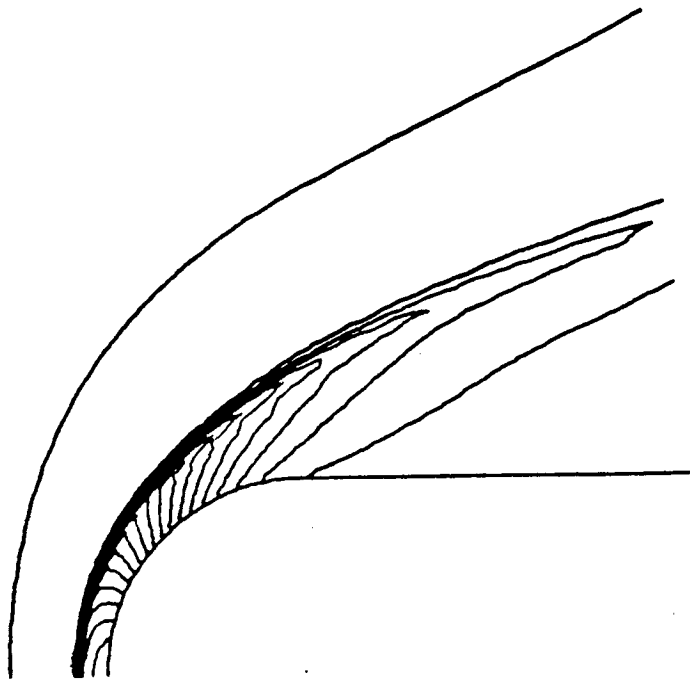

Fig. 44. Convergence history for Inviscid Flow over a Spherical Cylinder at $M_{oo} = 8.02$
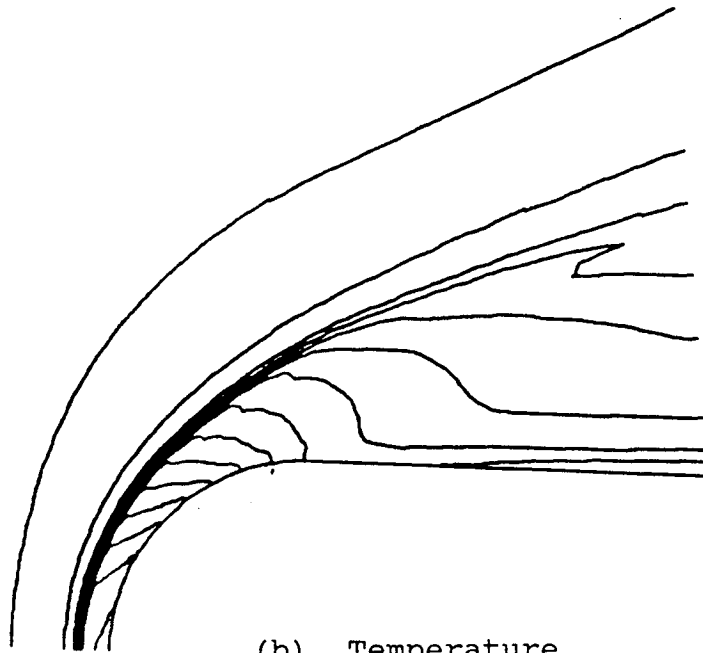
(a) Pressure

(b)   Temperature

Fig. 45.   Turbulent Flowfield over a Spherical Cylinder at
$M_{oo} = 8.02$

97

(c)   Mach Number

Fig. 45.   Turbulent Flowfield over a Spherical Cylinder at
M_{oo} = 8.02

PRESSURE

(a)
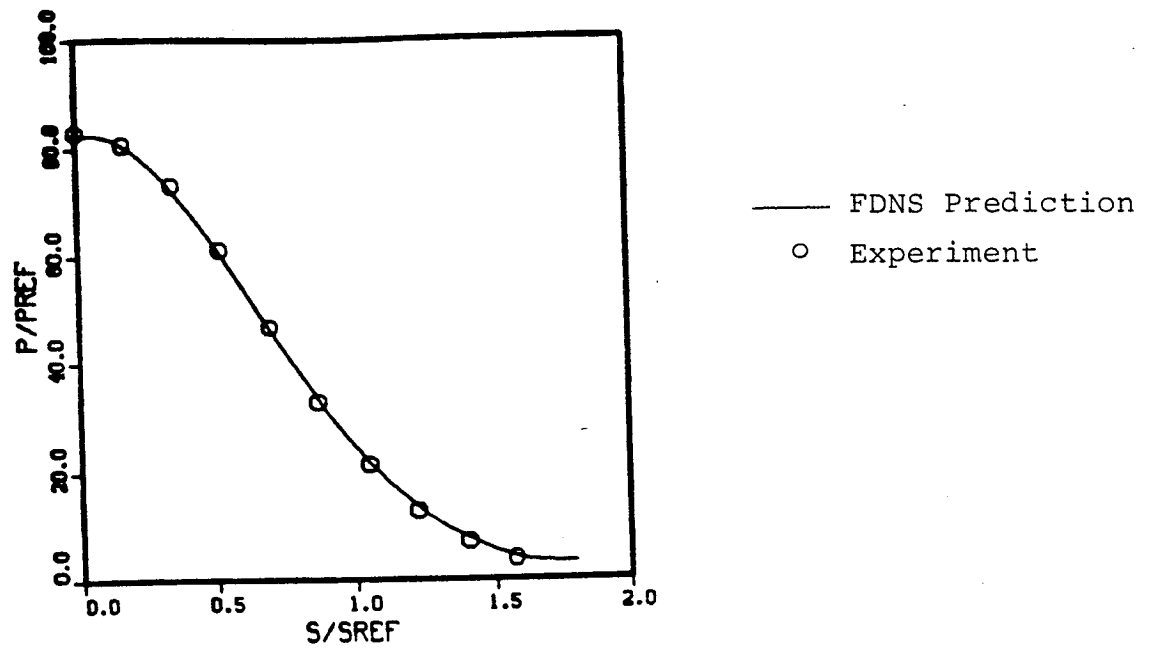
TEMPERATURE
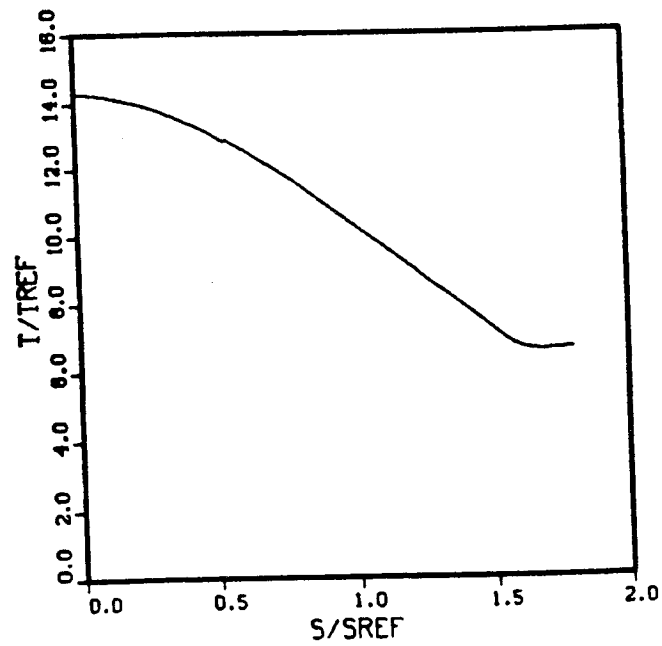
(b)

Fig. 46. Turbulent Flow over a Spherical Cylinder at M_{oo} = 8.02, Surface Pressure and Temperature Distributions

PRESSURE

(a)

TEMPERATURE

(b)

Fig. 47. Inviscid Flow over a Spherical Cylinder at $M_{oo} = 8.02$, Surface Pressure and Temperature Distributions

TOTAL TEMPERATURE

(a)   Wall Surface

TOTAL TEMPERATURE

(b)   Axial Distribution

Fig. 48.   Total Temperature Distributions for Supersonic Inviscid
Flow over a Spherical Cylinder Blunt Body at $M_{oo} = 8.02$

numerical schemes. The total temperature dip is sharp near the shock but the total temperature does recover to free-stream values downstream of the shock. Other t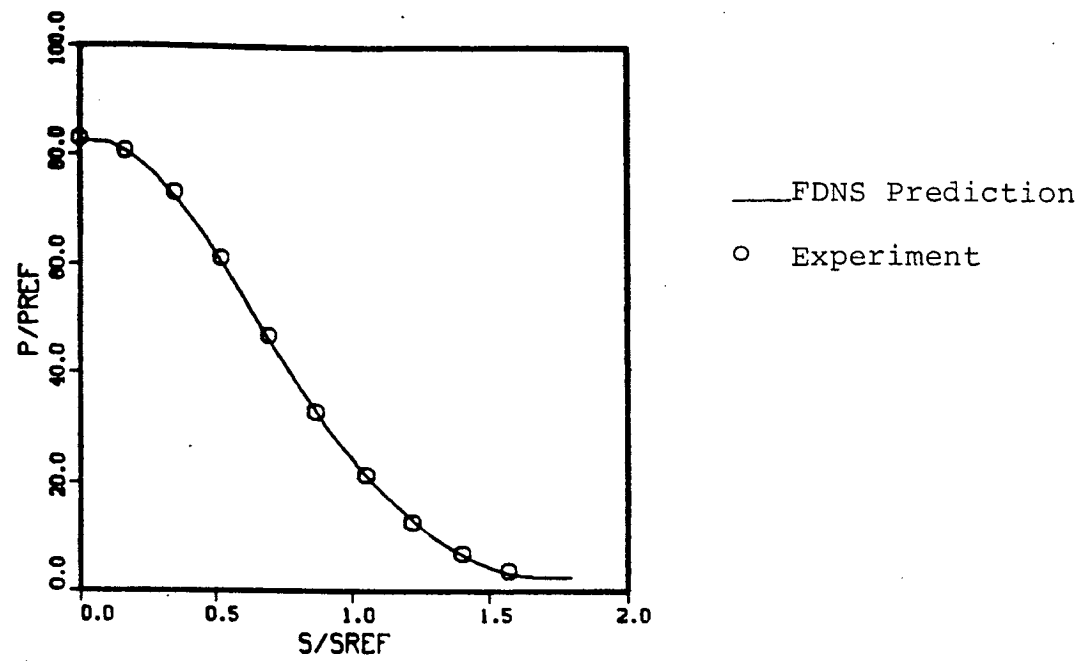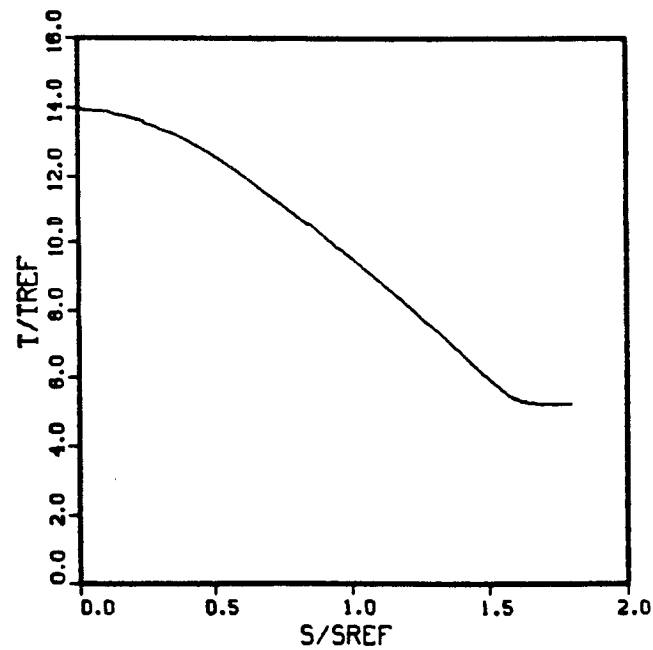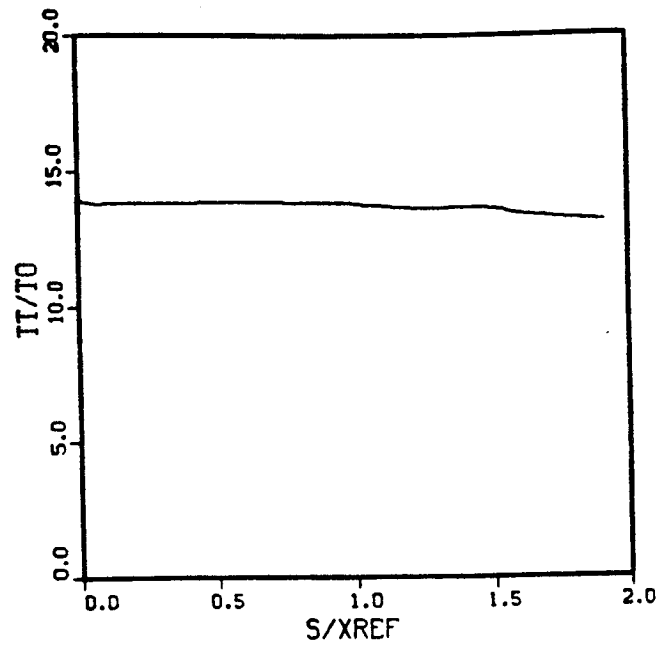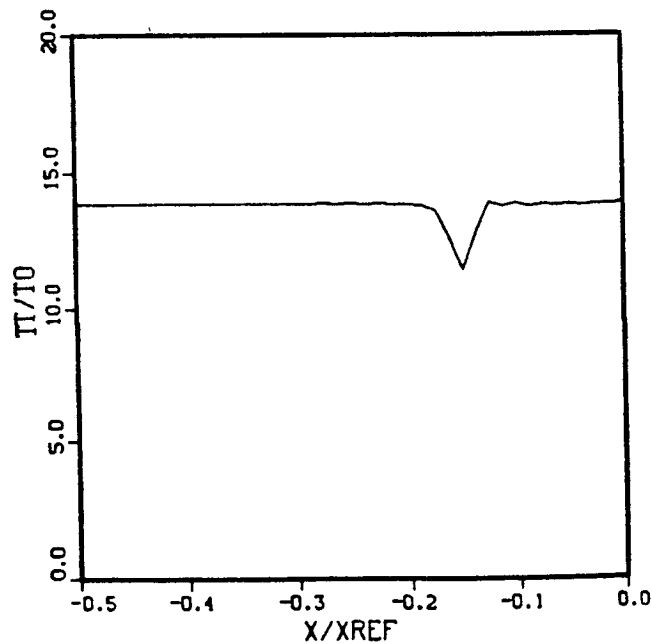han these features the FDNS code conserves the total temperature reasonably well. Therefore, the thermal analysis of the body is not compromised by this computational feature of the solution.

Although it was not investigated as a part of this study, flow over a backstep was previously investigated with FDNS (Ref. 18). This investigation established that the extension to the k-ϵ model was necessary to predict the correct reattachment length. Both the experiments which were simulated and the predictions indicated an unsteadiness in the flowfield downstream of the reattachment point. Quantitative evaluation of this unsteadiness was not attempted.

3.4.2 Supersonic Three-Dimensional Blunt Body Flows

a. 3-D Supersonic Spherical-Cylinder Blunt Body Flow

This problem represents an extension of the 2-D axisymmetric test case described in Section 3.4.1 to the three dimensional domain. The same free stream Mach number of 8.02 was imposed. A grid size of 41 x 21 x 31 was used, which is very coarse compared to the grid used in the 2-D case. A time step size of 0.01 was also assigned. The flow is assumed to be turbulent with an adabatic wall temperature boundary condition. The standard two-equation turbulence model with the wall function approach was employed. With this approach, there is no need to resolve the boundary layer below the viscous sublayer. This is a plausible approach for complex 3-D flow problems. A converged solution was obtained within 600 time steps (see Fig. 49). This calculation
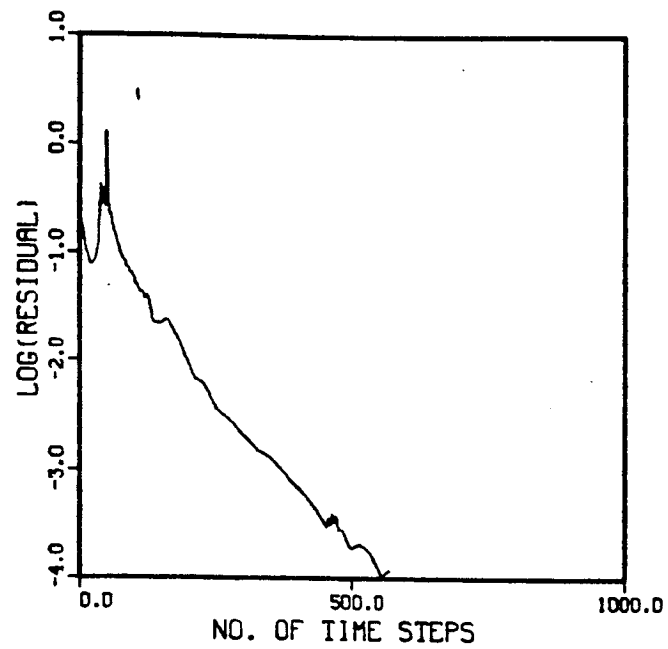
CONVERGENCE HISTORY

Fig. 49.   Convergence History for the 3-D Blunt Body Case at
            $M_{oo} = 8.02$

103

took 4600 sec of CPU time on the Cray-XMP supercomputer. Figure 50 illustrates the side-view and front-view of the predicted pressure contours. Again, about 3 to 4 grid points (in the direction normal to the shock) are needed to resolve the shock wave. It can be seen from Fig. 50b that an axisymmetric shock wave is predicted as expected. Figure 51a gives a comparison between the FDNS3D prediction and the measured data from Ref. 22. The predicted 3-D pressure distribution is not as smooth as the 2-D case, Fig. 47a. This is due to the coarse grid used in the longitudinal direction (only 21 grid points). However, even with this coarse grid, good agreement for the surface pressure distribution is shown in Fig. 51a. For the surface temperature distribution, Fig. 51b, the 3-D case gives almost identical results as the 2-D calculations shown in Figs. 46b and 47b.

The following problem represents a counterpart of the above test case to study surface heat transfer characteristics. The same free stream Mach number of 8.02 is imposed. A grid size of 38 x 45 x 41 is used (see Fig. 52), which is coarse compared to the grids used in the 2-D spherical-cylinder simulations reported previously. The grid wraps around 360 degrees in I-direction with a cyclic boundary condition imposed at I = 1 and I = Imax. A singularity line boundary condition is also applied along the stagnation line. A time step size of 0.01 was used. The flow is assumed to be laminar with Re = 0.23E+06 per in. A cylinder diameter of 5.8 in. was used in the experiment (Ref. 22). The viscosity law for blunt body flows described in Section 3.1 (based on Sutherland's formula) is employed in the simulation. A steady-state solution was obtained in 2000 time steps which is about 3 times greater than required for the turbulent flow case reported previously. This is due to the slow convergence near the wall boundary where very fine grids are used to resolve the
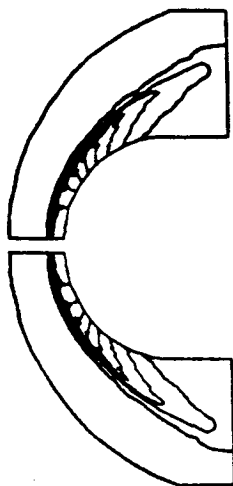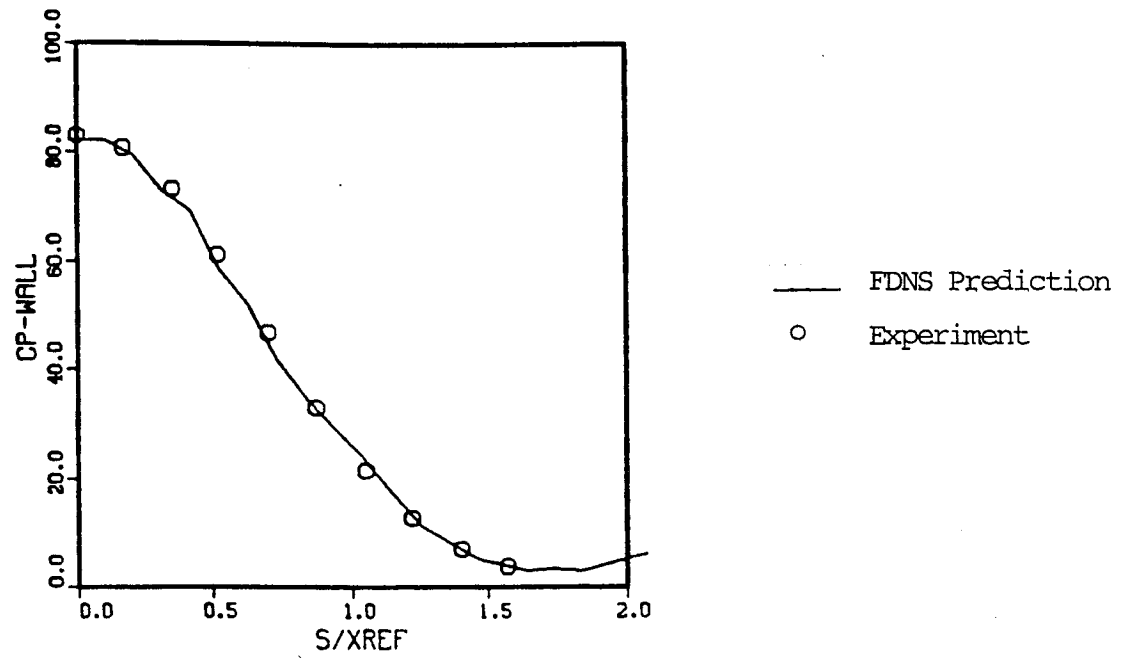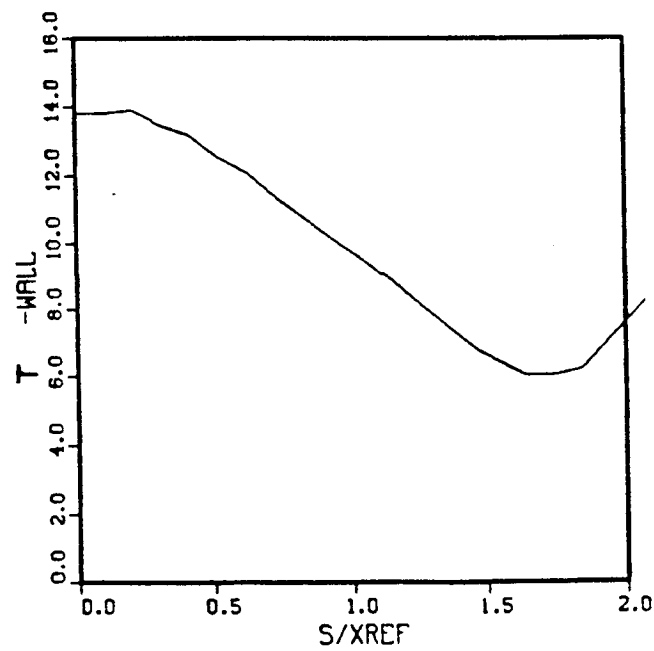
(a)   Side-View
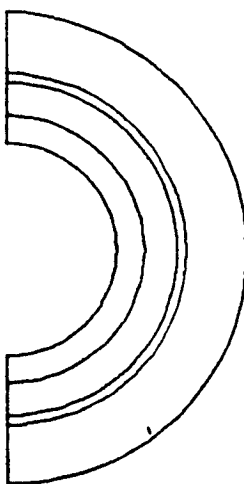
(b)   Front-View

Fig. 50.   Pressure Contours Around the 3-D Blunt Body at
$M_{oo} = 8.02$

105

(a)

(b)

Fig. 51. Surface Pressure and Temperature Distributions for the
3-D Blunt Body at M_{oo} = 8.02
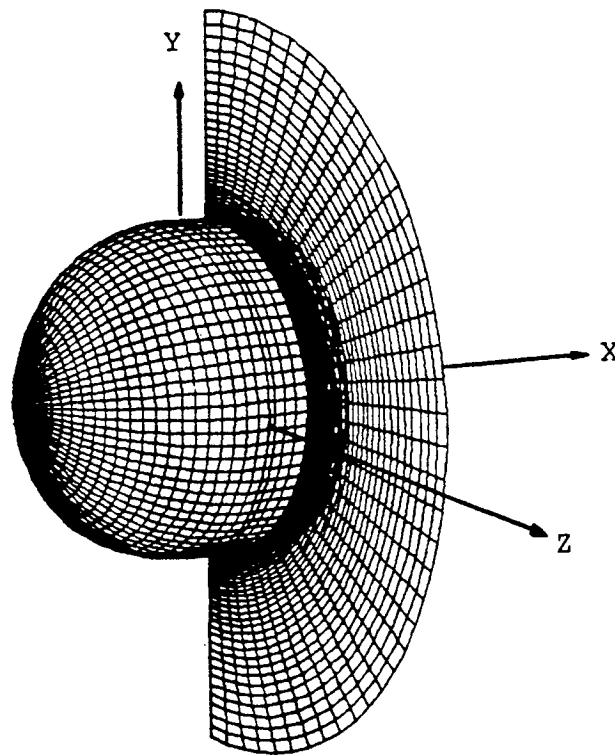
Fig. 52.   Mesh System for a 3-D Spherical-Cylinder Blunt Body

boundary layer. Figure 53 illustrates the side-view of the predicted pressure and temperature contours and shows that the solutions are symmetric as expected. Figure 54 gives comparisons of surface pressure and Stanton number distributions between the present prediction and the measured data from (Ref. 22). The predicted pressure distributions show good agreement with the measured data. For the Stanton number comparisons, only the normalized experimental distributions are used with the stagnation Stanton number estimated from the Fay-Riddell correlation (i.e. $St_s = 0.0078$). The measured stagnation Stanton number was reported to be 0.063 which is about 8 times higher than the Fay-Riddell estimate. With this modification to the experimental data, Fig. 54b shows reasonable correlations between the data and the FDNS3D predictions. Unlike the pressure predictions, the predicted Stanton number distributions are not smooth. This may be due to the coarse grid used in the longitudinal direction. However, even with this coarse grid, the FDNS3D predictions are generally in good agreement with the measured data.

b. 3-D Supersonic Circular-Cylinder Blunt Body Flows

Results of 3-D supersonic flow simulations over a spherical-cylinder blunt body for free stream Mach numbers of 6.05, 8.02, 10.20 and 20.8 are described above. Turbulent and inviscid flow cases have shown good results for surface pressure predictions. To further test these cases for heat transfer predictions, an experimental case of Mach 8 flow past a 3 in. diameter circular cylinder (Ref. 21) with a high Reynolds number (Re = 1.44E+06 per ft.) and a laminar flow assumption has been computed. In order to check the general performance of the 3-D version of the FDNS code (FNDS3D), this flow problem is simulated in three

(a)   Pressure
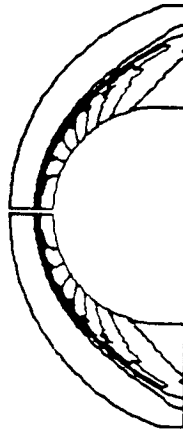
(b)   Temperature

Fig. 53. 3-D Sperical-Cylinder Blunt Body Flowfield at M_{oo} = 8.02
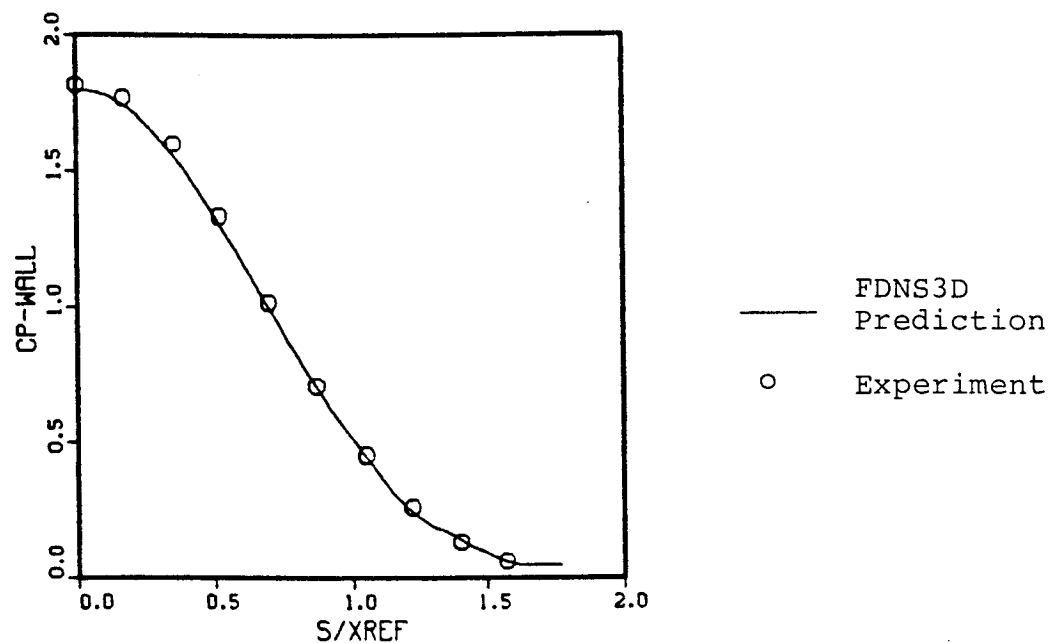
(a)   Surface Pressure Coefficient, CP-WALL
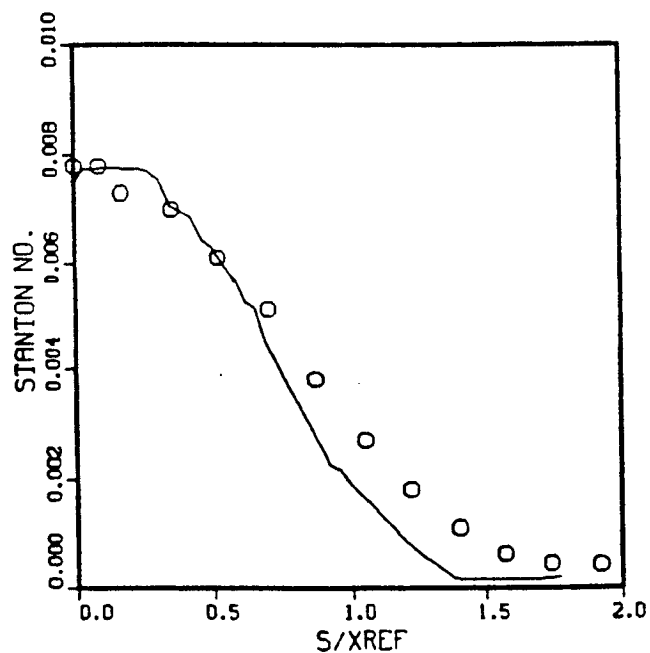
(b)   Heat Transfer Coefficient, Stanton No.

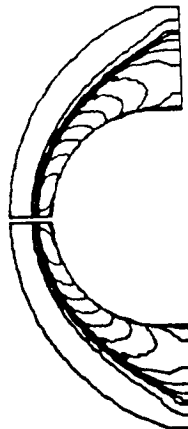Fig. 54.   Comparisons of Surface Pressure and Heat Transfer
Coefficients for a 3-D Spherical-Cylinder Blunt Body at
$M_{\infty} = 8.02$

dimensions. A grid size of 21 x 45 x 41 (with more grid points clustered near the wall) and a time step size of 0.01 was used. Symmetric boundary conditions along the symmetry plane and the transverse boundaries are imposed so that a two-dimensional flowfield solution can also be obtained. The blunt body flow viscosity law described in Section 3.1 is employed in the computation. Around 1500 time steps are required for the solution to reach steady state. Figure 55 shows the predicted pressure and temperature fields. The oscillations in pressure and temperature contours downstream of the shock are due to small second-order damping used in the code. This feature, however, does not affect the solution on the blunt body surface. The predicted surface pressure and heat transfer coefficient (Stanton number) distributions are compared with measured data (Ref. 21) in Figs. 56a and 56b respectively. Good correlations between the FDNS3D predictions and the test data are shown in Fig. 56. It is worth mentioning that the stagnation-point heat transfer coefficient estimated from the Fay and Riddell formula given above also correlates well with the experimental data and the FDNS3D prediction.

3.4.3 Supersonic Three-Dimensional AFE Blunt Body Flow

a. AFE Flowfield Heat Transfer Characteristics

For the AFE blunt body heat transfer analyses presented below, the Stanton number distributions on the windward surface of the blunt body were computed by using the solutions of the temperature field. The fluid viscosity was calculated based on the Sutherland's law. This implies that the thermal conductivity follows the same law since the specific heat and the Prandtl number were assumed to be constant. The Prandtl number was assumed to be 0.72 which is valid for air under the test

111

(a)   Pressure Contours

(b)   Temperature Contours

Fig. 55.   Circular-Cylinder 3-D Blunt Body Flow at $M_{oo} = 8.02$

112

(a) Surface Pressure Coefficient, CP-WALL
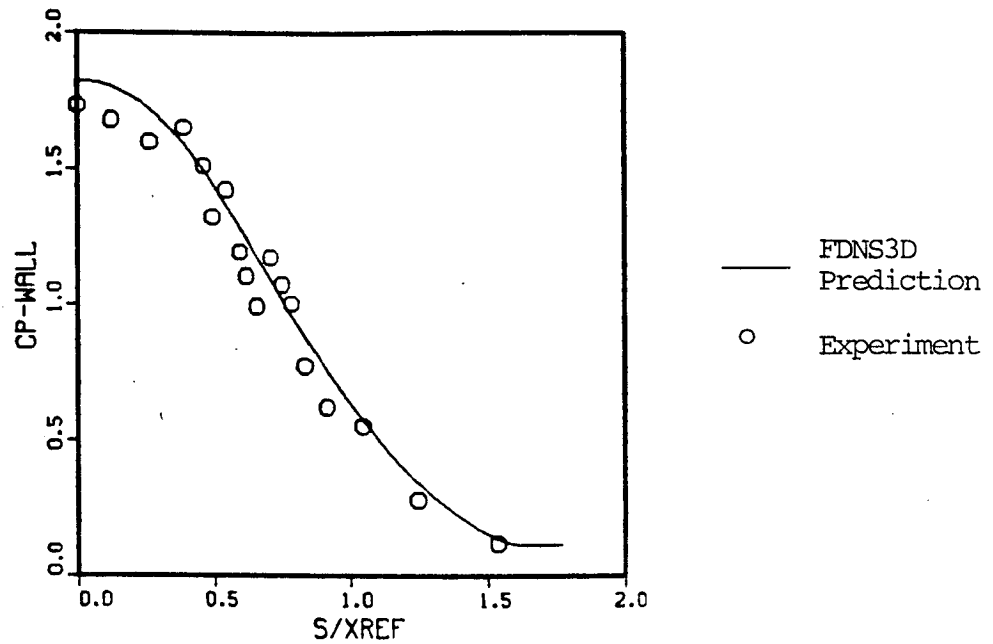
(b) Heat Transfer Coefficient, Stanton No.
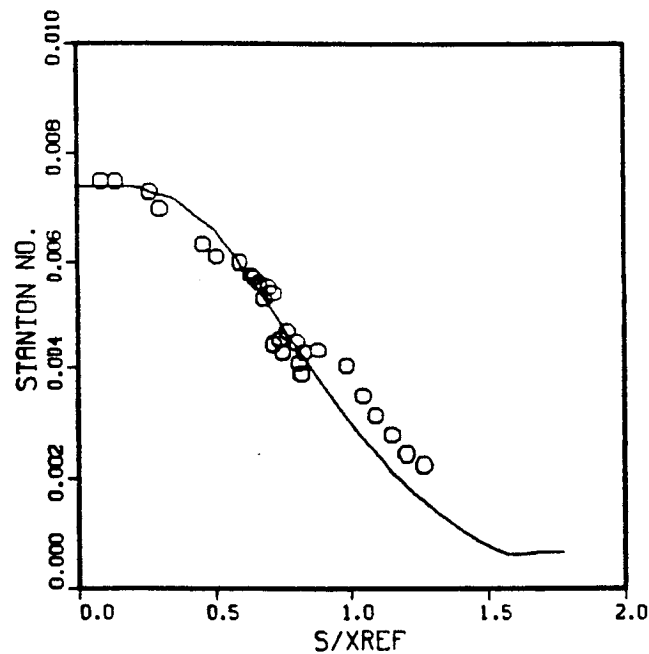
Fig. 56. Comparisons of Surface Pressure and Heat Transfer
Coefficients for a Circular-Cylinder Blunt Body at
$M_{oo} = 8.02$

113

conditions of the AFE model. The measured pressure and heat transfer data in Ref. 23 are the basis of data comparisons for the blunt body test cases. The viscosity at every grid point was updated for every time step based on the solution of the temperature field. Based on these conditions, the Stanton number of the surface heat transfer can be written as:

$$St = q_w/[(\rho U)_o(H_o - h_w)]$$

where:

q_w = (Viscosity) * $(h_p - h_w)/(dy *$ Prandtl No.)
H_o = free stream total enthalpy
h_p = static enthalpy at the near-wall grid point
h_w = static enthalpy based on the wall temperature
dy = wall normal distance between points p and w

b. 3-D Supersonic Turbulent Flow Over an AFE Model
    (for illustration only)

The FDNS3D three-dimensional flow solver has been applied to the solution of the flow over an AFE fore-body configuration. A mesh system with size of 37 x 50 x 40 was used for computation. Figure 57 is an oblique view of the mesh for K = 1 (body surface) and K = 20 (mid-way between the wall and the free stream boundary). This configuration corresponds to a zero angle of attack test case studied in a series of experimental investigations of flow about an AFE model (Ref. 27). The free stream Mach number is 5.835. An ideal gas assumption with specific heat ratio of 1.4 was used. Even though the flow is laminar, for the purposes of this calculation, turbulent flow is
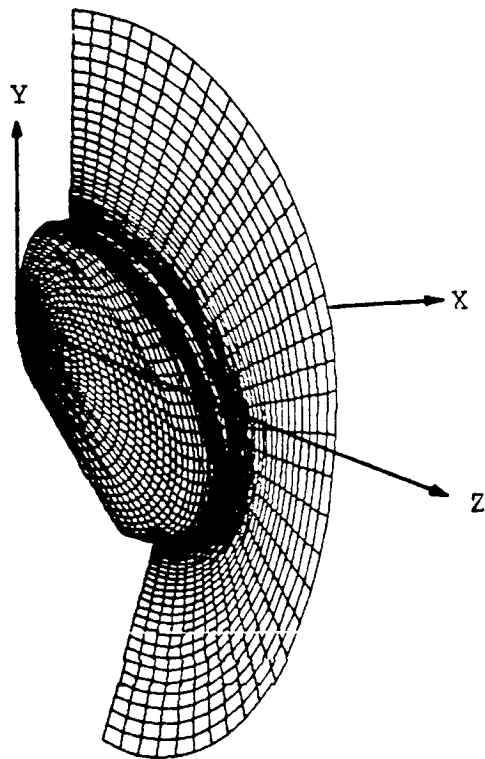
Fig. 57.   Mesh System of an AFE Model

assumed. A time step size of 0.01 was used for numerical integration toward a steady-state solution. A converged solution was obtained in 1200 time steps which corresponds to about 6 hours of CPU time on the Cray-XMP supercomputer. Figure 58 gives the predicted pressure contours around the AFE model. Strong expansions due to the small turning radius are shown clearly around the shoulders at the 0- degree (upper half of Fig. 58a) and 180-degree (lower half of Fig. 58a) locations. Comparisons of the predicted and the measured pressure coefficient (Ref. 27) distributions on the body surface at 0-degree and 180-degree locations are shown in Figs. 59a and 59b respectively. The pressure is slightly over-predicted at the 180-degree location. The FDNS3D turbulent flow results are generally in good agreement with the measured data, even though the flow is thought to be laminar.

c. Supersonic 3-D Laminar Flow Over an AFE Model

Simulations of supersonic turbulent flow past an AFE blunt body in a Mach 5.8 air stream were presented in the previous paragraph. Good comparisons between the measured and predicted surface pressure distributions were obtained. However, discrepancies in the previous heat transfer comparisons were attributed to the inadequacy of the mesh system used. In order to clarify this point, a new mesh system was constructed, using the GWIND GRID module (see Appendix A for a description of this grid generation package). A surface spline routine was used to transform the original surface equations, which define the radial location of surface points of the AFE, into a rectilinear coordinate system. This allows a grid line to pass through the stagnation point (from the 180-degree location to the 0-degree location). This new mesh system consists of no grid singularity lines and preserves much better grid orthogonality, especially
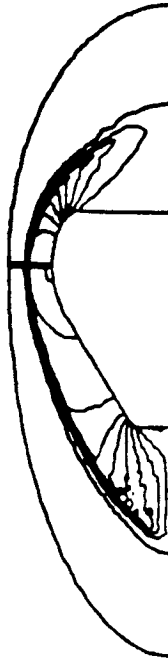
(a)   Side-View
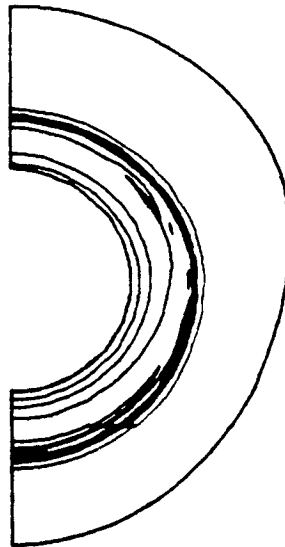
(b)   Front-View

Fig. 58.   FDNS3D Predicted Pressure Contours Around an AFE Model
at $M_{oo} = 5.835$

117
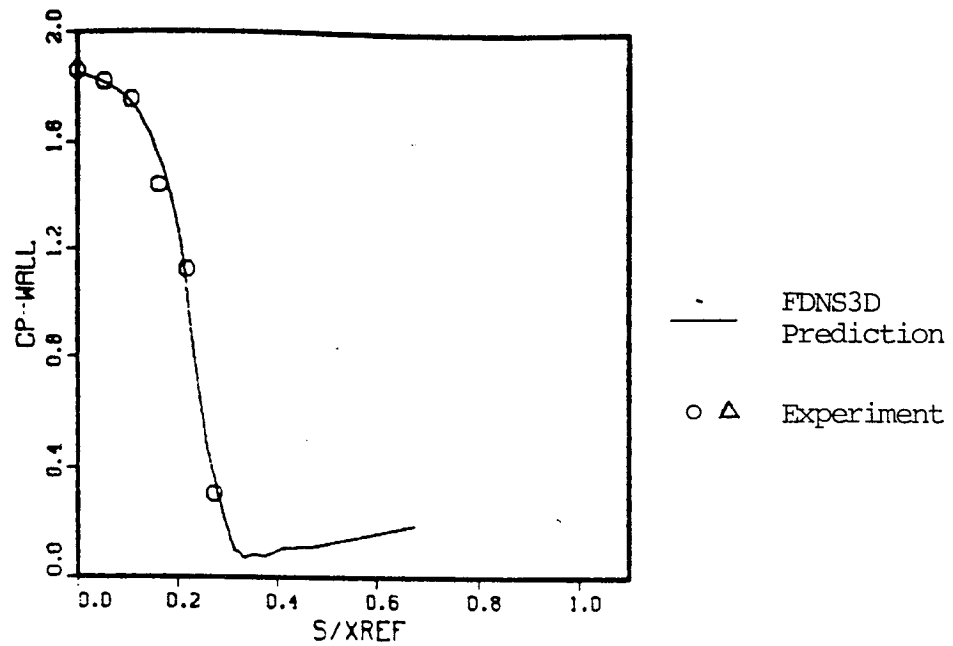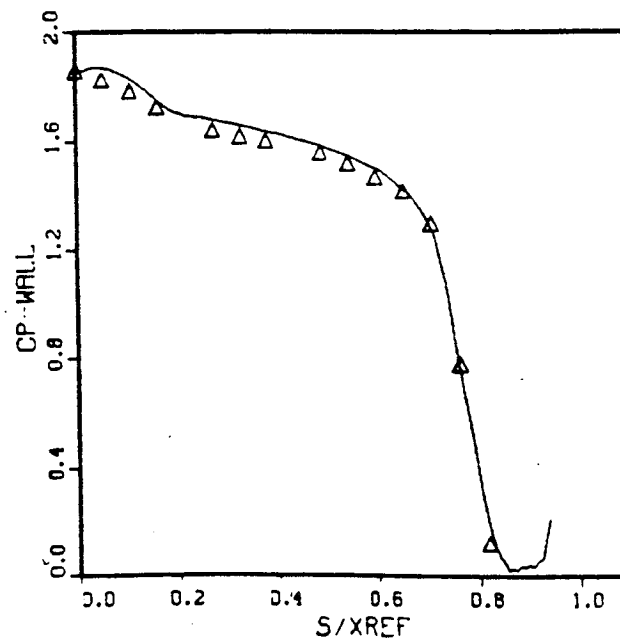
(a) 0-Degree

(b) 180-Degree

Fig. 59. Surface Pressure Distribution Comparisons for 3-D Flow
about an AFE Model at $M_{oo} = 5.835$

118

near the stagnation point. To provide better boundary layer
resolution, more grid points were clustered near the wall
boundary and near the region surrounding the stagnation point.
Figure 60 illustrates the 3-D mesh system. The grid size is 35 x
61 x 41 (total number of grid points is 87,535). This
configuration corresponds to the zero angle-of-attack case
presented in an experimental investigation of an AFE model (Ref.
23). The free stream Mach number is 9.741. An ideal gas
assumption with specific heat ratio of 1.4 was used. The blunt
body flow viscosity law given above was used in the computation.
The flow was assumed to be laminar with Re = 1.6405E+05. A
constant wall temperature (3.5 times the free stream value)
boundary condition was imposed. A time step size of 0.005 was
used for numerical integration to obtain a steady-state solution.
A converged solution was obtained in 1750 time steps which
corresponds to about 7.97 hours of CPU time on the Cray-XMP
supercomputer. Figure 61 gives the predicted pressure and
Stanton number contours on the symmetry plane and the surface of
the AFE model. Strong expansions due to the small turning radii
are clearly shown at the shoulders in the 0-degree and 180-degree
locations. Figure 61 also shows post-shock oscillations in the
solution. This is mainly caused by the course grid used in the
shock region. However, this does not affect the solution on the
surface. Comparisons of the predicted and the measured (Ref. 23)
pressure coefficient and Stanton number distributions along the
symmetry line of the body surface are shown in Figs. 62a and 62b,
respectively. The FDNS3D surface pressure and heat transfer
predictions are in good agreement with the measured data. A
small dip in the Stanton number distribution along the 0-degree
line is also predicted while the experimental data do not show
this effect. The reason for the difference is not yet clear.
Effects of wall temperature distributions (which were measured to
be non-uniform) may have contributed to this problem. However,
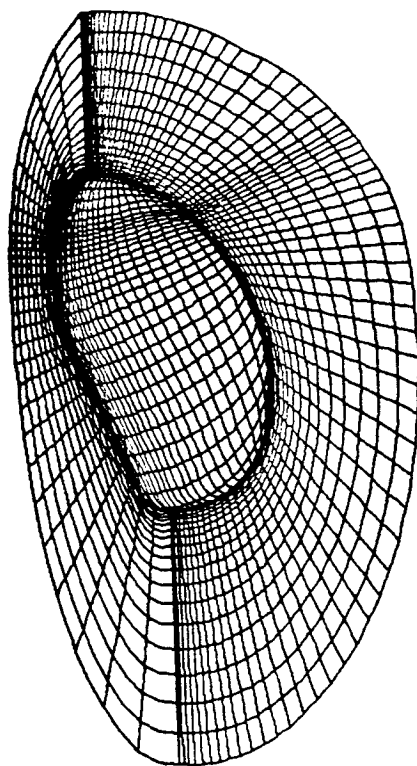
(a)   Perspective-View
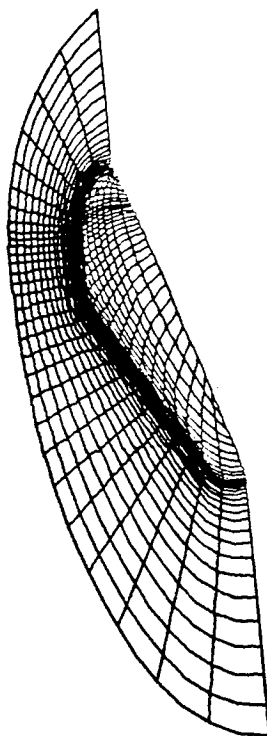
(b)   Side View

Fig. 60.   3-D Mesh System of the AFE Test Model

120
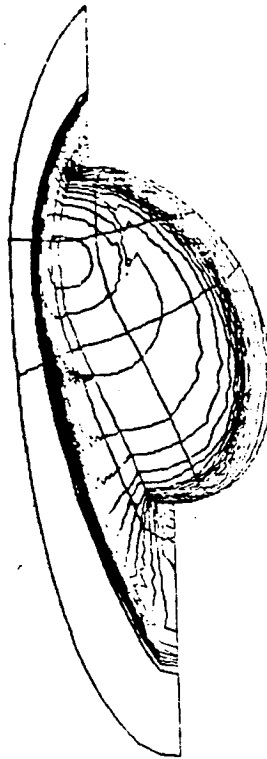
(a)   Pressure Contours
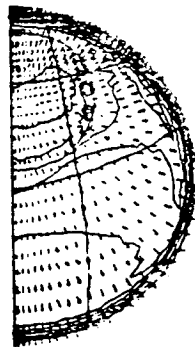
(b) Stanton Number Contours

Fig. 61   AFE Model Predicted Pressure and Stanton Number
Contours, 3-D Laminar Flow at M_{oo} = 9.741
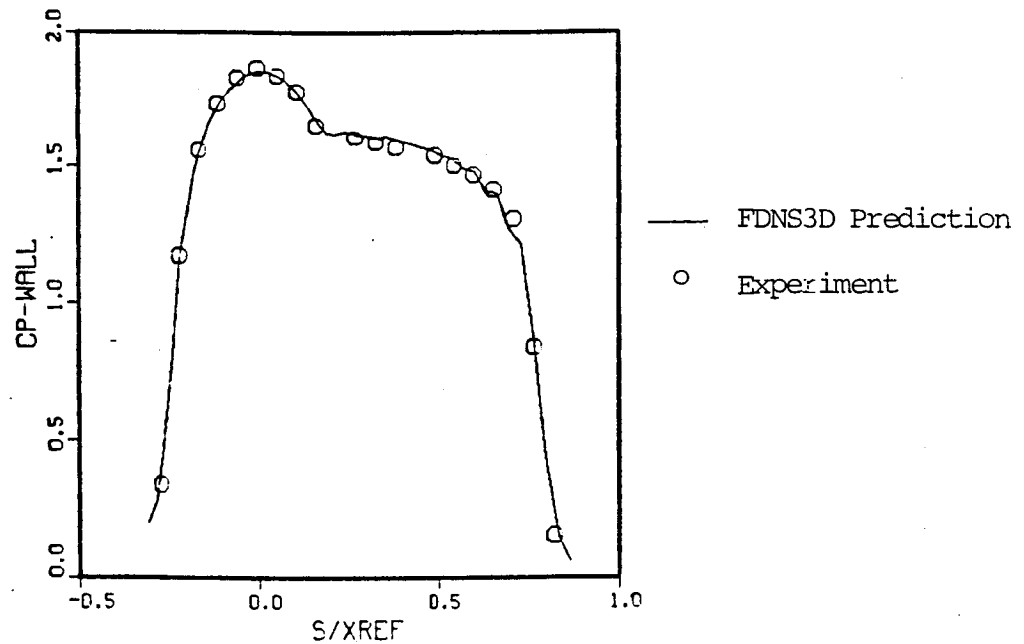
(a) Pressure Coefficient
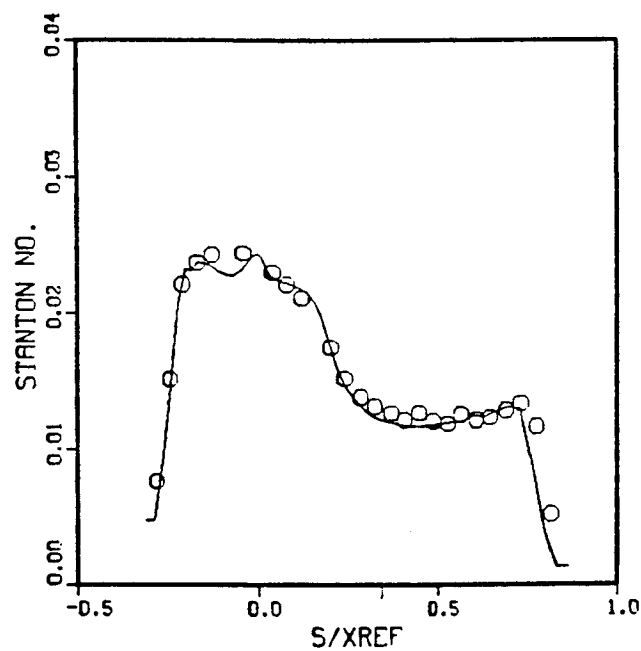
(b) Stanton Number

Fig. 62. Comparisons of Surface Pressure Coefficient and Stanton
No. at Plane of Symmetry on AFE Model, 3-D Laminar Flow
at M_{oo} = 9.741

this discrepancy is still within 10 percent of the test data
which is acceptable for engineering design purposes.

3.5 Clustered Nozzle Flow Field

The computation of a clustered nozzle flow test case
(Ref. 28), using the FDNS3D code, is presented in this section of
the report. A four-nozzle configuration was considered. Only
one eighth of the flow domain was modeled due to symmetry
boundary conditions. A grid system with mesh size of 71 x 33 x
31 was generated using an algebraic grid method. Several
iterations and adjustments to grid spacing distribution and
reductions in local grid skewness were required to obtain a
satisfactory mesh system.

The flow inlet was located at the nozzle exit where an inlet
Mach number was assigned based on the nozzle exit/throat area
ratio. A steady state flow field solution was obtained in 1500
time steps. Figure 63 illustrates the calculated velocity
vectors on two symmetry planes. Strong reversed flow is
predicted in the base region which agrees with the experimental
observations. A data comparison on the base pressure
distribution is shown in Figure 64. The predicted pressure is
somewhat high, but the centerline value is in very good agreement
with the test data. Further analyses of clustered nozzle
problems is recommended, but this study has established that FDNS
can treat this complex problem with fair accuracy.
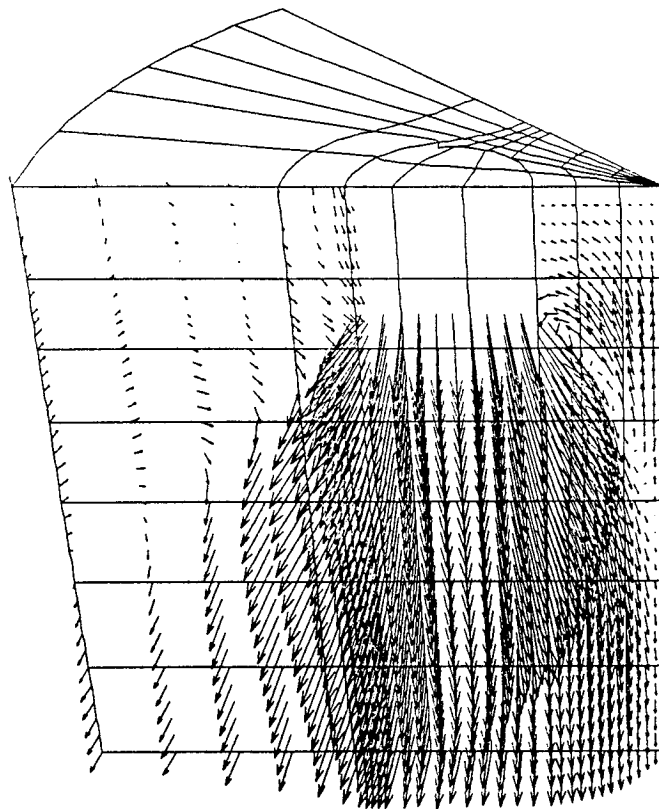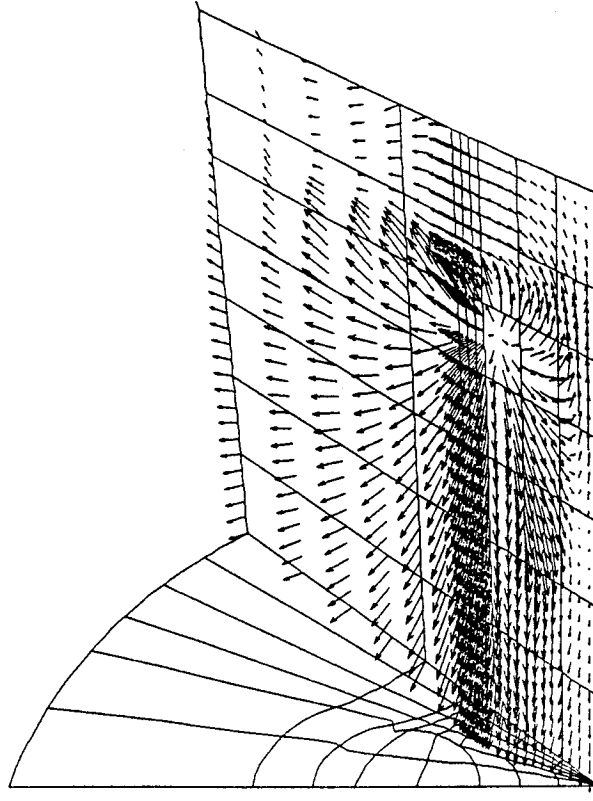
(b)   Symmetry-Plane Between Nozzles

(a)   Nozzle Center-Plane

Fig. 63.   Clustered Nozzle Flow, FDNS3D Calculated Velocity Vector Map

PRESSURE DISTRIBUTIONS ON HEAT SHIELD
ALONG RADIAL LINE BETWEEN NOZZLES
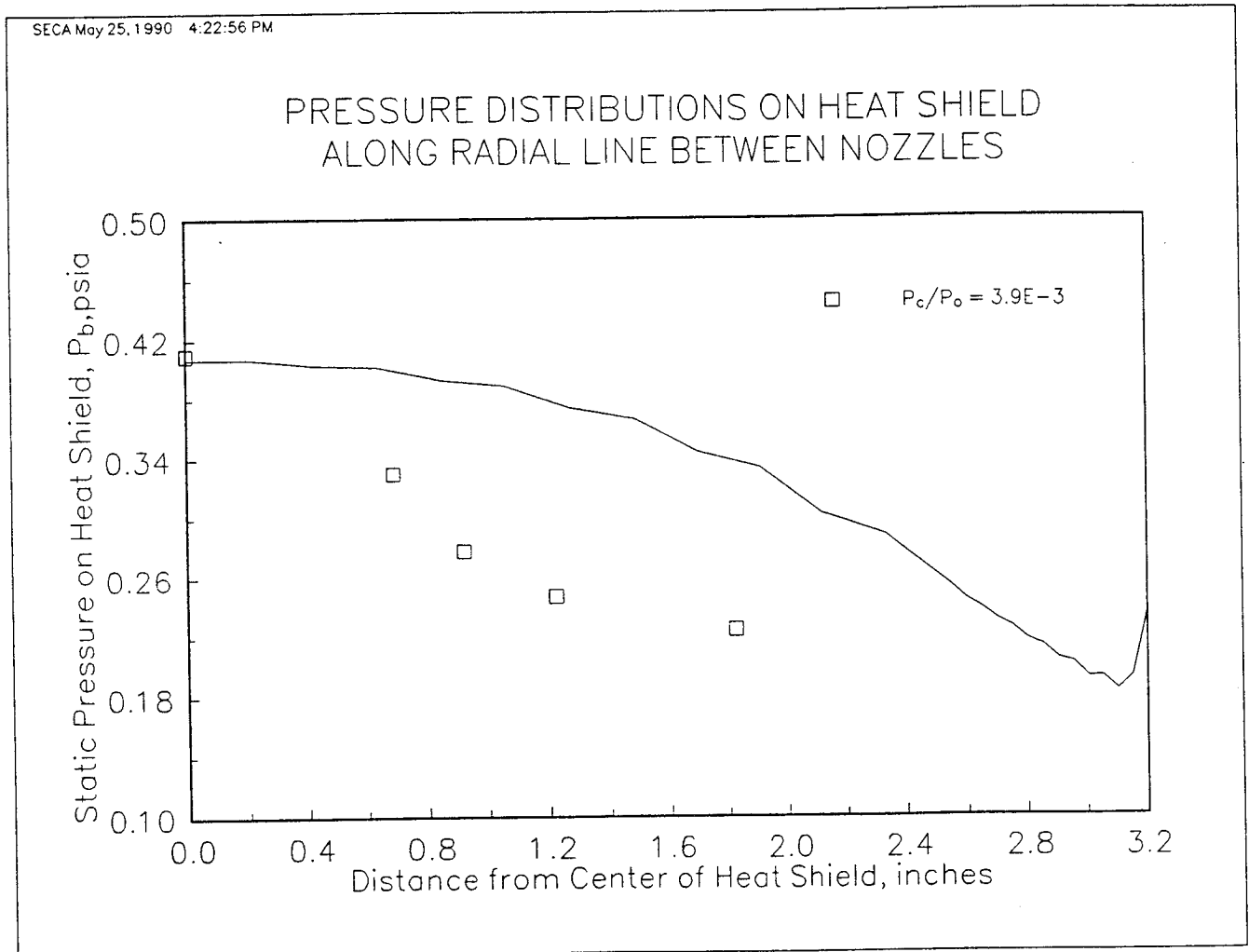
Fig. 64.   Clustered-Nozzle Base-Pressure Comparison

125

4.0 CONCLUSIONS

The capability of the FDNS code to solve a variety of propulsion related problems has been amply demonstrated. New capabilities added to the code and limitations which have been observed in this study are summarized below:

a. Appropriate turbulence models for compressible flow problems, which are essential for accurate simulations, have been incorporated into FDNS. Specific models for expanding plumes and dump combustors have been established by comparing simulations to experimental data.

b. Ideal gas, real gas, equilibrium gas mixtures, and finite rate gas mixtures can be described with the options currently in FDNS. For steady state, there is an accelerated option for performing finite rate calculations which is comparable in speed to equilibrium solutions.

c. The Mach disc solution technique for Mach numbers greater than 3 needs improvement. Logic to locate the triple point and double value this point will probably reduce the smearing of the slip line as it forms, and thus reduce unrealistic recirculation behind the normal shock.

5.0 RECOMMENDATIONS

The emphasis of this study was to validate and establish the range of applicability of a general purpose CFD code. FDNS was used for this purpose; however, now that the utility of the code is established, methods of improving its computational speed can be addressed. Using multigrids and vectorizing the code are recommended for this purpose.

Although GWIND was not developed to the same extent that FDNS was, there are some problems that require an explicit code. Such problems should be identified, and GWIND or a code like it should be developed for these purposes. One example, of such a need for very large problems, is a complete simulation of the AFE configuration.

References

1. Gordon, S., and B.J. McBride, "Computer Program for Calculation of Complex Chemical Equilibrium Compositions, Rocket Performance, Incident and Reflected Shocks, and Chapman-Jouget Detonations," NASA SP-273, Lewis Research Center, Cleveland, Ohio, 1968.

2. Nickerson, G.R., et al, "Two-Dimensional Kinetics (TDK) Nozzle Performance Computer Program Volume II, Programming Manual," SN91, Software and Engineering Associates, Inc., Carson City, NV, 31 March 1989.

3. Chen, Y.S., "Compressible and Incompressible Flow Computations with a Pressure Based Method," AIAA-89-0286, 27th Aerospace Sciences Meeting, Reno, NV, January 9-12, 1989.

4. Amsden, A.A., et al, "KIVA: A Computer Program for Two- and Three-Dimensional Fluid Flows with Chemical Reactions and Sprays," LA-10245-MS, Los Alamos National Laboratory, Los Alamos, NM.

5. Smith, S.D., "High Altitude Chemically Reacting Gas Particle Mixtures - Volumes I, II, and III," LMSC-HREC TR D867400-I, -II, and -III, Lockheed Missiles & Space Company, Huntsville, AL, August 1984.

6. McDonald, H., personal communication, Scientific Research Associates, Inc., Glastonbury, CT , September, 1986.

7. Markarian, P. and P. Kosson, "Standardized Infrared Radiation Model (SIRRM-II), Volume II: user's manual," AFAL-TR-87-098, Grumman Corp., Aircraft Systems Div., Bethridge, N.Y., March 1989.

8. Bernstein, L.S., Wormhoudt, J.C., and Conant, J.A., "The Aerodyne Radiation Code (ARC): Physical Assumptions and Mathematical Approximations," ARI-RR-173, July 1979.

9. Anon., "The Use of Variational Principles in Improving CFD Methodology," Final Report on NAS8-37304, SECA, Inc., Huntsville, AL, July, 1987.

10. Chen, Y.S., "Viscous Flow Computations Using a Second-Order Upwind Differencing Scheme," AIAA Paper 88-0417, AIAA 26th Aerospace Sciences Meeting, Reno, Nevada, January 1988.

11. Chen, Y.S., "3-D Stator-Rotor Interaction of the SSME," AIAA Paper 88-3095, AIAA/ASME/SAE/ASEE 24th Joint Propulsion Conference, Boston, MA, July 1988.

12. Wang, T.S., Chen, Y.S. and Farmer, R., "Numerical Study of Reactive Ramjet Dump Combustor Flowfields with a Pressure Based CFD Method," AIAA Paper 89-2798, AIAA/ASME/SAE/ASEE 25th Joint Propulsion Conference, Monterey, CA, July 1989.

13. Moretti, G., <u>AIAAJ</u>, <u>3</u>, pp. 223-229, 1965.

14. Magnus, D.E. and H.S. Schechter, "Analysis and Application of the Pade' Approximation for Integration of the Chemical Kinetics Equations," GASL TR 642, General Applied Science Laboratories, Inc., Westbury, L.I., NY, 1967.

15. Wang, T.S., et al, "Numerical Investigation of the Transient SSME Fuel Preburner Combustor Flowfield," AIAA Paper No. 90-0646, AIAA 28th Aerospace Sciences Meeting, Reno, Nevada, January 1990.

16. Wang, T.S., Farmer, R.C., and Tucker, K., "Turbulent Hydrocarbon Combustion Kinetics - Stochastic Modeling and Verification," AIAA Paper 89-0486, Jan. 1989.

17. Anon., "Heat Transfer in Rocket Engine Combustion Chambers and Regeneratively Cooled Nozzled," Quarterly Progress Report SECA-PR-90-07, SECA, Inc., Huntsville, AL, April 1990.

18. Chen, Y.S., and Kim, S.W., "Computation of Turbulent Flows Using an Extended $k-\epsilon$ Turbulence Closure Model," NASA CR-179204, Oct. 1987.

19. White, Frank M., <u>Viscous Fluid Flow</u>, McGraw-Hill Book Company, Chapter 7, pp. 576-660, 1974.

20. Schlichting, H., <u>Boundary-Layer Theory</u>, McGraw-Hill Book Company, 1979, p. 339.

21. Holden, M.S., Wieting, A.R., Moselle, J.R., and Glass, C., "Studies of Aerothermal Loads Generated in Regions of Shock/Shock Interactions in Hypersonic Flow," AIAA Paper 88-0477, Jan. 1988.

22. Matthews, R.K., and Eaves, R.H., "Comparison of Theoretical and Experimental Pressure and Heat-Transfer Distributions on

Three Blunt Nosed Cylinders in Hypersonic Flow," AEDC-TR-67-148, 1967.

23.   Micol, J.R., "Experimental and Predicted Pressure and Heating Distributions for an Aeroassist Flight Experiment Vehicle in Air at Mach 10," NASA Langley Research Center, Preliminary Data Release, 1988.

24.   Smith, S.D., and A.W. Ratliff, "User's Manual - Variable O/F Method-of-Characteristics Program for Nozzle and Plume Flowfield Analysis," LMSC-HREC D162220-IV-A. IV, Revision A, Lockheed missiles & Space Company, Huntsville, AL, June 1971 (Revised January 1972).

25.   Evans, R.M., "Boundary Layer Integral Matrix Procedure BLIMP-J User's Manual," Aerotherm UM-75-64, July 1975.

26.   Adamson, T.C., Jr., "The Structure of the Rocket Exhaust Plume without Reaction at Various Altitudes," Rpt. No. 4613-45-T, The Univ. of Mich., Ann Arbor, MI, 1963.

27.   Micol, J.R., "Simulation of Real Gas Effects on Pressure Distributions for a Proposed Aeroassist Flight Experiment Vehicle and Comparison to Prediction," Proposed NASA-TM-89103, February, 1987.

28.   Brewer, Edwin B., and Craven, Charles E., "Experimental Investigation of Base Flow Fiels at Hight Altitude for a Four-Engine Clustered Nozzle Configuration," NASA TN D-5164, May 1969.

APPENDIX A

1.0 INTRODUCTION

The concept of this study was to apply the calculus of
variations to compressible fluid flow in order to develop
accurate, efficient computational fluid dynamics (CFD) algorithms
for production type analyses. The Phase 1 investigation revealed
that the mechanics of a variational solution involves a
predictor-corrector calculation in which a time advanced
approximation is corrected by requiring that certain constraint
equations be satisfied to obtain the final solution. SECA
determined that the time advancement step should most efficiently
be accomplished with a rigorous upwind algorithm which evaluated
wave propagation along characteristic directions. When this
upwind method was implemented, it was found that excellent
solutions were obtained without requiring additional correction
steps. The Phase 2 effort will, therefore, be devoted to
utilizing and validating the upwind, explicit algorithm (GWIND)
and to developing an upwind, implicit counterpart designed
specifically for steady state problems. This first quarterly
progress report on the Phase 2 study will describe the GWIND code
and the test cases to be used for its validation and outline the
approach to be used for developing the implicit solution
methodology.

2.0 GWIND

2.1 General Description

GWIND is a general Navier-Stokes equation solver developed
by SECA, Inc. to be used to provide solutions to complex gas
dynamics problems. GWIND currently operates in either 2-D or
axisymmetric modes with inviscid, laminar, and turbulent options
for steady or unsteady flows of ideal gas mixtures. The code is
being extended to 3 dimensions and to real gas mixtures.

GWIND consists of four modules: a geometry module, a pre-
processor, an integrator, and a graphics module. Each of the four
modules are driven by menus designed to make the module user
friendly. Since the code is still under development, research
versions reside on SECA's Acer PC and on MSFC's CRAY/IBM
mainframe. The mainframe version has been vectorized and is in
the process of being modified to reflect the latest improvements.

The current state of development for each of the modules is
presented in the following sections.

2.2 Pre-Processor

The role of the pre-processor has been expanded from
assigning boundary and initial conditions to also include
preparing runstreams for the CRAY, offering choices for the grid

generator and integrator to be used, and providing interaction
with plotting packages. The pre-processor is used to prepare the
input and CRAY runstreams for all the GWIND modules like GRID,
DEFINE and INTEG. The GEOMETRY module not only runs the GWIND
module GRID, but also includes an interactive grid generator -
GENIE. The post-processor rearranges the data files so that
PLOT3D can be used for presenting the final computational
results. The GWIND interactive package is written in IBM TSO
language.

The pre-processor module also assigns boundary conditions to
each node, assigns initial conditions to each node which may be
either constant valued or linearly interpolated values,
establishes tables of data to be used with certain boundary
conditions, and generates tables of common nodes used to mate
regions in the integrator.

The pre-processor uses the grid generated by the geometry
module and, along with the boundary and initial conditions,
creates the geometry and initial flow field data file for input
to the integrator module.

2.3 Geometry

The internal geometry module, GRID, is an algebraic grid
generator capable of creating 2-D, axisymmetric and 3-D grids
over complex fluid flow regions. The module uses a library of
edge and surface shape functions which may be bilinearly or
trilinearly blended to obtain a body fitted coordinate system.

The shape functions currently in the module include;
straight edges, a set of fixed points, circular arcs, elliptical
arcs, parabolic arcs and helical arcs. Surface shapes available
are flat plates, cylindrical surfaces, cones, spheres, biconics
and edges of revolution.

Each edge of the region may consist of more than one shape
and each surface may consist of segments of different shapes. In
addition, intermediate edges may be imposed on any of the
surfaces to facilitate modelling complex features or the
geometry.

Other helpful features of the module are the capability to
employ uneven nodal distributions via a quadratic stretching
function and the capability to divide a complex geometry into
separate, distinct regions to be mated in the pre-processor
module.

Grids may also be provided by GENIE instead of GRID by
selecting this option in the pre-processor. Other grid package
options may be provided at this point.

2.4 Graphics

The mainframe graphics module utilizes PLOT3D to produce grid and contour plots of flow properties. PLOT3D uses files of computed flow variables along with internal conversions, assuming an ideal gas, to make the plots of user selected functions. The user may provide the converted file prior to calling PLOT3D to obtain more general results, i.e. real gas properties. SECA can transfer these files to its faciltiy via a modem to view the plots on a CRT or print the figures. Currently, to make and print such plots on MSFC's IRIS machines, a tape of the computed data must be prepared and reloaded on the IRIS machines.

The PC graphics module is written in Microsoft's QuickBasic and employs an Enhanced Graphics Adapter (EGA) installed on the PC AT. The graphics module is capable of plotting the geometry as well as flow properties such as density, pressure, Mach number, temperature or streamlines. The grid or an outline of the grid may be superimposed on the flow property plots. The flow properties are plotted using up to 50 constant property contour lines which may either be shaded in various colors between contours or simply discrete colored lines. The EGA is limited to sixteen colors which are repeated if more than sixteen contours are requested.

2.5 Integrator

The integrator module offers a selection of algorithms for solving the conservation equations. An explicit, windward differencing algorithm is currently operational; an implicit, windward differencing algorithm is under development. With either option, the viscous terms are resolved separately using conventional central differencing and will not be included in the following discussion.

Explicit Algorithm

The explicit windward algorithm is a finite volume flux splitting algorithm which guarantees total conservation in the integral sense by employing the elemental flux integrals to form the spatial derivatives found in the conservation equations. The derivation of the algorithm follows.

For 2-D and axisymmetric flow, the conservation equations may be cast in the form:

$$Q_t + F_x + G_y + \sigma H/y = 0$$

$$Q = [\rho, \ \rho u, \ \rho v, \ \rho E_T]^T$$

$$F = [\rho u, \ \rho u^2 + P, \ \rho uv, \ \rho uH_T]^T$$

$$G = [\rho v, \; \rho uv, \; \rho v^2 + P, \; \rho vH_T]^T$$

$$H = [\rho v, \; \rho uv, \; \rho v^2, \; \rho vH_T]^T$$

where t is time; x & y are Cartesian coordinates; u & v are velocity components in the x & y directions, respectively; ρ is density; P is pressure; E_T is total specific internal energy; and H_T is total specific enthalpy.

The conservation equations may be transformed to local, computational coordinates (ξ, η), such that $\Delta\xi = \Delta\eta = 1$ in the following manner.

$$(y^\sigma/J)Q_t + (y^\sigma \; \hat{F})_\xi + (y^\sigma \; \hat{G})_\eta + \sigma\hat{H} = 0$$

where:

$$J = \xi_x \; \eta_y - \xi_y \; \eta_x$$

$$\xi_x = J \; y_\eta \qquad\qquad \eta_x = - \; J \; y_\xi$$

$$\xi_y = - \; J \; x_\eta \qquad\qquad \eta_y = J \; x_\xi$$

$$\hat{F} = [\rho\hat{U}, \; \rho u\hat{U} + \xi_x \, P/J, \; \rho v\hat{U} + \xi_y \, P/J, \; \rho\hat{U}H_T]^T$$

$$\hat{G} = [\rho\hat{V}, \; \rho u\hat{V} + \eta_x \, P/J, \; \rho v\hat{V} + \eta_y \, P/J, \; \rho\hat{V}H_T]^T$$

$$\hat{H} = [0, \; 0, \; -P/J, \; 0]^T$$

$$\hat{U} = (\xi_x/J)u + (\xi_y/J)v \qquad \text{and} \qquad \hat{V} = (\eta_x/J)u + (\eta_y/J)v$$

The vectors $\hat{F}$ and $\hat{G}$ can be locally linearized by first obtaining the Jacobian matrices using the formulas

$$\hat{F}_\xi = \frac{\partial\hat{F}}{\partial Q} Q_\xi = A \; Q_\xi \qquad\qquad \hat{G}_\eta = \frac{\partial\hat{G}}{\partial Q} Q_\eta = B \; Q_\eta$$

The mathematical treatment of the Jacobian matrices A and B is identical, therefore by letting D represent A or B, n represent ξ/J or η/J, and $U = n_x u + n_y v$, the D matrix becomes

$$D = \begin{bmatrix} 0 & n_x & n_y & 0 \\ -uU + n_x\theta^2 & U + (1-\alpha)un_x & un_y - \alpha vn_x & \alpha n_x \\ -vU + n_y\theta^2 & vn_x - \alpha un_y & U + (1-\alpha)vn_y & \alpha n_y \\ U(\theta^2 - H_T) & H_T n_x - \alpha uU & H_T n_y - \alpha vU & (1+\alpha)U \end{bmatrix}$$

where: $\theta^2 = 0.5(\gamma-1)q^2$, $\alpha = (\gamma-1)$, $P = \alpha[\rho E_T - 0.5\rho q^2]$ and

135

$$q^2 = u^2 + v^2$$

The D matrix was derived using the following derivatives of the pressure:

$$P_\rho = \theta^2, \quad P_{\rho u} = -\alpha u, \quad P_{\rho v} = -\alpha v, \quad P_{\rho ET} = \alpha$$

The eigenvalues for the matrix D are:

$$\lambda = [U, \ U, \ U + nC, \ U - nC]$$

where $n = (n_x^2 + n_y^2)^{0.5}$.

The eigenvector matrix for D is derived by solving the following relationship for each of the four eigenvalues.

$$(D - \lambda)Q_n = 0$$

In expanded form the above relationship becomes

$$
\begin{bmatrix}
-\lambda & n_x & n_y & 0 \\
-uU+n_x\theta^2 & U+(1-\alpha)un_x-\lambda & un_y-\alpha vn_y & \alpha n_x \\
-vU+n_y\theta^2 & v\xi_x-\alpha un_y & U+(1-\alpha)vny-\lambda & \alpha n_y \\
U(\theta^2-H_T) & H_Tn_x-\alpha uU & H_Tn_y-\alpha vU & (1+\alpha)U-\lambda
\end{bmatrix} Q_n = 0
$$

The resultant eigenvector matrix is

$$
M_D =
\begin{bmatrix}
1 & 0 & 1 & 1 \\
u & n_y & u+\hat{n}_xC & u-\hat{n}_xC \\
v & -n_x & v+\hat{n}_yC & v-\hat{n}_yC \\
q^2/2 & -V & H_T+UC/n & H_T-UC/n
\end{bmatrix}
$$

where $V = n_xv - n_yu$, $\hat{n}_x = n_x/n$, $\hat{n}_y = n_y/n$, and C is the speed of sound. The determinant of the eigenvector martix is

$$|M_D| = 2\ C^3\ n/\alpha$$

The inverse of M_D is obtained using the standard formula

$$M_D^{-1} = M_{ji} / M_D$$

where $M_{ij} = (-1)^{i+j} m_{ij}$ and m_{ij} are the minors of M_D. Then

$$M_D^{-1} = (\alpha/C^2) \begin{bmatrix} H_T - q^2 & u & v & -1 \\ VC^2/\alpha n^2 & n_y C^2/\alpha n^2 & -n_x C^2/\alpha n^2 & 0 \\ q^2/4 - UC/2\alpha n & n_x/2\alpha n - u/2 & n_y C/2\alpha n - v/2 & 0.5 \\ q^2/4 + UC/2\alpha n & -(n_x C/2\alpha n + u/2) & -n_y C/2\alpha n - v/2 & 0.5 \end{bmatrix}$$

It has been verified that $M_D M_D^{-1}$ is equal to the identity matrix.

The matrix D may be spectrally decomposed into components corresponding to each of the eigenvalues by using the spectral theorem. Since two of the eigenvalues are identical the decomposition results in only three components. These components are obtained by performing the following matrix multiplies

$$D = M_D \quad U \begin{bmatrix} 1 & & & \\ & 1 & & \\ & & 0 & \\ & & & 0 \end{bmatrix} + (U+nC) \begin{bmatrix} 0 & & & \\ & 0 & & \\ & & 1 & \\ & & & 0 \end{bmatrix} + (U-nC) \begin{bmatrix} 0 & & & \\ & 0 & & \\ & & 0 & \\ & & & 1 \end{bmatrix} \quad M_D^{-1}$$

$$D = D_1 + D_2 + D_3$$

$$D_1 = (\alpha \, U/C^2) \times$$

$$\begin{bmatrix} C^2/\alpha - q^2/2 & u & v & -1 \\ n_x UC^2/\alpha n^2 - uq^2/2 & u^2 + n_y{}^2 C^2/\alpha n^2 & uv - n_x n_y C^2/\alpha n^2 & -u \\ n_y UC^2/\alpha n^2 - vq^2/2 & uv - n_x n_y C^2/\alpha n^2 & v^2 + n_x{}^2 C^2/\alpha n^2 & -v \\ U^2 C^2/\alpha n^2 - q^2 H_T/2 & uq^2/2 - n_y VC^2/\alpha n^2 & vq^2/2 + n_x VC^2/\alpha n^2 & -q^2/2 \end{bmatrix}$$

$$D_2 = [\alpha(U+nC)/2C^2] \times$$

$$
\begin{bmatrix}
W_1 & W_2 & W_3 & 1 \\
W_1(u+\hat{n}_xC) & W_2(u+\hat{n}_xC) & W_3(u+\hat{n}_xC) & u+\hat{n}_xC \\
W_1(v+\hat{n}_yC) & W_2(v+\hat{n}_yC) & W_3(v+\hat{n}_yC) & v+\hat{n}_yC \\
W_1(H_T+UC/n) & W_2(H_T+UC/n) & W_3(H_T+UC/n) & H_T+UC/n
\end{bmatrix}
$$

where $W_1 = (0.5q^2 - UC/\alpha n)$, $W_2 = (n_xC/\alpha n - u)$, and

$$W_3 = (n_yC/\alpha n - v)$$

$$D_3 = [\alpha(U-nC)/2C^2] \times$$

$$
\begin{bmatrix}
W_4 & W_5 & W_6 & 1 \\
W_4(u-\hat{n}_xC) & W_5(u-\hat{n}_xC) & W_6(u-\hat{n}_xC) & u-\hat{n}_xC \\
W_4(v-\hat{n}_yC) & W_5(v-\hat{n}_yC) & W_6(v-\hat{n}_yC) & v-\hat{n}_yC \\
W_4(H_T-UC/n) & W_5(H_T-UC/n) & W_6(H_T-UC/n) & H_T-UC/n
\end{bmatrix}
$$

where $W_4 = (0.5q^2 + UC/\alpha n)$, $W_5 = -(n_xC/\alpha n + u)$ and

$$W_6 = -(n_yC/\alpha n + v)$$

The quantity DQ_n now becomes $(D_1 + D_2 + D_3)Q_n$ where D_1 has eigen direction U, D_2 has eigen direction $U + nC$ and D_3 has eigen direction $U - nC$. Recall that DQ_n represents either

$$F_\xi = (F_1)_\xi + (F_2)_\xi + (F_3)_\xi$$

or $$G_\eta = (G_1)_\eta + (G_2)_\eta + (G_3)_\eta$$

The components D_1, D_2 and D_3 may be simplified by applying the chain rule to replace derivatives of (ρE_T) with derivatives of P. An ideal gas will be assumed at this point, i.e. one which is both thermally and calorically perfect. The relationship between pressure and total energy becomes

$$P = \alpha\rho(E_T - 0.5\ q^2)$$

Then

$$P_n = \alpha[\ 0.5q^2\rho_n - u(\rho u)_n - v(\rho v)_n + (\rho E_T)_n\ ]$$

Another simplification involves using the chain rule to replace $(\rho u)_n$ and $(\rho v)_n$ with $(\rho U)_n$ and $(\rho V)_n$. These two operations reduce the complicated component matrices into much more simplified forms, namely:

$$D_i Q_n = D^*_i Q^*_n, \quad \text{where } Q^* = [\rho,\ \rho U,\ \rho V,\ P]^T \quad \text{and}$$

$$D^*_1 = U \begin{bmatrix} 1 & 0 & 0 & -1/C^2 \\ n_x U/n^2 & 0 & -n_y/n^2 & -u/C^2 \\ n_y U/n^2 & 0 & n_x/n^2 & -v/C^2 \\ U^2/n^2 - q^2/2 & 0 & V/n^2 & -q^2/2C^2 \end{bmatrix}$$

$$D^*_2 = \frac{U+nC}{2nC} \begin{bmatrix} -U & 1 & 0 & n/C \\ -U(u+\hat{n}_x C) & u+\hat{n}_x C & 0 & n(u/C+\hat{n}_x) \\ -U(v+\hat{n}_y C) & v+\hat{n}_y C & 0 & n(v/C+\hat{n}_y) \\ -U(H_T+UC/n) & H_T+UC/n & 0 & n(H_T/C+U/n) \end{bmatrix}$$

$$D^*_3 = \frac{U-nC}{2nC} \begin{bmatrix} U & -1 & 0 & n/C \\ U(u-\hat{n}_x C) & -(u-\hat{n}_x C) & 0 & n(u/C-\hat{n}_x) \\ U(v-\hat{n}_y C) & -(v-\hat{n}_y C) & 0 & n(v/C-\hat{n}_y) \\ U(H_T-UC/n) & -(H_T-UC/n) & 0 & nH_T/C-U \end{bmatrix}$$

$D^*_1 Q^*_n$ can be expanded by noting that

$$(\rho U)_n = (\rho U)_n$$

$$(\rho u U)_n = -u U \rho_n + (u + \hat{n}_x \bar{U})(\rho U)_n - \hat{n}_y \bar{U}(\rho V)_n$$

$$(\rho v U)_n = -v U \rho_n + (v + \hat{n}_y \bar{U})(\rho U)_n + \hat{n}_x \bar{U}(\rho V)_n$$

$$(\rho U H_T)_n = -U(H_T + 0.5q^2)\rho_n + (H_T + U^2)(\rho U)_n$$

$$+ \bar{U}V(\rho V)_n + \gamma U P_n/\alpha$$

where $\hat{U} = U/n$, so that

$$D^*_1 Q^*_n = \{[\rho U, \ \rho u U + n_x P, \ \rho v U + n_y P, \ \rho U H_T]^T\}_n$$

$$+ \ [U\rho_n - (\rho U)_n] \times [1, \ u + \hat{n}_x \hat{U}, \ v + \hat{n}_y \hat{U}, \ H_T + \hat{U}^2]^T$$

$$- \ (nP_n/C^2) \times [\hat{U}, \ u\hat{U} + \hat{n}_x C^2, \ v\hat{U} + \hat{n}_y C^2, \ \hat{U}(H_T + C^2)]^T$$

$D^*_2 Q^*_n$ and $D^*_3 Q^*_n$ can also be expanded to yield

$$D^*_2 Q^*_n = - \ 0.5[U\rho_n - (\rho U)_n] \times [1, \ u + \hat{n}_x \hat{U}, \ v + \hat{n}_y \hat{U}, \ H_T + \hat{U}^2]^T$$

$$+ \ (nP_n/2C^2) \times [\hat{U}, \ u\hat{U} + \hat{n}_x C^2, \ v\hat{U} + \hat{n}_y C^2, \ \hat{U}(H_T + C^2)]^T$$

$$- \ \{[U\rho_n - (\rho U)_n]/2C\} \times$$

$$[\hat{U}, \ u\hat{U} + \hat{n}_x C^2, \ v\hat{U} + \hat{n}_y C^2, \ \hat{U}(H_T + C^2)]^T + (nP_n/2C) \times$$

$$[1, \ u + \hat{n}_x \hat{U}, \ v + \hat{n}_y \hat{U}, \ H_T + \hat{U}^2]^T$$

$$D^*_3 Q^*_n = - \ 0.5[U\rho_n - (\rho U)_n] \times [1, \ u + \hat{n}_x \hat{U}, \ v + \hat{n}_y \hat{U}, \ H_T + \hat{U}^2]^T$$

$$+ \ (nP_n/2C^2) \times [\hat{U}, \ u\hat{U} + \hat{n}_x C^2, \ v\hat{U} + \hat{n}_y C^2, \ \hat{U}(H_T + C^2)]^T$$

$$+ \ \{[U\rho_n - (\rho U)_n]/2C\} \times$$

$$[\hat{U}, \ u\hat{U} + \hat{n}_x C^2, \ v\hat{U} + \hat{n}_y C^2, \ \hat{U}(H_T + C^2)]^T - (nP_n/2C) \times$$

$$[1, \ u + \hat{n}_x \hat{U}, \ v + \hat{n}_y \hat{U}, \ H_T + \hat{U}^2]^T$$

Components of these equations are grouped and named as follows.

$$F = \{[\rho U, \ \rho u U + n_x P, \ \rho v U + n_y P, \ \rho U H_T]^T\}_n$$

$$f_1 = + \ [U\rho_n - (\rho U)_n] \times [1, \ u + \hat{n}_x \hat{U}, \ v + \hat{n}_y \hat{U}, \ H_T + \hat{U}^2]^T$$

$$f_2 = + \ (nP_n/C^2) \times [\hat{U}, \ u\hat{U} + \hat{n}_x C^2, \ v\hat{U} + \hat{n}_y C^2, \ \hat{U}(H_T + C^2)]^T$$

$$f_3 = + \ \{[U\rho_n - (\rho U)_n]/C\} \times [\hat{U}, \ u\hat{U} + \hat{n}_x C^2, \ v\hat{U} + \hat{n}_y C^2, \ \hat{U}(H_T + C^2)]^T$$

$$f_4 = (nP_n/C) \times [1, \ u + \hat{n}_x \hat{U}, \ v + \hat{n}_y \hat{U}, \ H_T + \hat{U}^2]^T$$

Note that F is identical to either F_ξ or G_η. These groupings allow the following representation of the F's (or G's).

$$(F_1)_n = F + f_1 - f_2$$

$$(F_2)_n = 0.5(f_2 - f_1) + 0.5(f_4 - f_3)$$

$$(F_3)_n = 0.5(f_2 - f_1) - 0.5(f_4 - f_3)$$

Again the eigen directions of F_1, F_2 and F_3 are U, $U + nC$ and $U - nC$, respectively.

Once the flux components have been evaluated, the windward algorithm determines which nodes in the element receive each of the flux components. The windward algorithm is stated as:

$$F_n = e_1(F_1)_n + e_2(F_2)_n + e_3(F_3)_n$$

where: $e_1 = 1$ if $U \geq 0$

$\qquad = 0$ if $U < 0$

$\qquad e_2 = 1$ if $U + nC \geq 0$

$\qquad = 0$ if $U + nC < 0$

$\qquad e_3 = 1$ if $U - nC \geq 0$

$\qquad 0$ if $U - nC < 0$

For supersonic flow, $e_1 = e_2 = e_3$, so that

$$F_n = e_1(F_1 + F_2 + F_3)_n$$

$$= e_1[F + f_1 + f_2 + 0.5*(f_2 - f_1 + f_4 - f_3)$$

$$+ 0.5*(f_2 - f_1 - f_4 + f_3)]$$

$$= e_1 F = e_1(F)_n$$

For subsonic flow where $U < nC$ the e's may be redefined as:

$$e_1 = 0.5(1 + \Gamma_1), \quad \text{where } \Gamma_1 = SIGN(U)$$

$$e_2 = 0.5(1 + \Gamma_2), \quad \text{where } \Gamma_2 = SIGN(U+nC) = SIGN(n)$$

$$e_3 = 0.5(1 + \Gamma_3), \quad \text{where } \Gamma_3 = SIGN(U-nC) = SIGN(-n) = - \Gamma_2$$

In subsonic flow any node in the flow grid will have either e_2 or e_3 equal to unity and the other equal to zero, therefore for any node

$$F_n = 0.5[(1+\Gamma_1)F + \Gamma_1(f_1-f_2) + \Gamma_2(f_4-f_3)]$$

By simply evaluating the signs on U for supersonic flow and for U and n for subsonic flow the algorithm automatically determines the proper directions in which to difference the three components of the flux vectors. The method by which the differencing is accomplished in GWIND is described below.

GWIND employs a numbering system convention which applies to

each element in the flow field regardless of orientation. This
numbering system is detailed below.

Typical Element
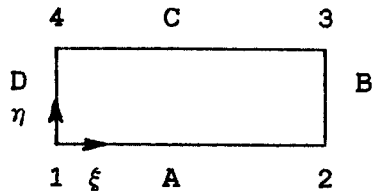
Nodes: 1 - 4
Faces: A - D
Elements do not need to be
rectangles; sketch indicates
numbering system only.

The position vector for any point in the element is $P = [x, y]^T$
or

$$P = (1-\xi)(1-\eta)P_1 + \xi(1-\eta)P_2 + \xi\eta P_3 + (1-\xi)\eta P_4$$

$$P_\xi = (1-\eta)(P_2 - P_1) + \eta(P_3 - P_4)$$

$$P_\eta = (1-\xi)(P_4 - P_1) + \xi(P_3 - P_2)$$

$$|A| = x_\xi y_\eta - x_\eta y_\xi = 1/J$$

In order to understand the physical interpretation of the
equations used in the algorithm, first note that the outward-
pointing normals

$$\vec{N} = N_x \vec{i} + N_y \vec{j}$$

on each face of the element are:

Face	$\underline{N}_x$	$\underline{N}_y$
A	y_2-y_1	x_1-x_2
B	y_3-y_2	x_2-x_3
C	y_4-y_3	x_3-x_4
D	y_1-y_4	x_4-x_1

Evaluation of the derivatives P_ξ and P_η at each node of the
element yields

Node	$\underline{x}_\xi$	$\underline{y}_\xi$	$\underline{x}_\eta$	$\underline{y}_\eta$
1	x_2-x_1	y_2-y_1	x_4-x_1	y_4-y_1
2	x_2-x_1	y_2-y_1	x_3-x_2	y_3-y_2
3	x_3-x_4	y_3-y_4	x_3-x_2	y_3-y_2
4	x_3-x_4	y_3-y_4	x_4-x_1	y_4-y_1

But from before

$$\xi_x = J\, y_\eta \qquad\qquad \eta_x = -\, J\, y_\xi$$

$$\xi_y = -\, J\, x_\eta \qquad\qquad \eta_y = J\, x_\xi$$

so that

Node	ξ_x	ξ_y	η_x	η_y
1	$-\,J_1\, N_{xD}$	$-\,J_1\, N_{yD}$	$-\,J_1\, N_{xA}$	$-\,J_1\, N_{yA}$
2	$J_2\, N_{xB}$	$J_2\, N_{yB}$	$-\,J_2\, N_{xA}$	$-\,J_2\, N_{yA}$
3	$J_3\, N_{xB}$	$J_3\, N_{yB}$	$J_3\, N_{xC}$	$J_3\, N_{yC}$
4	$-\,J_4\, N_{xD}$	$-\,J_4\, N_{yD}$	$J_4\, N_{xC}$	$J_4\, N_{yC}$

Therefore $\nabla\xi/J$ and $\nabla\eta/J$ are area normals at the 2 faces associated with each node in the positive ξ and η directions. U is the dot product of the velocity vector and the area normal vector. Therefore, the local computational coordinate form of the conservation equations represents the fluxes through the faces of the element and are, in fact, identical to the flux integral form of the conservation equations. GWIND departs from standard finite difference methods at this point by employing the integral form of the equations and actually integrating the fluxes through each element. This results in a finite volume integral approach using a windward algorithm.

The above table reveals that ξ_x and ξ_y involve only the normals on faces B and D of the typical element while η_x and η_y only involve the normals on faces A and C. Consequently, F is evaluated only on faces B and D while G is evaluated only on faces A and C.

The adopted convention for the typical element, with its numbering system for the nodes and faces relative to the ξ and η directions, dictates the following for $\Gamma_2 = \text{SIGN}(n)$. The outward-pointing normal for face B points in the direction of positive ξ

while the outward-pointing normal for face D points in the negative ξ direction. Therefore,

$$\Gamma_2 = 1 \text{ for nodes 2 \& 3 for } \hat{F}_\xi$$

$$= -1 \text{ for nodes 1 \& 4 for } \hat{F}_\xi$$

Likewise, the outward-pointing normal directions for faces A and C dictate that

$$\Gamma_2 = 1 \text{ for nodes 3 \& 4 for } \hat{G}_\eta$$

$$= -1 \text{ for nodes 1 \& 2 for } \hat{G}_\eta$$

If U_a is defined as the average U in either the ξ or η direction, recalling that U is the dot product of the velocity and area normal vectors, then, since the area normal vectors on opposite faces have opposite signs, the following is true:

$$\Gamma_1 = \text{SIGN}(U_a) \text{ for nodes 2 \& 3 for } \hat{F}_\xi$$

$$= -\text{SIGN}(U_a) \text{ for nodes 1 \& 4 for } \hat{F}_\xi$$

$$\Gamma_1 = \text{SIGN}(U_a) \text{ for nodes 3 \& 4 for } \hat{G}_\eta$$

$$= -\text{SIGN}(U_a) \text{ for nodes 1 \& 2 for } \hat{G}_\eta$$

Applying the above conventions for Γ_1 and Γ_2 to the equation for F_n and noting that each node on a face receives half of F_n yields:

For nodes 2 & 3 (for $\hat{F}_\xi$) or nodes 3 & 4 (for $\hat{G}_\eta$),

$$F^+ = 0.25[(1 + \Gamma_1)F + \Gamma_1(f_1 - f_2) + (f_4 - f_3)]$$

For the opposite nodes,

$$F^- = 0.25[(1 - \Gamma_1)F - \Gamma_1(f_1 - f_2) - (f_4 - f_3)]$$

or

$$F^\pm = 0.25[(1 \pm \Gamma_1)F \pm \Gamma_1(f_1 - f_2) \pm (f_4 - f_3)]$$

$$= 0.25F_n \pm 0.25(\Gamma_1 F_n + B]$$

where

$$B = \Gamma_1(f_1 - f_2) + (f_4 - f_3)$$

The flux equation consists of a center differenced term involving F_ξ or G_η only and a bias term B which is windward differenced but sums to zero over the element, thus ensuring the integral

144

conservation of the flow equations over the element.

The bias term B can be simplified using the following groupings of parameters:

$b_1 = \Gamma_1 C - U$

$b_2 = \Gamma_1 U - C$

$b_3 = [U\rho_n - (\rho U)_n]b_1/C - nP_n b_2/C^2$

$b_4 = [U\rho_n - (\rho U)_n]b_2 - nP_n b_1/C$

Then

$B = \quad b_3$

$\qquad b_3 u + b_4 \hat{n}_x$

$\qquad b_3 v + b_4 \hat{n}_y$

$\qquad b_3 H_T + b_4 U$

The above derivation results in a finite volume, totally conservative, windward algorithm consisting of center differenced fluxes with a windward bias involving no time-consuming matrix multiplies.

3.0 CHECK-OUT CASES RUN WITH GWIND

Several check out cases have been executed to verify the GWIND code. These cases include three source flow cases and a boundary layer case. The 2-D source flow case presented was also presented in the final report for the Phase I SBIR, however the results presented herein represent a significant improvement in accuracy over the earlier results. Also included are two axisymmetric source flow cases, one without a shock and one with a shock in the nozzle. The boundary layer case is a solution to the Blasius flat plate laminar flow problem.

3.1 Source Flow Cases

Source flow cases for 2-D and axisymmetric nozzles were run for a 15 degree half cone with a inlet Mach Number of 1.24. In each case the grid consisted of 57 nodes in the streamwise direction and 7 nodes in the normal direction. These cases were run on a microcomputer; they have not been run on the mainframe yet. The results of the calculations are presented in the table below. The parameter "Iterations" in the table indicated how many iterations it took to lower the sum of the squares of the errors by 5 orders of magnitude running at a CFL fraction of 0.9.

Although the solutions are not completely obtained at these
iteration numbers, the final answers have been obtained with only
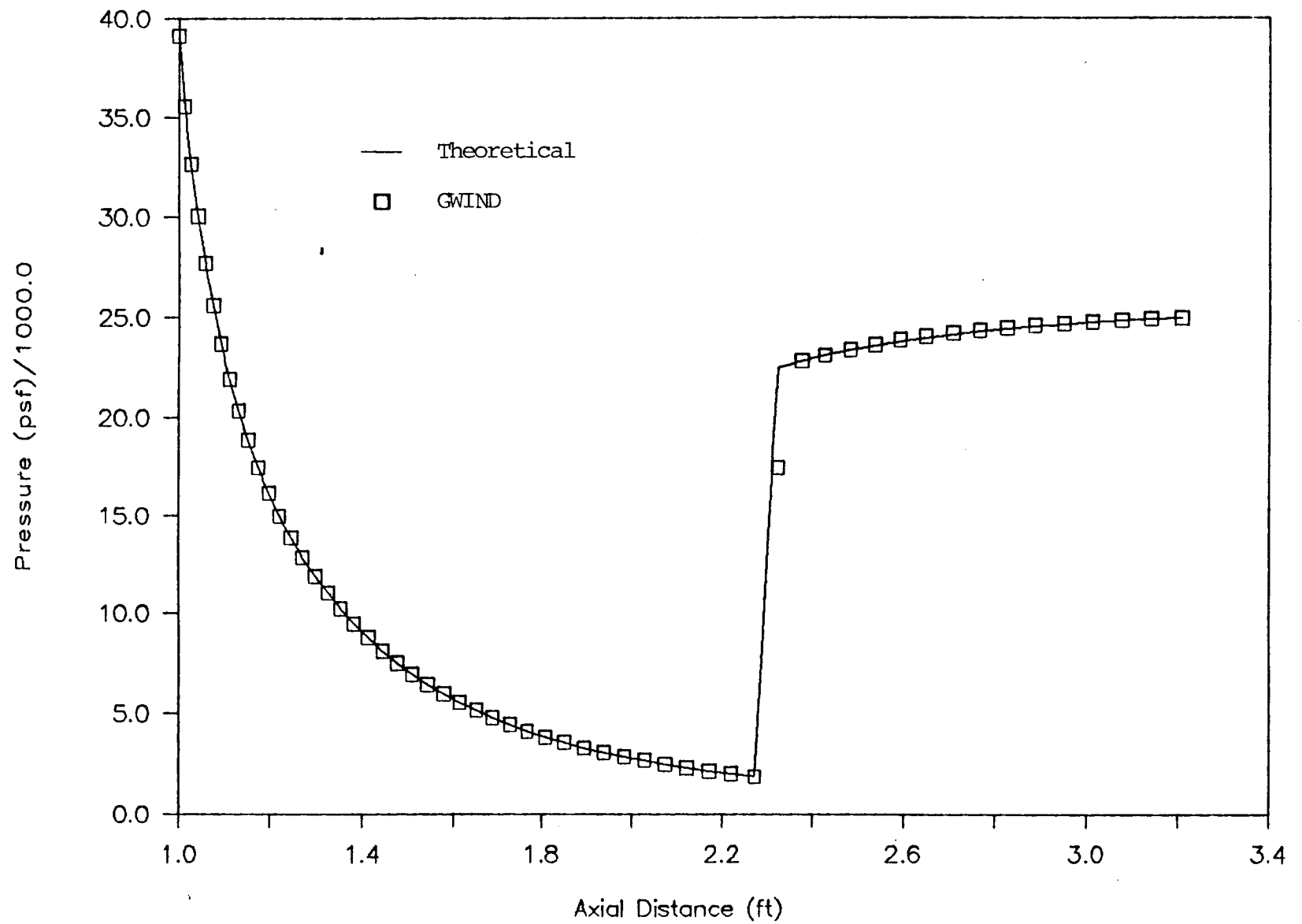a slight smoothing of the results remaining.

SOURCE FLOW RESULTS

| | | 2-D | | AXI | |
Parameter	Inlet	Correct Answer	Computed Answer	Correct Answer	Computed Answer
Pressure	39123	12780	12771	658.6	656.4
Density	.02981	.01341	.01340	.001612	.001609
Temperature	764.8	555.6	555.4	238.1	237.7
Velocity	1681	2311	2311	3025	3026
Mach No.	1.240	2.000	2.001	4.000	4.005
Total Temp.	1000	1000	1000	1000	1000
Total Pres.	100000	100000	100050	100000	100250
Iterations			350		500

The axisymmetric source flow case above was rerun specifying
an exit static pressure of 25000, causing a normal shock to stand
in the nozzle. Although a very crude grid (57 × 7) was used in
the analysis, excellent agreement with the correct shock location
and strength were obtained, as shown in the table below.
Excellent agreement was obtained for pressure, as shown in Figure
1, with no undershooting or overshooting near the shock. The
shock was smeared over 2 elements, resulting in some ambiguity in
the values chosen to represent the upstream pressure and the
downstream Mach Number.

SOURCE FLOW SHOCK PROBLEM

Parameter	Answer	Calculated
Upstream Mach No.	3.251	3.261
Upstream Press.	1877	1868
Downstream Mach no.	.4490	.4090
Downstream Press.	22482	22812
D'stream Total Pr.	25818	25602
Exit Mach No.	.215	.224
Exit Pressure	25000	25000

146

Figure 1.   Nozzle Shock

Plot of Pressure (psf)/1000.0 versus Axial Distance (ft), comparing Theoretical (line) and GWIND (squares).

3.2 LAMINAR BOUNDARY LAYER

A constant properties flat plate boundary layer was computed and compared with the Blasius solution to verify the laminar capabilities of GWIND. A rectangular 77 × 25 grid was used and a correct Blasius solution was imposed on the inlet. The results at the downstream boundary were compared to the Blasius solution to determine if the correct profile was maintained and if the boundary layer thickness grew at the proper rate. A plot of the downstream results compared to the Blasius solution are presented in Figure 2. The downstream profile agreed very well with Blasius except two small kinks near the wall. The cause of these kinks is still under investigation.

Figure 2. Laminar Boundary Layer
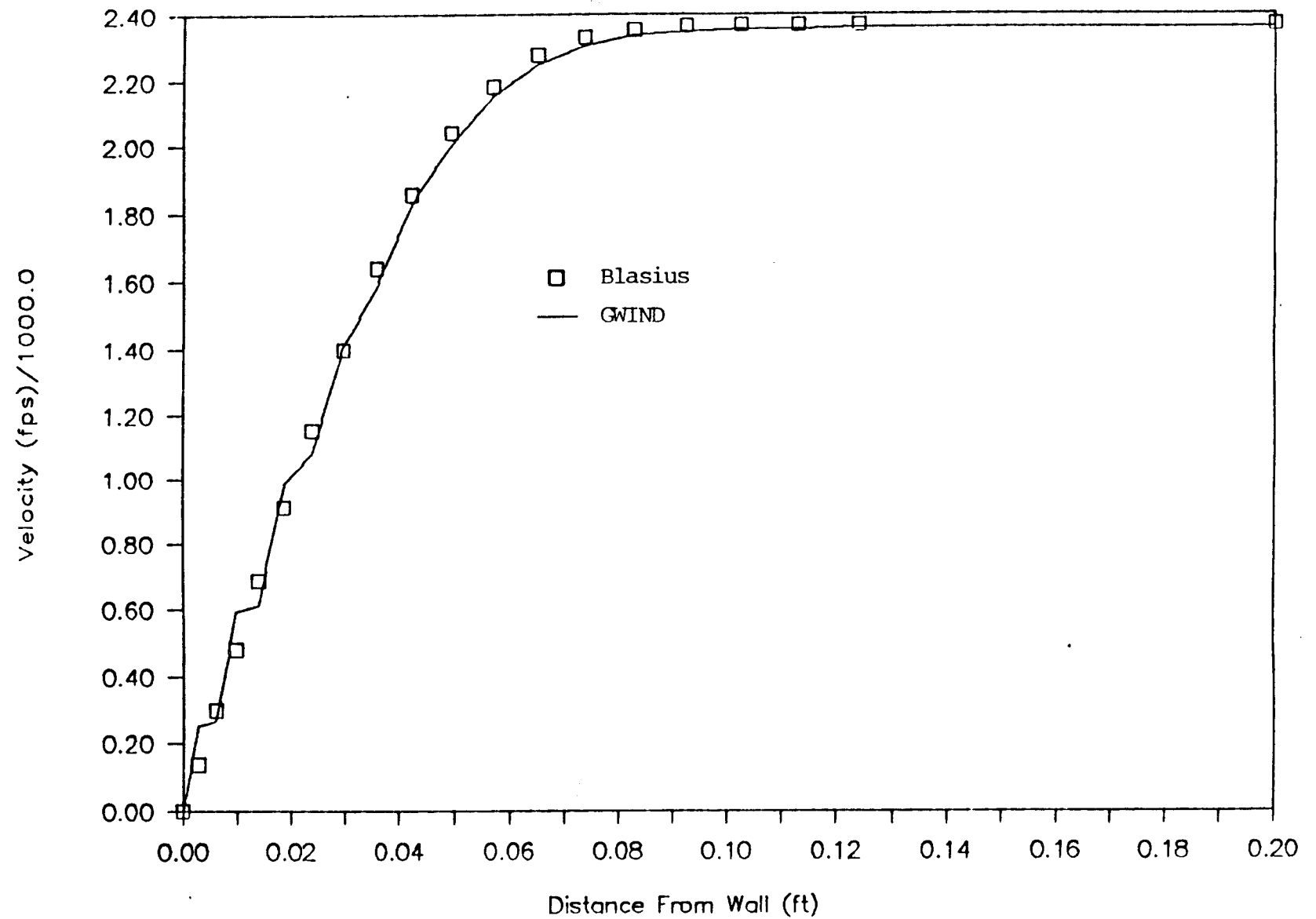
4.0 PRELIMINARY DESIGN FOR IMPLICIT INTEGRATOR FOR GWIND.

An implicit ADI integrator will be developed as a propulsion and plume analyzer which is optimized for describing steady-state, turbulent, combusting flow in moderately complex geometric regions. An upwind, finite volume method will be used to give good stability, accuracy and robustness characteristics. Many numerical methods have been developed for efficiently solving either the non-factored or factored Jacobian matrix using line-relaxation, LU decomposition or multi-grid techniques, etc., for the former case and ADI solvers for the latter case. Among these, the most well accepted approach is the ADI method due to its robustness and computational efficiency. The advantages of ADI are realized only when the mesh used is nearly orthogonal and smooth. As the grid skewness increases, the ADI convergence rate deteriorates due to increasing off-diagonal contributions. For such skewed, complex grids, LU decomposition or multi-zone with multi-grid approaches could be considered, although they are slower and require more storage. Since our major goal is to simulate combusting systems with sophisticated turbulence models, the ADI method is selected for this integrator development and the grid limitations will be accepted. For numerical accuracy, the well tested flux difference, second-order upwind scheme of Roe will be adopted. Roe's scheme with a TVD flux limiter has been reported to be fully conservative, accurate, and computationally efficient. Other flux splitting schemes such as Osher's and Beam-Warming's are more complex to implement. It is recognized that other codes contain many of the required features, are available, and could be considered for use, if modified. In general, these codes do not contain an adequate combustion chemistry capability. The PARC code uses central differencing and artificial damping for stability. Rai's code uses Osher's flux splitting scheme. CFL3D uses an LU solver. All of these codes suffer severe limitations for the intended applications; therefore, SECA will develop an implicit, upwind, ADI code with Roe's flux splitting scheme and with a multi-grid capability to address steady-state, turbulent combustion flows relative to propulsion devices and their associated plumes.

The equations previously developed serve as a staring point in designing an implicit code, except that the third dimension and the viscous terms must be added to the equations. This means that H will be defined differently. Only the equation for H will be shown to indicate how it differs and how the viscous terms appear.

$$
H = \begin{bmatrix} \rho\ w \\ \rho\ u\ w - \tau_{xz} \\ \rho\ v\ w - \tau_{yz} \\ \rho\ w\ w + P - \tau_{zz} \\ \rho\ w\ E_T + w\ P - u\ \tau_{xz} - v\ \tau_{yz} - w\ \tau_{zz} + q_z \end{bmatrix}
$$

A transformation to computational coordinates will be used, such that (x, y, z) become (ξ, η, ζ) and H becomes $\hat{H}$, etc.

Roe's flux difference method will be used.

$$\hat{H}_{k+.5} = 0.5[\hat{H}\{Q^L\} + \hat{H}\{Q^R\}]_{k+0.5} - 0.5\ |\hat{C}\{Q^L,Q^R\}|\ (Q^L - Q^R)_{j+0.5}$$

where $Q^L_{i+0.5} = Q_{\lambda,j} + 0.25\phi[(1-\kappa)\nabla_i + (1+\kappa)\Delta_i]Q_{i,j}$

$\qquad Q^R_{i+0.5} = Q_{\lambda+1,j} - 0.25\phi[(1+\kappa)\nabla_i + (1-\kappa)\Delta_i]Q_{i+1,j}$

$\quad \kappa = -1$ full second-order upwind

$\qquad = +1$ second-order central

$\qquad = 1/3$ 3rd-order upwind

$\quad \phi =$ 1st-order/2nd-order switching parameter

The vector D now has inviscid and viscous parts, such that:

$A = \hat{A} + A_V, \quad B = \hat{B} + B_V, \quad C = \hat{C} + C_V$

The discretized equations become:

$$[I + \theta\ \Delta t(\dot{\hat{A}}_\xi + \dot{\hat{B}}_\eta + \dot{\hat{C}}_\zeta)]\ \Delta Q = -\ \Delta t[(F-F_V)_\xi + (G-G_V)_\eta + (H-H_V)_\zeta]$$

$$= -\ \Delta t\ R$$

Approximate factorization and sweeps are accomplished as follows. The dots denote time derivatives.

$$(I + \theta \, \Delta t \, \overset{\bullet}{A}_\xi)(I + \theta \, \Delta t \, \overset{\bullet}{B}_\eta)(I + \theta \, \Delta t \, \overset{\bullet}{C}_\zeta) \, \Delta Q = - \, \Delta t \, R$$

I sweep:

$$(I + \theta \, \Delta t \, \overset{\bullet}{A}_\xi) \, \Delta Q^i = - \, \Delta t \, R$$

J sweep:

$$(I + \theta \, \Delta t \, \overset{\bullet}{B}_\eta) \, \Delta Q^j = \Delta Q^i$$

K sweep:

$$(I + \theta \, \Delta t \, \overset{\bullet}{C}_\zeta) \, \Delta Q = \Delta Q^j$$
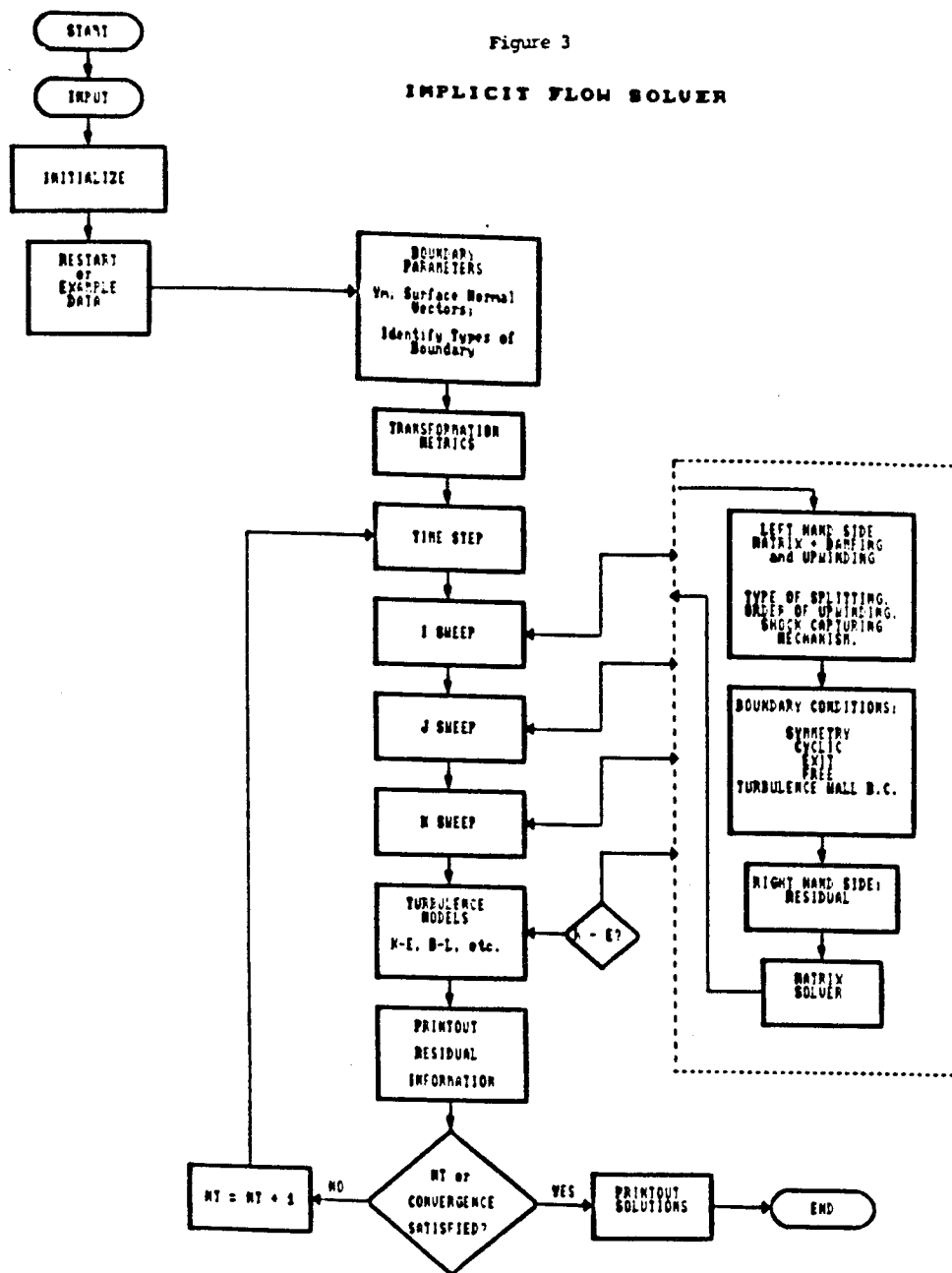
$$Q^{n+1} = Q^n + \Delta Q$$

A preliminary flow chart for the implicit version of GWIND is given in Figure 3.

5.0 CLOSURE

The development of a general computational tool to describe advanced rocket motors and their associated plumes has been initiated. An accurate and efficient explicit algorithm has been developed as the code GWIND; an implicit counterpart of this code is being prepared. Additional computations employing variational constraints to accelerate convergence are, apparently, not required. Turbulence models are already in the code, but have not yet been checked out. Chemistry models will be added to the code. A schedule of test cases to evaluate the codes has been established. Considering that this is a two year study, the progress reported in this first quarter constitutes an encouraging first step in providing a useful new generation of plume codes.

Figure 3

IMPLICIT FLOW SOLVER

153

NASA
Report Documentation Page

1. Report No.	2. Government Accession No.	3. Recipient's Catalog No.

4. Title and Subtitle	5. Report Date
THE USE OF VARIATIONAL PRINCIPLES IN IMPROVING COMPUTATIONAL FLUID DYNAMICS METHODOLOGY	MAY, 1990
	6. Performing Organization Code

7. Author(s)	8. Performing Organization Report No.
Yen-Sen Chen, Richard C. Farmer, and Jon A. Freeman	SECA-TR-90-05
	10. Work Unit No.

9. Performing Organization Name and Address	11. Contract or Grant No.
SECA, Inc. 3311 Bob Wallace Avenue, Suite 203 Huntsville, AL 35805	NAS8-37408
	13. Type of Report and Period Covered

12. Sponsoring Agency Name and Address	Contractor - FINAL
George C. Marshall Space Flight Center Marshall Space Flight Center, AL 35812	14. Sponsoring Agency Code

15. Supplementary Notes

Mark Seaford/Technical Monitor

16. Abstract

  The concept of this study is to develop accurate and efficient computational fluid dynamics (CFD) algorithms for production type analyses of viscous/turbulent, multicomponent, combusting flows.

17. Key Words (Suggested by Author(s))	18. Distribution Statement
CFD, Rocket Propulsion, Rocket Plumes	unclassified - unlimited

19. Security Classif. (of this report)	20. Security Classif. (of this page)	21. No. of pages	22. Price
unclassified	unclassified	154	